Moving liquid droplets with inertia: Experiment, simulation, and theory

Moving liquid droplets with inertia: Experiment, simulation, and theory

Proefschrift

ter verkrijging van de graad van doctor
aan de Technische Universtiteit Delft,
op gezag van de Rector Magnificus Prof. ir. K.C.A.M. Luyben,
voorzitter van het College voor Promoties,
in het openbaar te verdedigen
op dinsdag 5 februari 2013 om 15:00 uur
door

Hyoungsoo KIM

Master of Science in Mechanical Engineering, Korea Advanced Institute of Science and Technology (KAIST)

geboren te Busan, Republic of Korea

Dit proefschrift is goedgekeurd door de promotor:
Prof. dr. ir. J. Westerweel

Samenstelling promotiecommissie:

Rector Magnificus,	voorzitter
Prof. dr. ir. J. Westerweel,	Technische Universiteit Delft, promotor
Prof. dr. F. G. Mugele,	Technische Universiteit Twente
Prof. dr. A. A. Darhuber,	Technische Universiteit Eindhoven
Prof. dr. D. Bonn,	Universiteit van Amsterdam
Prof. dr. U. Staufer,	Technische Universiteit Delft
Dr. ir. C. Poelma,	Technische Universiteit Delft
Dr. ir. R. Badie,	ASML Holding NV

Keywords: Moving contact line, Immersion droplet, Tomographic particle image velocimetry, 3D particle tracking velocimetry, Modified lubrication theory, Dewetting, zero-flux boundary condition model

The research described in this thesis was performed in the Lab. for Aero- and Hydrodynamincs, of the department Process and Energy, of the Delft University of Technology, Delft, The Netherlands.

ISBN : 978-94-6186-115-3

Cover design: Kyungeun Lee

Copyright © 2013 by Hyoungsoo KIM

All rights reserved. No part of this book may be reproduced, stored in a retrieval system, or transmitted, in any form or by any means, without prior permission from the copyright owner.

PRINTED IN THE NETHERLANDS

To my family

Financial support
This work is part of the Industrial Partnership Programme (IPP) ‘Contact line control during wetting and dewetting’ (CLC) of the Foundation for Fundamental Research on Matter (FOM), which is supported financially by the Netherlands Foundation for Scientific Research (NWO). The IPP CLC is co-financed by ASML and Océ.

Contents

Preface **xi**

Summary **xiii**

Samenvatting **xvii**

1 Introduction **1**
- 1.1 Background 1
  - 1.1.1 Basic 1
  - 1.1.2 Dimensionless parameters 4
  - 1.1.3 Wetting and dewetting examples 5
  - 1.1.4 Hydrodynamics issue: singularity 5
- 1.2 Motivation 6
- 1.3 Particle Image Velocimetry towards free-surface 10
- 1.4 Objectives and scope of this thesis 11
- 1.5 Outline of the thesis 13
- 1.6 Bibliography 14

2 Experiment I: Full 3D-3C velocity measurement inside a liquid immersion droplet **19**
- 2.1 Introduction 19
- 2.2 Experimental setup 21
- 2.3 Pre- and post-processing for 3D-3C data 26
  - 2.3.1 Image processing 26
  - 2.3.2 3D calibration and correction 28
  - 2.3.3 Tomographic reconstruction 30
- 2.4 Results and discussion 31
  - 2.4.1 Error estimation 31
  - 2.4.2 3D Flow field 32
- 2.5 Conclusion 37
- 2.6 Acknowledgemet 37
- 2.7 Bibliography 38

3 Experiment II: Comparison of Tomo-PIV and 3D-PTV for microfluidic flows 41
3.1 Introduction . . . 42
3.2 Experimental set-up . . . 43
3.3 Methods . . . 45
3.3.1 3D Particle Tracking Velocimetry . . . 47
3.3.2 Tomographic Particle Image Velocimetry . . . 48
3.4 Results and discussion . . . 50
3.4.1 Result comparison of 3D-PTV and Tomo-PIV . . . 50
3.4.2 Comparison of particle reconstructions . . . 52
3.4.3 Assessment of velocity accuracy and divergence . . . 57
3.4.4 Quantitative comparison of velocity profiles . . . 58
3.5 Discussion and conclusion . . . 60
3.6 Acknowledgments . . . 61
3.7 Bibliography . . . 61

4 Experimental and theoretical investigation of dewetting corner 65
4.1 Introduction . . . 66
4.2 Experiments . . . 68
4.2.1 High-speed shadowgraphy recording . . . 68
4.2.2 Tomographic particle image velocimetry . . . 69
4.3 Experimental results and discussion . . . 71
4.3.1 Scaling analysis . . . 71
4.3.2 Internal flow pattern . . . 76
4.4 Model problem . . . 78
4.4.1 Modified three-dimensional lubrication model for the dewetting corner . . . 78
4.4.2 Modified interface equation $H(\zeta)$ for dewetting corner . . . 81
4.4.3 Self-similar flow pattern at $Re \sim O(100)$ . . . 85
4.5 Discussion and conclusion . . . 89
4.6 Acknowledgments . . . 90
4.7 Bibliography . . . 91

5 Numerics: Simplified droplet models 93
5.1 Introduction . . . 93
5.2 Model problem . . . 95
5.3 Results and discussion . . . 98
5.4 Conclusion . . . 102
5.5 Acknowledgement . . . 103
5.6 Bibliography . . . 103

6 Discussion and conclusion 105

A Supplement: experimental setup 109

A.1 Recirculation unit 109
A.2 Glass wafer 109

B Particle deposition **113**

C Validation for shooting method **115**
C.1 Bibliography 116

Acknowledgements **117**

List of Publications **119**

Curriculum Vitae **121**

Preface

"None of us can know what the world is in the way that we used to know it. Einstein says that time is not the same for all of us but different for each one of us. It is very hard to conceive of such separate views, of such relative way of seeing. Today is the first day of a new world that is much harder to live in: less certain, more lonely."

from the movie, Einstein and Eddington (2008).

In the 17th century, Isaac Newton described how gravity acts and explained why. Since his theory, during about a 200 years, everybody had believed Newton's theory for gravity. The planets make their orbits around the sun. By Newton's theory of gravity, we can estimate their orbits. Where will they be? When do they pass closest to the sun? However, the theory was not perfect. ***Mercury!*** The predicted orbit of Mercury based on Newton's theory was different from the true orbit that we observed. In the 19th century, Albert Einstein introduced a new theory that all things with mass deform spacetime and this deformed curvature is an alteration of the geometry of spacetime. By considering this curved spacetime, we can correctly calculate the orbit of Mercury. Furthermore, Einstein produced $E = mc^2$ (E, energy; m, mass; and c, speed of light) from his special relativity theory, based upon the theorem that nothing can travel faster than light. For a long time, nobody could not claim this.

However, in 2011, the OPERA research group in Italy first claimed that there is a particle that can be faster than light. It is a neutrino. Eventually, the measured time difference was explained as a measurement error. However, this is a still controversial issue and nobody knows whether Einstein is perfectly right or not. I believe that it is not important who is right and who is wrong. The most important thing is an attitude on a research.

Every day and every time, we experience science and nature. In order to explain the phenomena, we learn and use physics. However, I believe that there is no absolute answer to explain nature. Always, keep asking, keep thinking, and keep answering.

Delft, the Nethlerands
Hyoungsoo Kim

Summary

Moving liquid droplets with inertia: Experiment, simulation, and theory – H. Kim

Recently, water-based immersion lithography has been introduced for producing 50-nm and sub 40-nm devices in the semiconductor industry. The main advantage of using immersion fluids is that it yields enhanced spatial resolution due to a higher refractive index ($n_{water} \approx 1.44$) for 193nm light compared to air ($n_{air} \approx 1.0$). One of the primary challenges remaining in immersion lithography is to maintain the liquid stably between the freely moving optical scanner and the silicon wafer. The confined liquid layer is partially wetting and dewetting where there is a contact line of solid, gas, and liquid phases. During scanner operation, the relative contact line velocity of the liquid layer increases up to $O(1\text{ m/s})$ and contact line instability occurs at critical conditions.

Interestingly, we can notice a similar phenomenon in nature, i.e. droplet breakup. After rain, a raindrop on a window is sliding down, sometimes leaving behind tiny droplets. In this case, the internal flow velocity is of the order of a few mm/s or cm/s, which is very slow compared to a liquid droplet of the immersion lithography.

Currently, there are many efforts to understand the droplet breakup mechanisms for creeping flow conditions. In contrast, investigation of droplet breakup in a higher velocity flow regime, $V \approx O(1\text{ m/s})$, is at an early stage. To achieve a better understanding of the latter instability mechanism, we perform an experimental, theoretical, and numerical analysis of a partial wetting and dewetting flow over a moving substrate with a velocity $U \approx O(1\text{ m/s})$.

The first part of the thesis describes the experimental setup and the measurement techniques used: shadowgraphy and particle image velocimetry. The liquid immersed droplet is generated by a simplified immersion device that has the same basic functioning of a real immersion device (supplying water at the inlet and extracting water and air at the outlet). The droplet thickness is of the order of a hundred micron.

To investigate the flow field inside the moving droplet, we perform tomographic particle image velocimetry and 3D particle tracking velocimetry, which enable us to measure three-dimensional three-component velocities in a volume. Even though the two techniques were expected to give the same result, we have observed differences. To investigate this issue, we have quantitatively compared and evaluated both results, considering (1) the mass conservation in the droplet, (2) the reconstructed 3D particle distributions, (3) the divergence of the flow, and (4) velocity profiles.

Based on these assessments, we conclude that tomographic particle image velocimetry is an applicable method for measuring the complex micro-scale flow patterns robustly and accurately. In the following parts, velocity flow fields are presented, which were obtained by tomographic particle image velocimetry. We first obtain an internal flow pattern of the immersion droplet and show a recirculation region close to the rear part of the droplet. Furthermore, a self-similar flow pattern is observed near the corner region of the dewetting contact lines.

Surprisingly enough there are some similarities between a gravity-driven liquid droplet on an inclined surface at $Re \ll 1$ and an immersion droplet at $Re \sim O(100)$: (1) a relation between the dynamic receding contact angle θ and the velocity U of the contact line, i.e., $\theta^3 = f(Ca)$ where Ca is the capillary number, (2) a self-similar flow pattern near the corner (dewetting), and (3) a relation between the dynamic receding contact angle and the corner opening angle.

For the gravity-driven droplet, the analytical results were obtained by using creeping flow ($Re \ll 1$) and classical lubrication approximations ($\epsilon \cdot Re \ll 1$), where Re is the Reynolds number and ϵ is an aspect ratio of the flow structure. Voinov (1976) and Cox (1986) first described the relation between the dynamic receding contact angle and the velocity U of the contact line, the so-called Cox-Voinov law. Stone et al. (2002) and Limat and Stone (2004) first obtained the three-dimensional lubrication model. Based on this model, Snoeijer et al. (2005) found out a self-similar flow pattern near the corner structure. However, these analytical solutions can not fully explain similarities in the liquid immersion droplet at $Re \sim O(100)$ and $\epsilon \cdot Re > 1$.

In the second part of this thesis, we perform a theoretical study of the dewetting flow in the immersion droplet. To further investigate the liquid immersion droplet, we observe the shape of the droplet by means of high-speed shadowgraphy. Based on this, we perform a scaling analysis. First, we present that the dynamic receding contact angle and the corner opening angle are correlated with each other, which is described by an empirical model. Second, we show that $\epsilon \cdot Re$ is larger than unity and hence the existing analytical solutions are not applicable to the present problem. Thus the classical lubrication theory has to be modified. In the theoretical approach of this thesis, we introduce such a modified model based on a scaling analysis and flow pattern analysis.

Based on measurement results by shadowgraphy and tomographic particle image velocimetry, we derive a modified lubrication theory for $\epsilon \cdot Re > 1$. By scaling arguments, we assume that the normal velocity and the normal vorticity components are negligible

in comparison with other components. The streamlines are nearly parallel and straight between boundaries, which is validated by tomographic particle image velocimetry. Based on these assumptions, we obtain a modified pressure that consists of a capillary pressure and a dynamic pressure. The nonlinear acceleration terms (inertial effects) are expressed in terms of the dynamic pressure.

Based on the modified lubrication model, we first provide an approximate analytical solution to describe a three-dimensional corner structure, i.e. the relation between the dynamic receding contact angle and the half corner opening angle. From this analytical solution, we postulate that there are two regions, which are dominated by either the capillary pressure and the dynamic pressure. In fact, when the half corner opening angle becomes smaller (fast substrate speed), the dynamic pressure effect becomes dominant. Subsequently, we obtain an analytical velocity profile that shows a self-similar flow pattern near the corner-shaped contact lines at $\epsilon \cdot Re > 1$. In this part, we compare two different cases, the gravity-driven droplet and the immersion droplet, to explain the observed similarity. Incidentally, both analytical results are analogous. However, when the corner opening angle is small, the two solutions are slightly different. These theoretical results are validated by the experimental results.

The third part provides a simplified numerical model to investigate the internal flow pattern of the immersion droplet. In this approach, the immersion droplet is simplified as a flat cylinder. The liquid-gas interface is fixed and is assumed as a zero flux boundary. For the inlet and outlet boundary conditions, we apply a similar basic functioning of the current simplified immersion needle device as used in the experiments. The simplified numerical model is qualitatively in a good agreement with the experimental result. In this thesis, we propose the idea of simplifying the computational model anticipating it can assist in improving the immersion hood design.

Samenvatting

Bewegende druppels met traagheid: Experimenten, simulaties en theorie − H. Kim

In recente jaren is immersie-lithografie geïntroduceerd in de halfgeleiderindustrie om 50-nm en sub 40-nm structuren te maken. Het grootste voordeel van het gebruik van immersievloeistoffen is de toename in de ruimtelijke resolutie door de hogere brekingsindex ($n_{water} \approx 1.44$) voor 193 nm licht, vergeleken met lucht ($n_{lucht} \approx 1.0$). Een van de belangrijkste uitdagingen in immersie-lithografie is het stabiel houden van de vloeistof tussen de vrijelijk bewegende optische scanner en de silicium wafer. De vloeistoflaag zal het substraat gedeeltelijk bevochtigen op de contactlijn tussen vaste, gasvormige en vloeibare fasen. Tijdens de werking van de scanner zal de contactlijn van de vloeistof bewegen met een relatieve snelheid tot $O(1\ \mathrm{m/s})$ en zal de contactlijn instabiel worden bij kritische condities.

Opmerkelijk genoeg treedt een vergelijkbaar fenomeen, het opbreken van druppels, ook op in de natuur. Na een regenbui glijdt een droppel omlaag over een raam, soms kleine druppels achterlatend. In dit geval zijn de interne stroomsnelheden in de orde van enkele mm/s of cm/s, wat erg traag is vergeleken met de druppel in immersie-lithografie.

Er wordt momenteel veel aandacht besteed aan het begrijpen van het mechanisme dat druppels doet opbreken in kruipstromingen. Daarentegen is het onderzoek naar het opbreken van druppels bij hogere snelheden, $V \approx O(1\ \mathrm{m/s})$, nog relatief onontgonnen. Om een beter begrip te krijgen van dit instabiliteitsmechanisme, analyseren we de gedeeltelijk bevochtigende stroming over een bewegend substraat met een snelheid van $U \approx O(1\ \mathrm{m/s})$, met behulp van experimenten, theoretische modellering en numerieke simulaties.

In het eerste gedeelte van dit proefschrift worden de experimentele opstelling en de meettechniek beschreven: *shadowgraphy* en *particle image velocimetry*. De immersie-druppel wordt gegenereerd met behulp van een versimpeld immersie apparaat dat dezelfde basisfunctionaliteit heeft als een echt immersie apparaat (toevoer van water bij de instroom en extractie van water en lucht bij de uitstroom). De druppel heeft een dikte in de ordegrootte van honderd micrometer.

We onderzoeken de stroming in de bewegende druppel met behulp van *tomographic*

particle image velocimetry en *3D particle tracking velocimetry*, technieken die het mogelijk maken om de drie snelheidscomponenten in drie dimensies te meten. Hoewel verwacht werd dat de twee technieken dezelfde resultaten zouden geven, zagen we verschillen. Om deze te onderzoeken hebben we de resultaten kwantitatief onderzocht en vergeleken, met name (1) massabehoud in de druppel, (2) de reconstructie van de 3D verdeling van deeltjes, (3) de divergentie van het snelheidsveld en (4) snelheidsprofielen.

Op basis van deze analyse concluderen we dat *tomographic particle image velocimetry* een geschikte methode is voor het meten van complexe stromingen op microschaal op een robuuste en nauwkeurige manier. In de volgende secties worden de snelheidsvelden getoond die met *tomographic particle image velocimetry* verkregen werden. Allereerst verkrijgen we een inwendig stromingspatroon van de immersie-druppel en laten we zien dat er een gelijkvormig patroon is aan de achterzijde van de druppel. Hiernaast is een gelijkvormig stromingspatroon te onderscheiden in de hoek gevormd door de contactlijnen aan de achterzijde van de druppel.

Het is interessant dat een door zwaartekracht gedreven druppel op een hellende plaat bij $Re \ll 1$ overeenkomsten vertoont met een immersie-druppel bij $Re \sim O(100)$: (1) een correlatie tussen de dynamische terugwijkende contacthoek θ en de snelheid U van de contactlijn, ofwel $\theta^3 = f(Ca)$, waarbij Ca het capillair getal is, (2) een gelijkvormig snelheidsveld nabij de hoek aan de achterzijde van de druppel, en (3) een correlatie tussen de dynamische terugwijkende contacthoek en de openingshoek van de achterzijde van de druppel.

Voor de door zwaartekracht gedreven druppel werden de analytische resultaten bepaald met behulp van kruipstroming ($Re \ll 1$) en klassieke smeringstheorie ($\epsilon \cdot Re \ll 1$), waarbij Re het Reynolds getal is en ϵ de aspect ratio van de druppel. Voinov (1976) en Cox (1986) waren de eerste die de relatie beschreven tussen de dynamische terugwijkende contacthoek en de snelheid U van de contactlijn, de zogenaamde wet van Cox-Voinov. Stone et al. (2002) en Limat en Stone (2004) verkregen als eerste het drie-dimensionale smeringsmodel. Op basis van dit model vonden Snoeijer et al. (2005) het gelijkvormige stromingsveld nabij de hoek. Deze analytische oplossingen kunnen echter niet de gelijkenissen verklaren die te zien zijn in de immersie druppel bij $Re \sim O(100)$ en $\epsilon \cdot Re > 1$.

In het tweede gedeelte van dit proefschrift voeren we een theoretische studie uit van de *dewetting* stroming van een immersie-druppel. Om de immersie-druppel verder te onderzoeken, bepalen we de vorm van de druppel met behulp van hogesnelheids *shadowgraphy*. Op basis hiervan voeren we een schaalanalyse uit. Allereerst laten we zien dat de dynamische terugwijkende contacthoek en de openingshoek gecorreleerd zijn, wat beschreven kan worden met een empirisch model. Vervolgens laten we zien dat $\epsilon \cdot Re$ groter dan 1 is en de bestaande analytische oplossingen dus niet toepasbaar zijn op het huidige probleem. De klassieke smeringstheorie dient dus aangepast te worden. In de theoretische benadering van dit proefschrift introduceren we een gemodificeerd model op basis van een schalingsanalyse en een analyse van het stromingspatroon.

Op basis van de meetresultaten verkregen met behulp van *shadowgraphy* en *tomographic velocimetry* leiden we een gemodificeerd smeringsmodel af voor $\epsilon{\cdot}Re > 1$. Met behulp van schalingsargumenten nemen we aan dat de snelheids- en vorticiteitscomponenten loodrecht op het substraat verwaarloosbaar klein zijn ten opzichte van de overige componenten. De stroomlijnen zijn nagenoeg evenwijdig en recht, wat bevestigd werd door *tomographic particle image velocimetry*. Op basis van deze aannames verkrijgen we een gemodificeerde druk die bestaat uit de capillaire druk en de dynamische druk. De niet-lineaire acceleratie termen (traagheidseffecten) komen tot uiting in de dynamische druk.

Op basis van het gemodificeerde smeringsmodel kunnen we allereerst een analytische benadering vinden voor de drie-dimensionale vorm van de hoek, ofwel de verhouding tussen de dynamische terugwijkende contacthoek en de openingshoek. Op basis van dit analytische resultaat kunnen we postuleren dat er twee gebieden zijn, die gedomineerd worden door de capillaire druk danwel de dynamische druk. In feite worden de dynamische druk dominant als de halve openingshoek kleiner wordt (bij hogere substraat snelheden). Ten tweede verkrijgen we een analytisch snelheidsprofiel dat gelijkvormig is nabij de hoek van de contactlijnen bij $\epsilon{\cdot}Re > 1$. In dit gedeelte vergelijken we de twee verschillende gevallen (de door zwaartekracht gedreven druppel en de immersie-druppel) om de gelijkenissen te verklaren. Overigens zijn de analytische resultaten vergelijkbaar. Wanneer de openingshoek klein is, zijn de oplossing echter ietwat verschillend. De theoretische resultaten worden gevalideerd door experimentele resultaten.

In het derde deel wordt een versimpeld numeriek model beschreven om de inwendige stroming in een immersie-druppel te bestuderen. In deze benadering wordt de immersie-druppel versimpeld tot een platte cilinder. Het vlak tussen vloeistof- en gasfase ligt vast en wordt beschouwd als een niet-doorlatende randvoorwaarde. Voor de in- en uitstroom randvoorwaarden passen we een vergelijkbare versimpeling van het immersie apparaat toe zoals werd gebruik in de experimenten. Het versimpelde numerieke model is kwalitatief in goede overeenstemming met de experimentele resultaten. In dit proefschrift stellen we dat het versimpelde numerieke model een manier is om de immersie apparatuur te ontwerpen.

CHAPTER 1

INTRODUCTION

1.1 Background

1.1.1 Basic

On a rainy day, we can observe that small drops stick to a window. Occasionally, raindrops roll or slide down and other larger drops leave a trail of water. The liquid droplet is dragged over the surface of the window by gravity. In a similar case, the droplets are moving on a window of a car or train. In this case, the droplet is driven by a surrounding fluid motion. The contact line, the region where gas, liquid, and solid phase meet, is moving with respect to the substrate, so-called wetting and dewetting phenomena.

First, let us consider the wetting condition. If a liquid droplet is placed on a very clean solid substrate, we observe a spreading of the liquid. This is due to interactions at the molecular scale between different phases. The gas-liquid interface is mainly governed by the affinity (i.e. the intermolecular force) between the molecules in the solid, the liquid, and the gas. The substrate can be either totally or partially wetted by the liquid. A spreading parameter S describes the difference in overall surface energies (De Gennes et al., 2004). The parameters can be defined by considering the surface energy of the substrate:

$$S = [E_s]_{dry} - [E_s]_{wet} = \gamma_{sg} - (\gamma_{sl} + \gamma_{gl}), \tag{1.1}$$

where E_s is the substrate surface energy per unit area and γ is surface tension between different phases. The subscripts, i.e. sg, sl, and gl, indicate solid-gas, solid-liquid, and gas-liquid, respectively. If $S \geq 0$, the liquid phase is totally wetting along the solid substrate. If $S < 0$, the liquid does not fully spread, but the liquid drop forms at equilibrium as shown

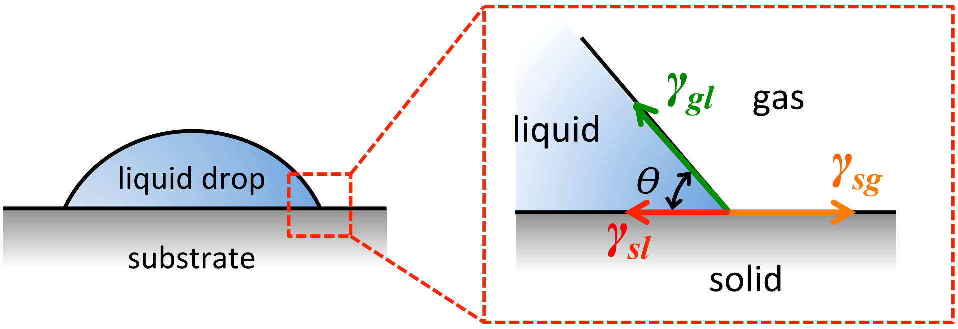

Figure 1.1: A sketch of an equilibrium contact angle

on the left in figure 1.1.

Figure 1.1 shows an equilibrium state of a droplet on a substrate. At the contact line of solid, liquid, and gas phases, the force balance is expressed as follows:

$$\gamma_{gl}\cos\theta = \gamma_{sg} - \gamma_{sl}, \tag{1.2}$$

which is Young's relation where the equilibrium contact angle is θ, γ_{gl} the surface tension force, γ_{sg} the force between solid and gas, and γ_{sl} the force between solid and liquid (Young, 1805). By substituting equation 1.1 into 1.2, we obtain the spreading parameter such as:

$$S = \gamma_{gl}(\cos\theta - 1). \tag{1.3}$$

The spreading parameter is determined by the equilibrium contact angle θ and the surface tension γ_{gl}. When there is a partial wetting, the parameter is negative. As θ is increased, the liquid becomes non-wetting.

A surface tension represents attractive forces between liquid molecules, and it is a physical property of the liquid. The equilibrium contact angle depends on the surface energy of the substrate. For instance, the angle is changed with different substrate conditions, i.e. hydrophilic and hydrophobic surfaces. When a contact angle is smaller than 90°, the surface is hydrophilic. On the other case, when $\theta > 90°$, it is hydrophobic. For a different substrate condition, the ratio between dry and wet areas is different as shown in figure 1.2. In the case of hydrophobic surfaces, the solid surface is less wettable than hydrophilic ones. Even larger θ, in nature, you could notice a nearly perfect non-wetting liquid drop on a leaf as shown in figure 1.3, which is a superhydrophobic surface. With $\theta \sim 180°$, figure 1.3 shows an example that the surface tension along a gas-liquid interface is dominant.

The surface tension γ is a force per unit length [N/m], or energy per unit area [J/m^2]. It is inversely proportional to the length of contact lines. Due to the strong surface tension along

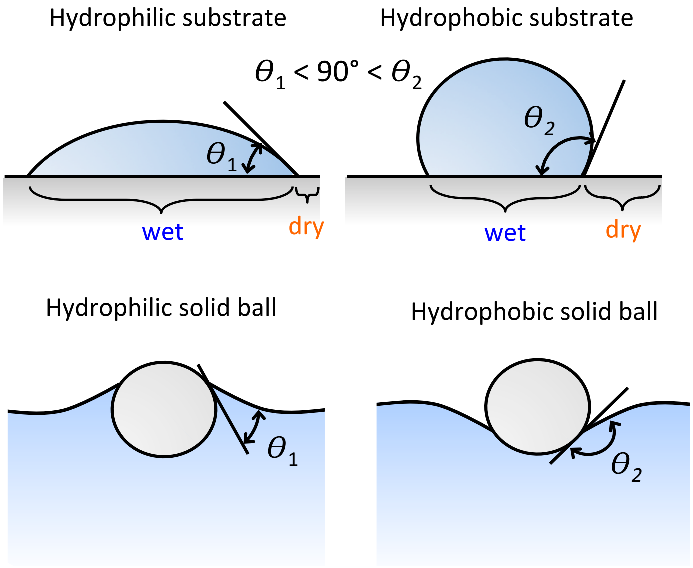
Hydrophilic substrate
Hydrophobic substrate
$\theta_1 < 90° < \theta_2$
θ_1
θ_2
wet
dry
wet
dry
Hydrophilic solid ball
Hydrophobic solid ball
θ_1
θ_2

Figure 1.2: Comparison of contact angles by hydrophilic and hydrophobic surfaces.

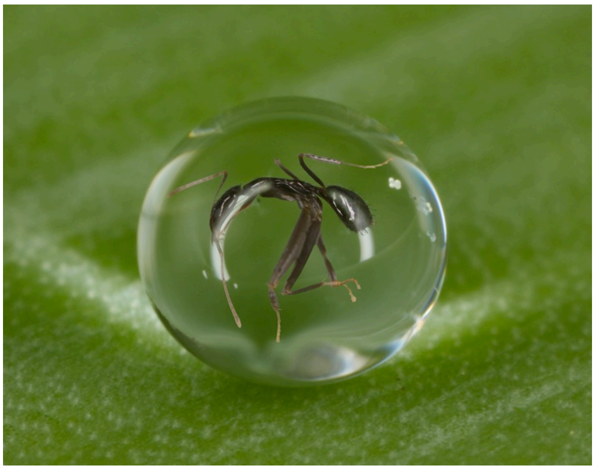

Figure 1.3: Non-wetting liquid drop on a superhydrophobic surface. An ant is entrapped a droplet by surface tension. Photo by: Adam Gormley.

the drop surface, once an ant has been entrapped, it can not escape by itself. The pressure difference across the gas-liquid interface is estimated by the Young-Laplace equation,

$$\Delta p = \gamma \left(\frac{1}{R_1} + \frac{1}{R_2} \right), \tag{1.4}$$

where Δp is the pressure difference across the gas-liquid interface, γ the surface tension, and R_1 and R_2 the principal radii of curvature. For pure water, γ is 72 mN/m. In the case of figure 1.3, $\Delta p \approx 96$ [Pa], provided that $R_1 = R_2 = 1.5$ mm. Evidently, the ant does not have the force to break the equilibrium state.

Surface tension becomes important when the characteristic length scale is small. When does the surface tension become important? How small is small? Commonly, the capillary length is used to determine whether the surface tension is important or not. The capillary length κ^{-1} can be estimated by comparing the Laplace pressure to the hydrostatic pressure, i.e. $\gamma/\kappa^{-1} = \rho g \kappa^{-1}$. Then, for water (density $\rho = 10^3$ kg/m^3) and normal gravitational acceleration ($g = 9.8$ m/s^2), a typical length scale is of the order of a few mm. If $\kappa^{-1} < O(1$ mm) for water, the surface tension dominates the behavior of the gas-liquid interface.

1.1.2 Dimensionless parameters

A hydrodynamics problem is governed by the Navier-Stokes equations that include all the physical parameters and variables. The full equations are extremely difficult to analyze in general. However, frequently, not all of these variables are encountered in a given problem. By using a dimensional analysis, the governing equations become dimensionless with non-dimensional groups expressing the relative importance of the forces. In wetting and dewetting problems, typical dimensionless numbers are introduced as below:

$$\text{Reynolds number} \qquad Re = \frac{\rho U \ell}{\mu} \qquad \frac{\text{inertia forces}}{\text{viscous forces}}, \tag{1.5a}$$

$$\text{Capillary number} \qquad Ca = \frac{\mu U}{\gamma} \qquad \frac{\text{viscous forces}}{\text{surface tension forces}}, \tag{1.5b}$$

$$\text{Weber number} \qquad We = \frac{\rho U^2 \ell}{\gamma} \qquad \frac{\text{inertia forces}}{\text{surface tension forces}}, \tag{1.5c}$$

$$\text{Ohnesorge number} \qquad Oh = \frac{\mu}{\sqrt{\rho \gamma \ell}} \qquad \frac{\text{viscous forces}}{\text{inertia and surface tension forces}}, \tag{1.5d}$$

where ρ is the density [kg/m^3]; μ, the dynamic viscosity [Pa·s]; U, the velocity [m/s]; ℓ, a characteristic length [m]; and γ, the surface tension [Nm^{-1}]. If a dimensionless parameter is much lager than a unity, we can assume that the force associated with the numerator is dominant.

1.1.3 Wetting and dewetting examples

Let us consider a dynamic situation of wetting and dewetting phenomena. We briefly mentioned earlier typical examples, i.e. moving droplets on a substrate by gravity or shear flow. Partial wetting and dewetting phenomena occur over a wide range of Reynolds numbers. For instance, at low Reynolds number, i.e. $Re \ll 1$, (a) the spreading of a liquid drop on a horizontal surface (Greenspan, 1978; Hocking and Rivers, 1982), (b) the sliding of a liquid drop on an inclined-plane by gravity (Le Grand et al., 2005; Limat and Stone, 2004; Podgorski et al., 2001; Snoeijer et al., 2005), (c) the movement of a drop on a horizontal surface by the external flow (Dussan et al., 1987), (d) the movement of a meniscus along a tube by the capillary effect (Huh and Mason, 1977), (e) the dewetting of the contact line of an evaporating droplet (Guéna et al., 2007; Poulard et al., 2003), and (f) the impact of a solid object through a liquid interface (Richardson, 1948). These studies are all assumed to be Stokes flow, i.e. with negligible inertia.

On the other hand, there are also examples of partial dewetting and dewetting at intermediate Reynolds number, i.e. $Re > 1$. When a high velocity ($U \approx 1$ m/s) liquid droplet ($R \approx 1$ mm) impacts on solid substrate, the Reynolds number is of order of 10^3 for water (Mani et al., 2010; Pasandideh-Fard et al., 1996). Mani et al. (2010) showed that the classical lubrication theory breaks down in this droplet impacting problem because of the compressibility of air. Additionally, in an industrial application, a confined liquid layer over a moving substrate (i.e. a wetting and dewetting flow structure) is used to improve spatial resolution of optical lithography, i.e. so-called immersion lithography (Mulkens et al., 2004; Owa and Nagasaka, 2008; Schuetter et al., 2006). In this case, the wetting and dewetting velocity increases up to the order of 1 m/s, i.e. $Re \sim O(100)$ for water (Kim et al., 2011; Riepen et al., 2008; Winkels et al., 2011). In these cases, we can not neglect the nonlinear acceleration terms, i.e. inertial effects.

1.1.4 Hydrodynamics issue: singularity

In wetting and dewetting problems, the liquid-air interface is moving with respect to the solid. Contact line dynamics remains one of the most difficult and disputed problems in fluid dynamics, because there is a singular point where air, liquid, and solid coexist. Landau and Levich (1942) first studied the problem of a withdrawal of a plate or fiber from a liquid bath. They observed that the viscous stress is logarithmically divergent at the singularity. Later on, Huh and Scriven (1971) proposed a hydro-dynamical model of the flow near a moving contact line assuming steady, two-dimensional flow, low Reynolds number, and a simplified straight interface of the fluid. According to their model, however, the no-slip condition at the singular point induces a flow close to a contact line, which leads to an energy dissipation that is logarithmically diverging. Many scholars have made a great effort to resolve the hydrodynamic singularity ever since. Two ideas are mainly used to remove the singularity issue: (1) a slip boundary condition at the contact line can be

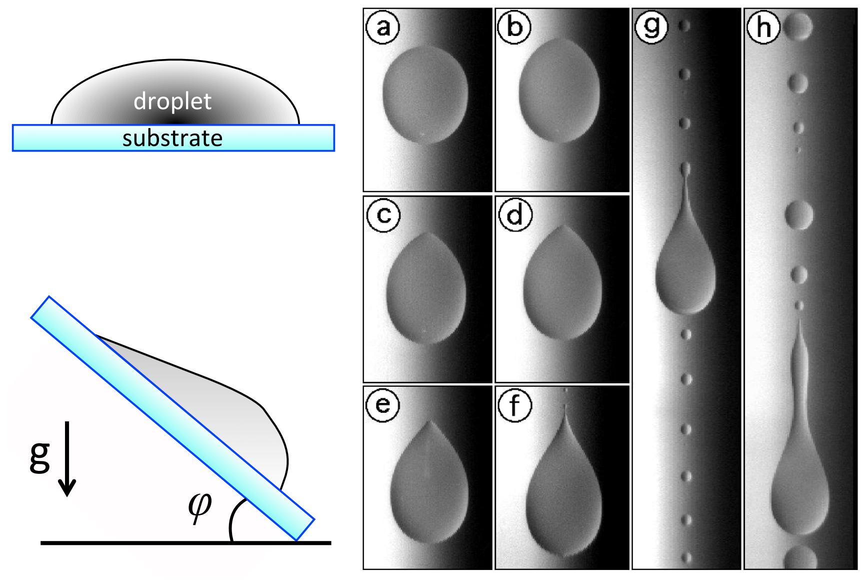

Figure 1.4: Example of gravity-driven liquid droplets on an inclined substrate. Left top: an equilibrium state of a droplet on a substrate. Left bottom: a droplet sliding down an inclined plate at a certain angle φ. Right: different shapes of drop sliding down a plate when increasing the inclination angle φ. Image taken from Podgorski et al. (2001).

applied (Brochard-Wyart and De Gennes, 1992) and (2) a partial wetting and dewetting structure near contact lines can be assumed between the macroscopic layer and the thin film (de Gennes, 1985).

1.2 Motivation[1]

Podgorski et al. (2001) described that the rear part of a gravity-driven droplet on an incline evolves from a round shape to a cusp shape when the contact line velocity (or the inclination angle φ) increases, as shown in figure 1.4. The shape transient of such a dewetting liquid droplet that is dragged over the substrate is an interesting phenomenon. Above a critical velocity, the droplet begins to break up ('pearling') at the downstream side of the main droplet (see figure 1.4(g) and (h)). This contact line instability is also encountered in industry, for instance in an immersion lithography machine. Recently, immersion lithography has been given serious attention within the semiconductor industry, because it enhances the optical resolution by replacing the air in the gap between a lens and a silicon-

---

[1] The content of this section has partly been presented in the JMBC news letter (Kim et al. 2010).

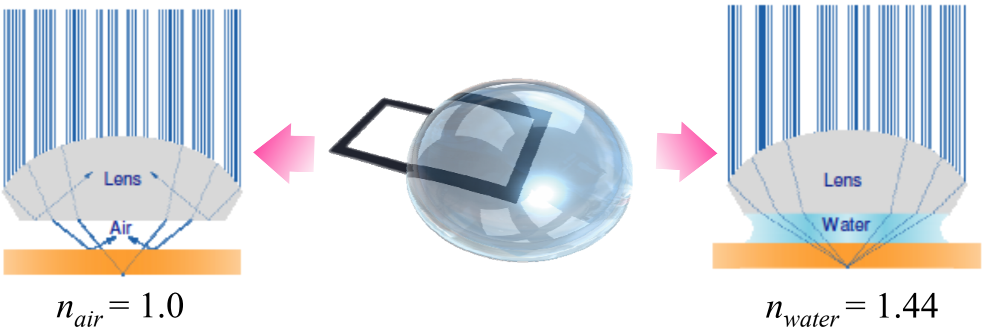

Figure 1.5: Schematic of an liquid immersion droplet in photolithography where n is the refractive index.

wafer with water, which has a higher refractive index ($n_{water} \approx 1.44$) for 193nm light, as shown in figure 1.5. The immersed liquid film thickness is of the order of hundreds micron. Current immersion systems can improve the optical resolution down to tens of nanometers, which is an enhancement of the spatial resolution by about 30-40 %, enabling sub-40-nm structure patterning (French and Tran, 2009).

Besides the advantage of higher optical resolution, immersion lithography also poses a couple of difficulties and challenges. In semiconductor production usually the silicon-wafer is moved underneath the optical lithographic lens. One of the key challenges in immersion lithography is to keep the liquid contained under the lens with extremely uniform properties with respect to fluid dynamics, temperature, and purity. Non-homogeneous liquid can cause several defects, which are classified into five cases: (a) process-induced defects, (b) watermark defects, (c) defects arising from bubbles in the fluid, (d) drying stain defects, and (e) particle-borne defects (French and Tran, 2009). Figure 1.6 summarizes some defect results (see comment at figure 1.6). In particular, losing liquid at the dynamic contact line and entrainment of air at the interface between liquid and surrounding air are potential risks for a high throughput and accurate next-generation lithography tools.

Taking this into consideration, a detailed study and understanding of the dynamic contact line is of utmost importance for better control of the liquid under the lens. Schuetter et al. (2007) presented an empirical model to predict a critical velocity depending on the substrate condition (see figure 1.7). They showed that the critical velocity is increased with the static receding contact angle. In other words, the droplet breakup occurs earlier on a hydrophilic substrate than on a hydrophobic surface. They also addressed that liquid loss is related to two mechanisms, i.e. pulling and inertial instabilities. At low velocities on the hydrophilic surface, the critical velocity is mainly governed by the film pulling velocity. A droplet breakup by inertial instability is frequently observed at high substrate accelerations and velocities on hydrophobic surfaces. The critical velocity consists of two

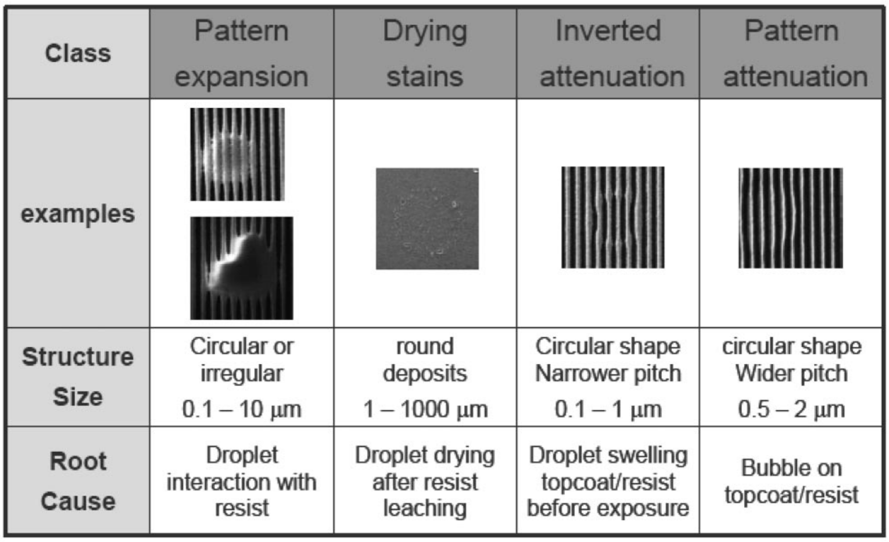

Class	Pattern expansion	Drying stains	Inverted attenuation	Pattern attenuation
examples				
Structure Size	Circular or irregular 0.1 – 10 µm	round deposits 1 – 1000 µm	Circular shape Narrower pitch 0.1 – 1 µm	circular shape Wider pitch 0.5 – 2 µm
Root Cause	Droplet interaction with resist	Droplet drying after resist leaching	Droplet swelling topcoat/resist before exposure	Bubble on topcoat/resist

Figure 1.6: Examples of defects produced during immersion lithography. Table taken from Mulkens et al. (2007).

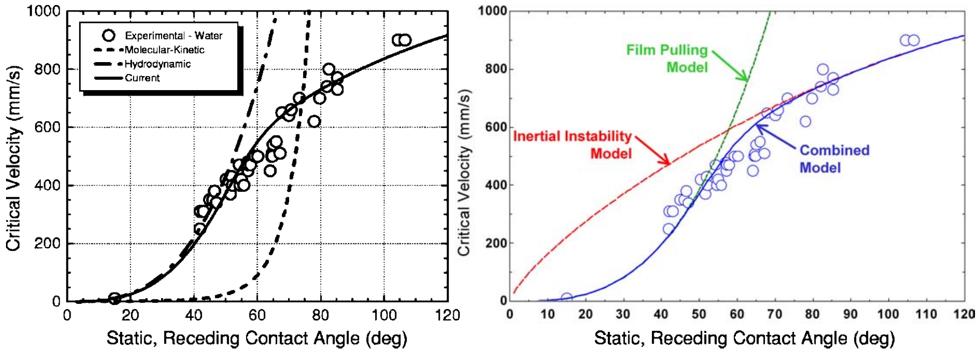

Figure 1.7: Immersion lithography I: the critical velocity depends on the static receding contact angle. Graphs taken from Schuetter et al. (2007) (left) and Harder (2007) (right).

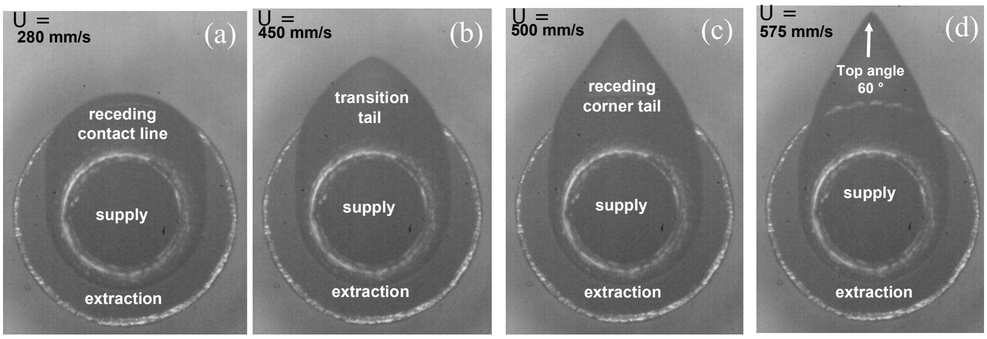

Figure 1.8: Immersion lithography II: different shapes (bottom view) of the immersion droplet on different substrate velocities U where the substrate is moving upward. Image taken from Riepen et al. (2008).

velocity components:

$$v_{crit} = \left(v_{fp}^{-m} + v_{in}^{-m}\right)^{-1/m} \tag{1.6}$$

where v_{fp} ($=C_1\theta^3(\gamma/\mu)$) is the film pulling velocity and v_{in} ($=C_2(\gamma/\mu)^{1/4}$ $(\gamma\kappa/\rho)^{3/8}$ $\sin^{3/4}\theta$) is the inertial instability velocity, where C_1 and C_2 are an empirical constant; θ, the receding contact angle; γ, the surface tension; μ, the dynamic viscosity; κ^{-1}, the capillary length. Furthermore, m is a parameter to fit the measurement results. This equation is obtained experimentally by Schuetter et al. (2007).

Riepen et al. (2008) reported the evolution of dynamic contact angles as a function of the velocity of the substrate. They used a simplified system that mimics the basic functioning of an immersion hood of an actual industrial system. To generate the immersion droplet, at the center of the simplified system, water is supplied and then water and air are simultaneously extracted through an annular trench around the inlet. They showed that the dewetting contact lines evolve from a round shape to a cusp shape, and even observed 'pearling' when the substrate velocity is further increased (Riepen et al., 2008). Furthermore, they reported that the droplet breakup apparently occurs when the top angle is 60° (see figure 1.8(d)). In this case, the wetting and dewetting velocity increases up to about 1 m/s, i.e. $Re \sim O(100)$ for water (Kim et al., 2011; Riepen et al., 2008). However, interestingly, the gravity-driven liquid droplet on an incline also begins to lose liquid behind the main droplet when the top corner angle between contact lines is 60° (Podgorski et al., 2001; Stone et al., 2002). In this case, the Reynolds number and capillary number are much smaller than unity. Furthermore, there are more similarities between the gravity-driven droplet at $Re \ll 1$ and the immersion droplet at $Re \sim O(100)$ (see chapter 4). It is still unclear how to explain the similarity in the different Reynolds number regimes. In the current problem, critical dimensionless numbers are estimated as below:

$$\text{Reynolds number} \qquad Re = \frac{\rho U \ell}{\mu} = \frac{1000 \times 1 \times 0.001}{0.001} = 1000 \tag{1.7a}$$

$$\text{Capillary number} \qquad Ca = \frac{\mu U}{\gamma} = \frac{0.001 \times 1}{0.072} = 0.0139 \tag{1.7b}$$

$$\text{Weber number} \qquad We = \frac{\rho U^2 \ell}{\gamma} = \frac{1000 \times 1^2 \times 0.001}{0.072} = 13.9 \tag{1.7c}$$

$$\text{Ohnesorge number} \qquad Oh = \frac{\mu}{\sqrt{\rho \gamma \ell}} = \frac{0.001}{\sqrt{1000 \times 0.072 \times 0.001}} = 0.0037 \tag{1.7d}$$

where the density $\rho = 10^3$ kg/m^3; the dynamic viscosity $\mu = 10^{-3}$ Pa·s; the critical velocity U = 1 m/s; the characteristic length $\ell = 10^{-3}$ m; and the surface tension $\gamma = 72\times 10^{-3}$ Nm^{-1}.

1.3 Particle Image Velocimetry towards free-surface

A flow measurement technique is very applicable to study hydrodynamics problems. In particular, particle image velocimetry (referred to as PIV) is the most powerful method to quantitatively measure velocity components (Adrian and Westerweel, 2010). For conventional PIV, tracer particles are added to the flow. The particles are illuminated twice by a pulsed laser in a plane or volume. Then, the emitted light from the particles is recorded by a camera. From these two sequential records, a velocity vector is determined by the particle displacement within the time between the light pulses, as shown in figure 1.9. Then, the local 2D (i.e. in-plane) velocity V is obtained from the particle displacement (Δx) within the exposure time delay (Δt).

To measure the out-of-plane velocity components in a single 2D plane, stereoscopic-PIV has been introduced (Arroyo and Greated, 1991; Prasad, 2000; Prasad and Adrian, 1993; Willert, 1997). The tracer particle motions are recorded by two cameras having a different viewing angle. Each camera observes a different projection of the tracer particle motion. The perspective distortion of particle images is corrected by a calibration and then the three velocity vector components can be obtained (Raffel et al., 2007). Besides, there are also different types of three-dimensional three-component (referred to as 3D-3C) velocimetry techniques (see the introduction of chapters 2 and 3).

In the PIV experiment, if we have a discontinuity of the refraction index at the phase interface, it makes the measurement very difficult. For a liquid-liquid interface, the refractive index matching is used to correct a distortion at the interface (Budwig, 1994). However, if there is a gas-liquid interface, it is impossible to match the refractive index to a different phase. Kang et al. (2004) tried to measure the lateral flow fields of an evaporating droplet (the experimental setup is similar as shown in the black-dashed box of figure 1.10). They performed the image and velocity mapping method based on a direct ray tracing method

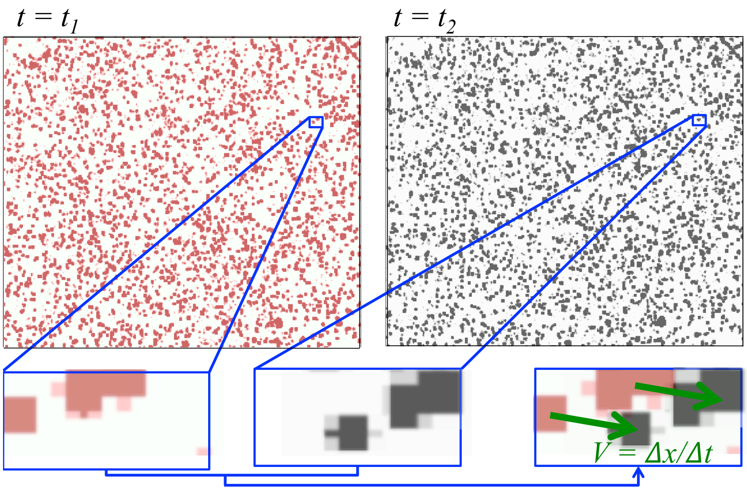

Figure 1.9: Comparison of schematic of particle image velocimetry. Particle images are recorded at $t = t_1$ and t_2. The images are artificially colored red and black, respectively. Overlap of two image intensities in the blue boxes are located at the same position. The overlapped image represents the particle displacement, $\Delta x = V \cdot \Delta t$.

to correct the internal flow field distorted by the droplet surface. However, it is still difficult to resolve the velocity field close to the gas-liquid interface (the most distorted area), as shown in the purple region of figure 1.10. This is due to the reflection and refraction at the free surface. The laser light is also refracted through the gas-liquid interface. To observe the flow field inside the droplet without any distortion, the measurement domain should have a constant refractive index across the different phase interface. Therefor, it is better to observe the droplet flow pattern from below where the liquid phase contacts the transparent solid phase. The PIV setup could be arranged as indicated by the red-dashed box of figure 1.10. In this case, to measure the three-dimensional fluid motion by conventional planar PIV, the measurement domain must be scanned by moving the position of the focal-plane. Alternatively, it is also possible to use 3D velocimetry techniques, for instance 3D particle tracking velocimetry (Maas et al., 1993), tomographic PIV (Elsinga et al., 2006), holographic PIV (Hinsch, 2002), and defocused PIV (Pereira et al., 2000).

1.4 Objectives and scope of this thesis

The objective of the current research is to study dewetting flow at intermediate Reynolds number, in particular for a liquid immersion droplet. From an industrial point of view, the droplet breakup problem is one of the crucial issues in the immersion lithography

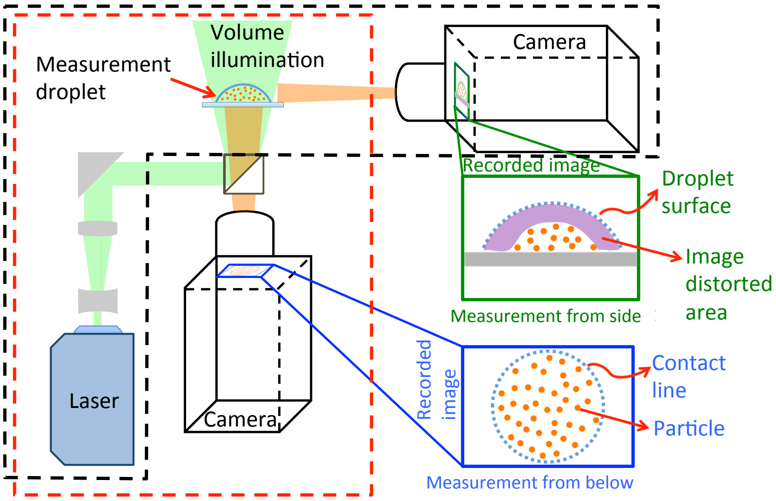

Figure 1.10: Schematic of the PIV setup for the measurement of the flow within droplet. The black-dashed box shows the side-view PIV measurement. This allows to measure the lateral fluid motion but the image can be distorted near the droplet interface. The red-dashed box presents the below PIV measurement, i.e. bottom-view.

machine. It is required to understand the droplet breakup mechanism to prevent or control the instability problem. From an academic point of view, surprisingly enough, interesting similarity results are observed between different dewetting flow problems, i.e. the gravity-driven liquid droplet on an incline with $Re \ll 1$ and the liquid immersion droplet at $Re \sim O(100)$. However, so far there is no satisfactory explanation for this. To accomplish a better understanding of this problem, we perform an experimental, theoretical, and numerical analysis.

When a partial wetting and dewetting flow problem has a thin-film flow structure, we can use a lubrication approximation. To exploit this approximation the key requirement is that the aspect ratio $\epsilon = h/L$ is small, $\epsilon \ll 1$, where the characteristic film thickness (gap) is h and the length scale is L. Then, even though the Reynolds number is much larger than unity, if $Re{\cdot}\epsilon$ is much smaller than unity, we can assume that inertia is negligible, i.e. we are dealing with Stokes flow (Reynolds, 1886; White, 2005). However, the present problem (the liquid immersion droplet) has a relatively high Reynolds number ($Re \sim O(100)$) and the lubrication approximation is not applicable due to $Re{\cdot}\epsilon > 1$ (see chapter 4). Therefore, it is difficult to apply a standard theoretical approach. Therefore, an experimental approach has to be performed to understand the internal flow pattern near the moving contact line.

In this thesis, to obtain the flow field, we use a multiple camera measurement technique.

Four CCD cameras are mounted below a customized stereo microscope and all cameras view the same plane. The measurement droplet has a volume of approximately 1 μl and the droplet height is of the order of 100 μm. A customized system for the microfluidic flow measurement has been developed to obtain 3D-3C velocity vectors. This study is the first to measure the micro scale flow pattern involving wetting and dewetting phenomena by using multiple cameras. We perform tomographic particle image velocimetry (referred to as Tomo-PIV) (Elsinga et al., 2006) and 3D particle tracking velocimetry (referred to as 3D-PTV) (Maas et al., 1993). Furthermore, we evaluate the velocity measurement uncertainty and accuracy for both methods. Based on these PIV experimental results, we gained insight into the flow pattern allowing us to derive a new theoretical model to describe this wetting and dewetting phenomena.

Moreover, to investigate droplet breakup, we observe the droplet shape from side and bottom views by means of shadowgraphy. Based on these results, we perform a scaling analysis to characterize the dominant effects in this problem. This allows us to simplify the governing equations. Based on the flow pattern and scaling, we develop a theoretical model for $Re{\cdot}\epsilon > 1$. In this thesis, we do not deal with intermolecular forces, i.e. long-range forces. Here, we consider a partial wetting and dewetting problem on a macroscopic scale.

From the experimental results, we are able to understand the internal flow pattern of the immersion droplet over the moving substrate. The results provide the basis of the modified lubrication model. However, the experimental approach has some minor limitations. To obtain experimental data for every case requires an extensive work. The immersion droplet instability might be related to many variables, e.g. the working fluid, the substrate, the design of the immersion hood device, and so on. In this sense, numerical simulations provide some advantages over experiments, such as the complex shape of the immersion hood device and high efficiency to obtain the data. In this sense, we introduce an idea for the simplified numerical model to gain a better understanding of the various internal flow patterns that depends on the immersion hood design.

1.5 Outline of the thesis

A partial dewetting flow problem, in particular that of a liquid immersion droplet, is studied by means of experimental, numerical, and theoretical methods. The outline of this thesis is as follows:

In chapter 2, we describe a Tomo-PIV system for the measurement of the full three-dimensional velocity field with all three components in a droplet over a stagnant and a moving surface.

In chapter 3, we quantitatively compare results of Tomo-PIV and 3D-PTV. In order to assess the results, we investigate (a) the mass conservation in the droplet, (b) the reconstructed 3D particle distributions, (c) the divergence of the flow, and (d) velocity profiles.

In chapter 4, we perform a high-speed shadowgraphy measurement and Tomo-PIV. From the shadowgraphy result, we perform a scaling analysis and then we report that inertia, pressure, and viscous forces are balanced together in the present problem. Based on the scaling analysis and flow pattern analysis, we develop a modified lubrication theory for the dewetting corner at $Re{\cdot}\epsilon > 1$. The model describes that the dewetting corner has a three-dimensional conical structure. Moreover, it shows that there is a relation between the corner opening angle and the dynamic receding contact angle. With the modified lubrication model, we obtain a self-similar flow pattern near the dewetting contact lines. Lastly, we compare analytical results for two different flow configurations, i.e. the gravity-driven droplet on an incline and the immersion droplet.

In chapter 5, we introduce a simplified numerical model for the immersion droplet. We use a zero flux boundary condition for the gas-liquid interface. The numerical results are compared with the experimental results.

In chapter 6, the thesis is closed with a summary of conclusions and discussion.

Chapter 2, 3, and 4 have been submitted or published for publication in peer-reviewed journals. Chapter 5 has been presented for oral presentation at a conference. The theoretical and numerical results are validated by the experimental results. These chapters are self-contained and can be read individually.

1.6 Bibliography

R. J. Adrian and J. Westerweel. *Particle Image Velocimetry.* Cambridge University Press., 2010.

M. P. Arroyo and C. A. Greated. Stereoscopic particle image velocimetry. *MEAS SCI TECHNOL*, **2**, 1181, 1991.

F. Brochard-Wyart and P. G. De Gennes. Dynamics of partial wetting. *ADV COLLOID INTERFAC*, **39**, 1, 1992.

R. Budwig. Refractive index matching methods for liquid flow investigations. *EXP FLUIDS*, **17**, 350, 1994.

P. G. De Gennes, F. Brochard-Wyart and D. Quéré. *Capillarity and wetting phenomena: drops, bubbles, pearls, waves.* Springer Verlag, 2004.

V. Dussan et al. On the ability of drops to stick to surfaces of solids. Part 3. the influences of the motion of the surrounding fluid on dislodging drops. *J FLUID MECH*, **174**, 381, 1987.

G. E. Elsinga et al. Tomographic particle image velocimetry. *EXP FLUIDS*, **41**, 933, 2006.

R. French and H. Tran. Immersion lithography: photomask and wafer-level materials. *ANNU REV MATER RES*, **39**, 93, 2009.

P. G. de Gennes. Wetting: statics and dynamics. *REV MOD PHYS*, **57**, 827, 1985.

H. Greenspan. On the motion of a small viscous droplet that wets a surface. *J FLUID MECH*, **84**, 125, 1978.

G. Guéna, C. Poulard and A. M. Cazabat. The leading edge of evaporating droplets. *J COLLOID INTERF SCI*, **312**, 164, 2007.

P. M. Harder. *Physical and thermal behaviors of dynamic three-phase contact lines*. University of Wisconsin–Madison, 2007.

K. D. Hinsch. Holographic particle image velocimetry. *MEAS SCI TECHNOL*, **13**, R61, 2002.

L. Hocking and A. Rivers. The spreading of a drop by capillary action. *J FLUID MECH*, **121**, 425, 1982.

C. Huh and S. G. Mason. The steady movement of a liquid meniscus in a capillary tube. *J FLUID MECH*, **81**, 401, 1977.

C. Huh and L. E. Scriven. Hydrodynamic model of steady movement of a solid/liquid/fluid contact line. *J COLLOID INTERF SCI*, **35**, 85, 1971.

K. H. Kang et al. Quantitative visualization of flow inside an evaporating droplet using the ray tracing method. *MEAS SCI TECHNOL*, **15**, 1104, 2004.

H. Kim et al. Full 3D-3C velocity measurement inside a liquid immersion droplet. *EXP FLUIDS*, **51**, 395, 2011.

L. Landau and B. Levich. Dragging of a liquid by a moving plate. *ACTA PHYSICOCHIM URS*, **17**, 1942.

N. Le Grand, A. Daerr and L. Limat. Shape and motion of drops sliding down an inclined plane. *J FLUID MECH*, **541**, 293, 2005.

L. Limat and H. A. Stone. Three-dimensional lubrication model of a contact line corner singularity. *EUROPHYS LETT*, **65**, 365, 2004.

H. G. Maas, A. Gruen and D. Papantoniou. Particle tracking velocimetry in three-dimensional flows. *EXP FLUIDS*, **15**, 133, 1993.

M. Mani, S. Mandre and M. P. Brenner. Events before droplet splashing on a solid surface. *J FLUID MECH*, **647**, 163, 2010.

J. Mulkens et al. Benefits and limitations of immersion lithography. *J MICROLITH MICROFAB*, **3**, 104, 2004.

J. Mulkens et al. Defects, overlay and focus performance improvements with five generations of immersion exposure systems. *SPIE Optical Microlithography XX, v6520, San Jose, USA*, 2007.

S. Owa and H. Nagasaka. Immersion lithography: its history, current status and future prospects. In *P SPIE*, volume 7140, 714015, 2008.

M. Pasandideh-Fard et al. Capillary effects during droplet impact on a solid surface. *PHYS FLUIDS*, **8**, 650, 1996.

F. Pereira et al. Defocusing digital particle image velocimetry: a 3-component 3-dimensional DPIV measurement technique. Application to bubbly flows. *EXP FLUIDS*, **29**, 78, 2000.

T. Podgorski, J. M. Flesselles and L. Limat. Corners, cusps, and pearls in running drops. *PHYS REV LETT*, **87**, 36102, 2001.

C. Poulard, O. Benichou and A. M. Cazabat. Freely receding evaporating droplets. *LANGMUIR*, **19**, 8828, 2003.

A. K. Prasad. Stereoscopic particle image velocimetry. *EXP FLUIDS*, **29**, 103, 2000.

A. K. Prasad and R. J. Adrian. Stereoscopic particle image velocimetry applied to liquid flows. *EXP FLUIDS*, **15**, 49, 1993.

M. Raffel, C. E. Willert and J. Wereley S.and Kompenhans. *Particle image velocimetry: a practical guide (experimental fluid mechanics)*. Springer Verlag, 2007.

O. Reynolds. On the theory of lubrication and its application to mr. beauchamp tower's experiments, including an experimental determination of the viscosity of olive oil. *P R SOC LONDON*, **40**, 191, 1886.

E. G. Richardson. The impact of a solid on a liquid surface. *P PHYS SOC*, **61**, 352, 1948.

M. Riepen, F. Evangelista and S. Donders. Contact line dynamics in immersion lithography-dynamic contact angle analysis. In *Proc. 1st Euro. Conf. Microfluidics*, 2008.

S. Schuetter et al. Measurements of the dynamic contact angle for conditions relevant to immersion lithography. *J MICROLITH MICROFAB*, **5**, 023002, 2006.

S. D. Schuetter, T. A. Shedd and G. F. Nellis. Prediction of the velocity at which liquid separates from a moving contact line. In *SPIE*, 2007.

J. H. Snoeijer et al. Self-similar flow and contact line geometry at the rear of cornered drops. *PHYS FLUIDS*, **17**, 072101, 2005.

H. A. Stone et al. Singularité anguleuse d'une ligne de contact en mouvement sur un substrat solide: Corner singularity of a contact line moving on a solid substrate. *C R PHYS*, **3**, 103, 2002.

F. M. White. *Viscous Fluid Flow*. McGraw-Hill, 2005.

C. Willert. Stereoscopic digital particle image velocimetry for application in wind tunnel flows. *MEAS SCI TECHNOL*, **8**, 1465, 1997.

K. G. Winkels et al. Receding contact lines: From sliding drops to immersion lithography. *EUR PHYS J-SPEC TOP*, **192**, 195, 2011.

T. Young. An essay on the cohesion of fluids. *Philosophical Transactions of the Royal Society of London*, **95**, 65, 1805.

CHAPTER 2

EXPERIMENT I: FULL 3D-3C VELOCITY MEASUREMENT INSIDE A LIQUID IMMERSION DROPLET[1]

Abstract

We describe a tomographic PIV system for the measurement of the internal flow in a droplet over a stagnant and a moving surface. The flow condition is representative of the flow in an immersion droplet applied in a liquid-immersion lithography machine. We quantify the accuracy and reliability of the measurements, and compare the shape of the reconstructed measurement volume to shape measurements by means of shadowgraphy. First results indicate the internal flow pattern near the receding contact line, showing a small recirculation region.

2.1 Introduction

In semiconductor fabrication, immersion lithography has been considered as a means to further improve the spatial resolution. By replacing the air ($n_{air} \approx 1.0$) in the gap between a lens and an object (a silicon wafer) with water ($n_{water} \approx 1.44$) for 193nm UV light the optical resolution in the image plane is enhanced (French and Tran, 2009). The spatial resolution is given by $\delta = k\lambda/\mathrm{NA}$ where k is the process coefficient with $k \simeq O(1)$, λ the light wavelength, and NA the numerical aperture of the lens, $\mathrm{NA} = \mathrm{n} \cdot \sin\theta$, where θ is the half viewing angle. Current immersion systems can improve the resolution quality down to the order of tens of nanometers (Mulkens et al., 2004; Owa and Nagasaka, 2008), which is an enhancement of about 30-40 %.

---

[1] The content of this chapter has been published in Experiments in Fluids (Kim et al. 2011). Copyright © Springer.

Besides the advantage of higher optical resolution, immersion lithography also poses a couple of difficulties and challenges. In semiconductor production usually the substrate (wafer) is moved underneath the optical lithographic lens. The biggest challenge then is to keep the liquid phase uniform without defects. With speeds in the range of 1 m/s, the main concerns for wafer defects are: (1) water left behind (watermarks), and (2) a loss of resist-water adhesion (air gap) and bubble entrainment at the leading edge of the immersion droplet. To further increase yield, manufacturers of lithographic immersed-lens scanners wish to increase the wafer speed even further. Schuetter et al. (2006) studied the transitions of the dynamic contact angle for the immersion droplet until the maximum substrate speed, about 0.4 m/s, where the droplet starts to break up. Riepen et al. (2008) reported the evolution of dynamic contact angles as a function of the rotational speed where the substrate is rotated with respect to a liquid immersion droplet. The receding contact angles evolve from a round shape to a cusp shape when the substrate has a velocity less than 0.73 m/s. Above the critical velocity, the liquid droplet begins to break up (‘pearling’) at the downstream side of the immersion droplet. This critical velocity depends on fluid, gap heights, contact angles, and so on.

In a different geometry, similar studies were performed on a moving droplet on an inclined substrate, albeit at a much lower Reynolds number ($\mathrm{Re} = O(1)$), i.e. almost within the Stokes flow regime. Podgorski et al. (2001) showed that the initially rounded perimeter of the drop exhibits a singularity at the rear of the drop when the capillary number exceeds a critical value. Snoeijer et al. (2005) attempted to apply conventional planar particle image velocimetry (PIV) to measure the internal flow field. However, the measured flow field rather represents the average fluid motion over the whole depth of the droplet. A theoretical model was suggested to understand the mechanism of the droplet motion. In the Stokes flow regime, the theoretical model is derived from the lubrication theory taking into account the the small slope of the liquid-air interface with respect to the solid plane (Limat and Stone, 2004). However, in the case of the immersion droplet at a higher value of the Reynolds number, it is difficult to obtain a theoretical model.

Therefore, to allow for a further understanding of the fluid motion in a liquid immersion droplet under realistic conditions, the droplet flow field needs to be investigated experimentally. Kang et al. (2004) performed a quantitative measurement of lateral flow fields of an evaporating droplet by a direct ray tracing method and Lu et al. (2008) measured the internal flow of electro-wetting-on-dielectric (EWOD) driven droplet by conventional PIV. However, due to the complex nature in contact line dynamics, the volumetric measurement of all velocity components of the flow inside the entire droplet shape is desirable. To measure the volumetric flow field several methods are proposed. Scanning light-sheet (Brücker, 1995), holography (Hinsch, 2002; Sheng et al., 2009), defocusing digital particle image velocimetry (DDPIV) (Pereira et al., 2000, 2007), tomographic particle image velocimetry (Elsinga et al., 2006) and 3D particle tracking velocimetry (Maas et al., 1993) are the most typical approaches. Recently, Pereira et al. (2007) investigated the 3D flows of evaporating droplet by using μDDPIV with an inverted microscope.

In this paper, the internal flow of the liquid immersion droplet on a moving substrate is investigated by means of tomographic PIV. This measurement technique is capable of simultaneously measuring all three velocity components (referred to as 3D-3C). The paper is structured as follows. First, the experimental setup and measurement technique are explained in detail. Next, the pre- and post-processing for 3D-3C data will be elucidated followed by a discussion of the measurement accuracy based on the assessment of the relative measurement examined by means of the continuity equation. Tomographic PIV is applied to determine the complex flow topology of the immersion droplet at $\mathrm{Re} = 200$ for the first time. From this result, we can assess the internal flow field of the liquid immersion droplet. The results may lead to strategies that can achieve the flow control and to optimized designs of the immersion lithographic system.

2.2 Experimental setup

The experimental setup is shown in figure 2.1. A transparent glass wafer with a highly uniform hydrophobic surface coating (static contact angle, $\theta_s \approx 90°$) is used. The working fluid is distilled water with a dynamic viscosity $\mu = 10^{-3}$ Pa·s, a surface tension $\gamma = 70$ mN/m, and a density $\rho = 10^3$ kg/m^3. We consider a liquid immersion droplet with a diameter (D) of 2 mm and a height (h) of 200 μm as shown in figure 2.2(a). The wafer spins with a velocity of V_w=1.0 m/s at the position of the droplet, so that the flow conditions are characterized by a capillary number ($\mathrm{Ca} = \mu V_w/\gamma$) of 0.014 and a Reynolds number ($\mathrm{Re} = \rho V_w h/\mu$) of 200. At these conditions the immersion droplet exhibits a wedge shape at the rear. In particular, figure 2.2(b-c) shows that the droplet begins to lose mass (referred to as 'pearling') at a critical velocity of around 1.4 m/s.

Figure 2.3 depicts a schematic of the experimental facility. A constant immersion film (droplet) is generated by a so-called immersion needle as shown in the red dashed line on the top right in figure 2.3. The measurement volume coincides with the total droplet volume. At the center of the immersion needle, the working fluid is supplied to the droplet. It is extracted through an annular trench around this center supply inlet. This simplified configuration represents a more complex immersion hood of an actual lithography machine. The inlet volume flow rate is constant at a rate of 39.34 ml/min with an uncertainty of ±2 % of the full scale. To extract air and liquid at the same time through the annulus, a vacuum pressure of -0.5 bar is applied during the measurements. This condition generates a certain constant droplet volume for both a moving and a stagnant wafer. Furthermore, the immersion needle is installed near the edge of the 12 inch wafer, which spins with a constant angular velocity that results in a constant velocity at the

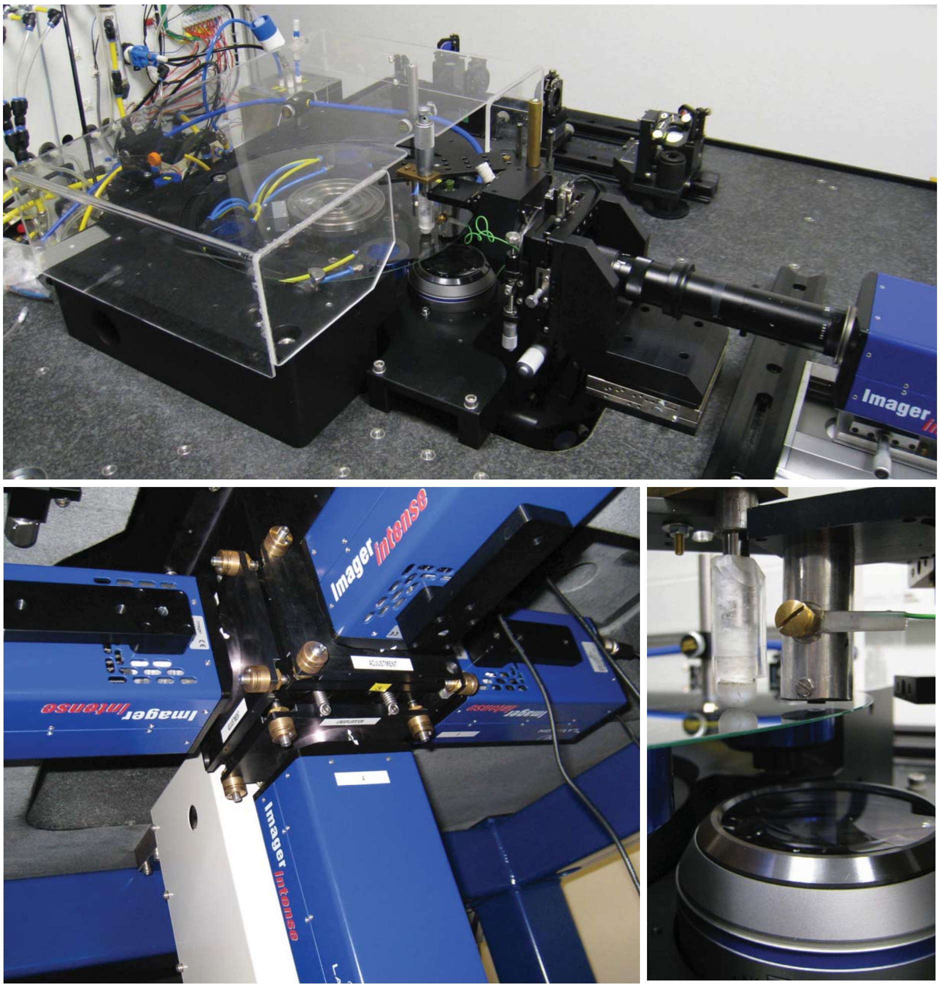

Figure 2.1: Illustrations of the experimental setup. Top: an overview of the facility. Bottom left: four PIV cameras are mounted on a custom-made microscope at the bottom of the set-up. Bottom right: the customized stereo-microscope, simplified immersion hood and pre-loaded device.

position of the droplet. Due to the large radial droplet position, the local movement of the wafer with respect to the needle can be considered nearly uniform translational. The surface of the immersion needle is aligned with the wafer surface in parallel as much as possible. The rotation table consists of a vacuum chuck at the center to hold and rotate the wafer. Four vacuum pre-loaded (VPL) air bearings support the horizontal position and

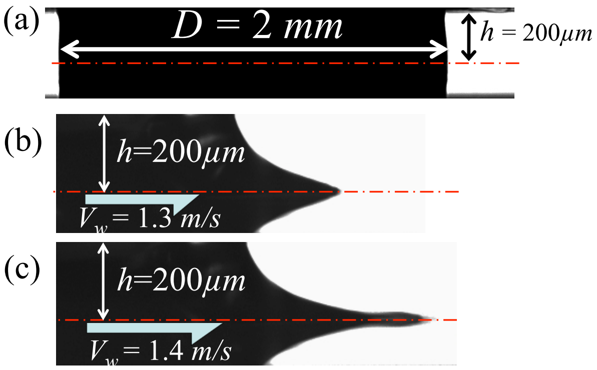
(a)
D = 2 mm
h = 200µm
(b)
h=200µm
Vw = 1.3 m/s
(c)
h=200µm
Vw = 1.4 m/s

Figure 2.2: Shadowgraphy results: the side view of (a) the entire liquid immersion droplet on the stagnant substrate ($V_w = 0$ m/s), (b) the tail of the immersion droplet on the moving substrate with $V_w = 1.3$ m/s, and (c) the tail of the immersion droplet on the moving substrate with $V_w = 1.4$ m/s. The dash-dot lines indicate the surface of the substrate(wafer).

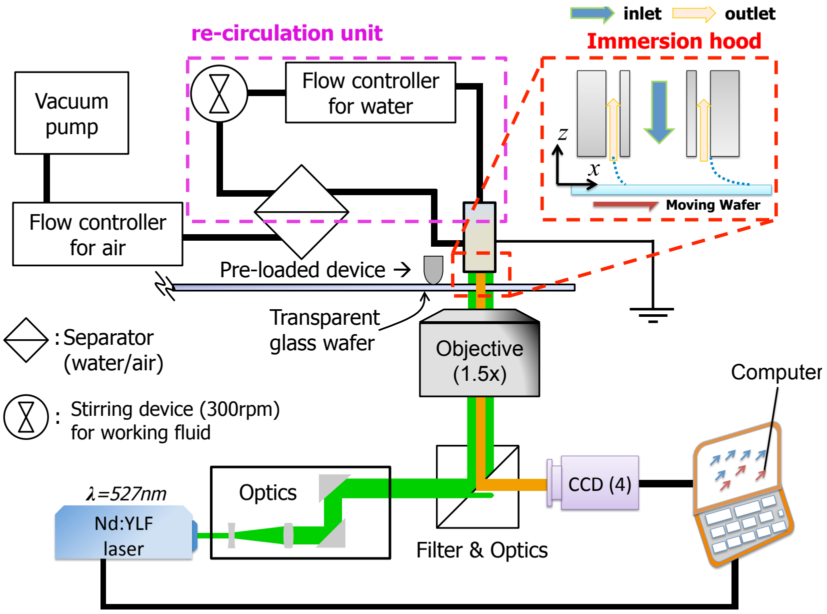
inlet
outlet
re-circulation unit
Immersion hood
Vacuum pump
Flow controller for water
Flow controller for air
z
x
Moving Wafer
Pre-loaded device
Transparent glass wafer
: Separator (water/air)
: Stirring device (300rpm) for working fluid
Objective (1.5x)
Computer
λ=527nm
Nd:YLF laser
Optics
CCD (4)
Filter & Optics

Figure 2.3: Schematic of the experimental setup. The upper half shows the liquid immersion droplet system consisting of the simplified immersion hood and the flow controller for the inlet and outlet flows. In addition, the lower half shows the stereoscopic measurement system.

level of the wafer.

For the visualization of the motion of the fluid inside the droplet, the re-circulating fluid is seeded with 1.28 μm tracer particles (Microparticle GmbH) that are fluorescent (Rhodamine-B) and that have a polyethylene glycol (PEG) coating. This coating avoids particle coagulation and attachment of particles to the wafer surface and to the free droplet surface. The fluorescence is excited by illumination with laser light from a pulsed frequency-doubled Nd:YLF laser which emits light with a wavelength of 527 nm. A separate stirring device maintains a homogeneous particle density. The PEG coated particles in water possess a slightly negative surface charge, whereas the immersion needle showed a weak positive charge promoting the attachment of particles to the surface. Therefore, the immersion needle is grounded to maintain electrical neutrality which reduces the number of particles sticking to the surface significantly.

The optimal particle image density is a compromise between the spatial resolution, the number of ghost particles, and the cross-correlation signal-to-noise ratio. The inflow impinges vertically downward on the wafer, and the outflow is extracted upward as shown in figure 2.4. Hence, the illumination with the laser through the microscope lens is parallel to the inflow and outflow directions. Hence, the laser beam illuminates the whole droplet. As a consequence, the background noise reaches a rather high level, which requires a proper image processing to reduce the effects of image background noise (see Sect. 2.3.1). The resulting image density (N_I) is 5.38×10^{-1}, $N_I \equiv CA_I \Delta z_0 / M_0^2$, where C is the mean number of particles per unit volume [m^{-3}], M_0, the magnification of the lens, Δz_0, the depth-of-field [m], and A_I, the image interrogation area [m^2]. In this experiment, the particle volume fraction is 2.5 % in aqueous suspension of 0.2 ml and then the particles are diluted in 500 ml distilled water. In the present condition, there is a low image density condition, $N_I < 1$. Directly counting particle images from raw images yields a value of around 0.034 ppp (particles per pixel) which corresponds to a source density $N_S \simeq 0.09$. The whole pre- and post-processing and calibration procedures are performed by means of a commercial code (Davis 7.4, LaVision GmbH).

For the velocity measurements we apply four CCD cameras, each with a resolution of 1376 × 1040 pixels and a 12-bit dynamic range. In this experimental condition, the equivalent dimension of a single pixel in the object domain is almost 4 μm. The camera (LaVision Imager Intense) has a high quantum efficiency of about 48% at 580 nm. To observe the flow field inside the droplet, the entire droplet volume needs to be accessed without any distortion for instance caused by reflection or refraction at the free surface. Therefore, four cameras are mounted on an inverted custom-made microscope. The optical path of each camera is off-axis through a single microscope objective lens with a magnification of 1.5. The offset angle between the optical axes of the cameras is about $\alpha \approx 20°$, as shown in figure 2.5. The laser beam diameter L_d is almost 5 mm. As shown in figure 2.5, the custom-made microscope is installed below at about 30 mm from the wafer surface. The depth-of-field is given approximately by $\Delta z_0 \cong 4(1+1/M_0)^2 f^{\#2} \lambda$, where Δz_0 is the depth-of-field; M_0, the magnification of the lens; $f^{\#}$, the f-number of the lens; λ, the

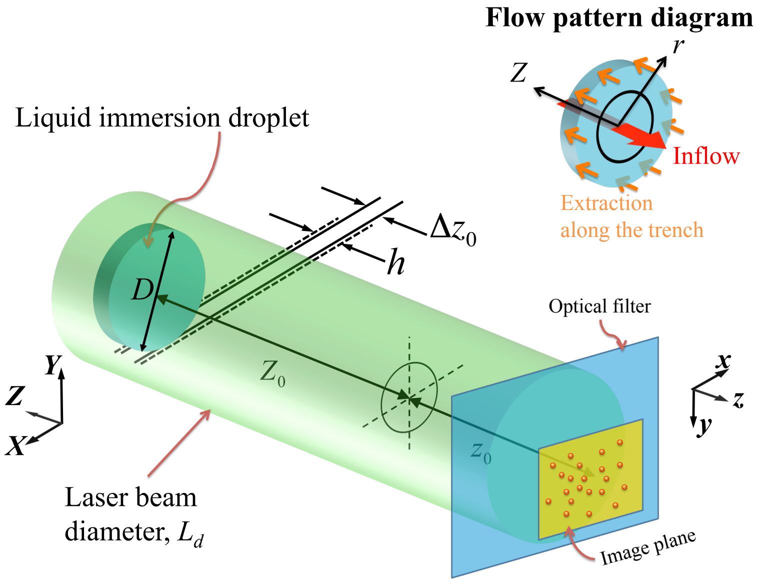

Figure 2.4: Schematic of the volume illumination for the immersion droplet where δz is the depth of field, h the height of the droplet, D the diameter of the droplet. At the top right, a close-up of the stationary droplet with the cylindrical coordinate system (r, θ, Z) is given.

wavelength of the light. For the given optical parameters we have $\Delta z_0 \approx 120$ μm.

The wafer is provided from Silicon Valley Microelectronics, Inc. and has a diameter of 300±0.3 mm and a local thickness of 0.70±0.05 mm. A highly uniform hydrophobic surface wafer that is coated with a photoresist is applied by ASML Holding NV. To our best knowledge, there are no glass-wafers, with a global flatness at a micron precision within the domain of commercial mass products. Only special custom-made wafers at extremely high price levels might provide values of overall flatness in the order of only a few micron. Therefore, for a constant droplet height, we applied a mechanical device that maintains a fixed reference position of the substrate. To establish this, we first record the height deviation of the edge of the wafer from the lateral camera as a function of time, so that we can obtain the topological characteristics of the wafer. Then, to control the height deviation, we properly mount a mechanical limitation to slightly push the wafer to a certain distance below a reference position (50 μm proved to be sufficient). Owing to this device, a global flatness of the wafer during rotation is controlled within ± 1 μm as shown in figure 2.6. The input velocity (V_w) is a nominal value of the system. Therefore, we determine the rotational speeds by measuring the topological characteristics of the wafer as a function of time. Hence, the measured wafer speed (V_m) has the uncertainty around 0.7 % compared with the nominal velocity on the system, as shown in Table 1. Additionally,

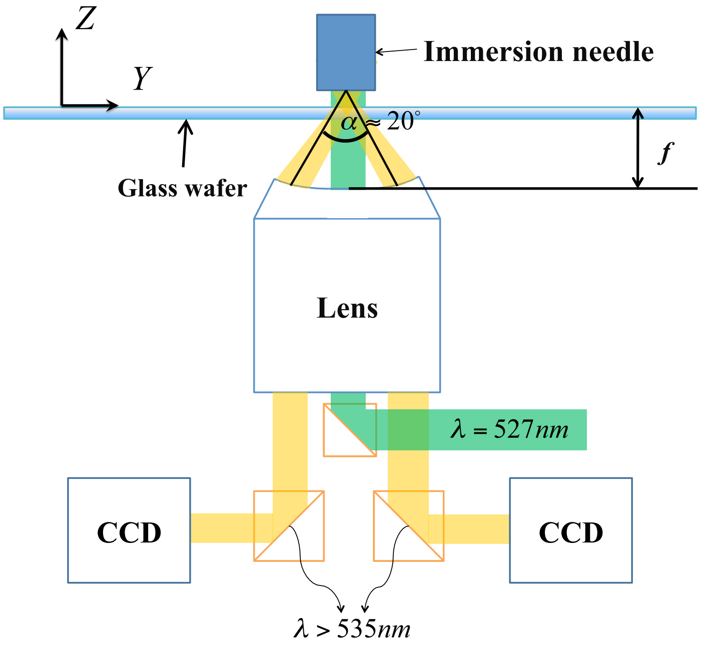

Figure 2.5: The geometry of the cross-sectional stereo microscope with CCD cameras. The focal length f is about 31 mm and the inner aperture is about 7 mm inside the lens. The particles inside the immersion droplet are volumetrically illuminated at 527 nm wavelength. The optical filters installed in front of each CCD camera only transmit light with wavelengths longer than 535 nm.

since the photoresist coating wafer is very sensitive to contact with water, the duration of the contact with water should be minimized.

2.3 Pre- and post-processing for 3D-3C data

2.3.1 Image processing

As can be seen in figure 2.4, the entire droplet volume is illuminated by using laser light passing into the droplet parallel to the inflow and outflow direction. As a consequence, parts of the flow field inside the water supply device, i.e., a flow region located vertically above the droplet volume, are also being illuminated, causing a rather strong background illumination (see figure 2.7(a)). The image-processing steps necessary to minimize this background illumination are as follows. The main steps are based on spatial and temporal

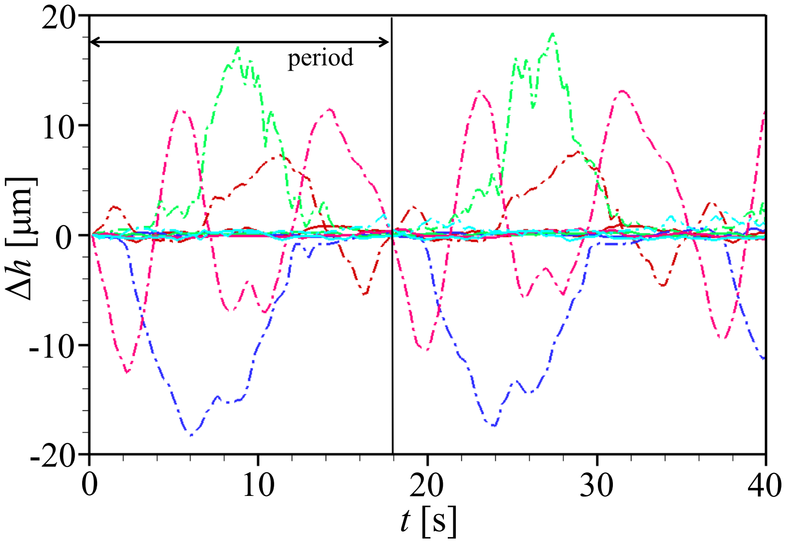

Figure 2.6: Effect of the pre-loaded device. The height deviation (Δh) is examined by measuring the topological characteristics of the edge of the wafer as a function of time. All dash-dot lines indicate the variation of the glass wafer without the pre-loaded device being applied, solid lines present the controlled results with the pre-loaded device lowered on the wafer surface.

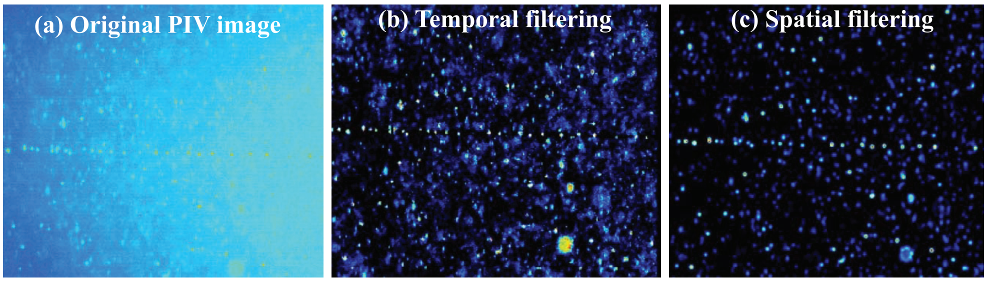

Figure 2.7: Effects of the image processing. (a) Original PIV image; (b) image after temporal filtering; (c) after additional spatial filtering and 3×3 Gaussian smoothing filtering.

image processing. First of all, we performed a temporal image processing reducing the effects of e.g. laser reflections at the droplet interface, dust on the glass wafer, out-of-plane particles and similar effects. For the temporal filtering, each intensity value at every pixel is first averaged over all images. Secondly, the computed mean pixel gray value is subtracted

Table 2.1: Accuracy of the rotational table by varying rotational speeds where V_w is the input value and V_m is the measured value. The uncertainty (error) is the relative error, $|V_w - V_m|/V_w \times 100\%$.

V_w (m/s)	V_m (m/s)	Error (%)
0.20	0.2014	0.70
0.40	0.4028	0.70
0.60	0.6043	0.72
0.80	0.8057	0.71
1.00	1.0074	0.74
1.20	1.2090	0.75
1.40	1.4099	0.71
1.60	1.6121	0.76

at each pixel, i.e.

$$I'_{i,j}(X,Y) = I_{i,j}(X,Y) - \frac{1}{N}\sum_{i=1}^{N} I_{i,j}(X,Y), \tag{2.1}$$

where $I_{i,j}(X,Y)$ is the intensity value at every pixel for the camera j, $j = 1...4$, $I'_{i,j}$, the new intensity value after this temporal filter processing, i, the index of the image, and N is the total number of images. The result is shown in figure 2.7(b). The aforementioned step is useful in the case of steady flow. Additionally, a spatial filtering is applied, to remove the remaining noise in the images. A spatial 3×3 pixel sliding minimum filter, which subtracts the calculated local minimum from the local intensity has been applied to all individual images. If necessary, the temporal and spatial filtering should be repeated until reasonable particle image fields are obtained. To enhance the visibility of the particle images with respect to the noisy image background a 3×3 Gaussian smoothing filter is applied as a final step (Guezennec and Kiritsis, 1990).

2.3.2 3D calibration and correction

For the 3D calibration, a calibration target is traversed across several planes along the height of the measurement volume (i.e. the droplet). To reproduce the actual experimental conditions, the liquid should be present between the calibration target and the substrate. From this calibration the geometric mapping function is obtained as a third-order polynomial (Soloff et al., 1997), which can be written as:

$$\begin{aligned} x = a_0 + a_1 X + a_2 X^2 + a_3 X^3 + a_4 Y + a_5 Y^2 \\ + a_6 Y^3 + a_7 XY + a_8 X^2 Y + a_9 XY^2, \end{aligned} \tag{2.2}$$

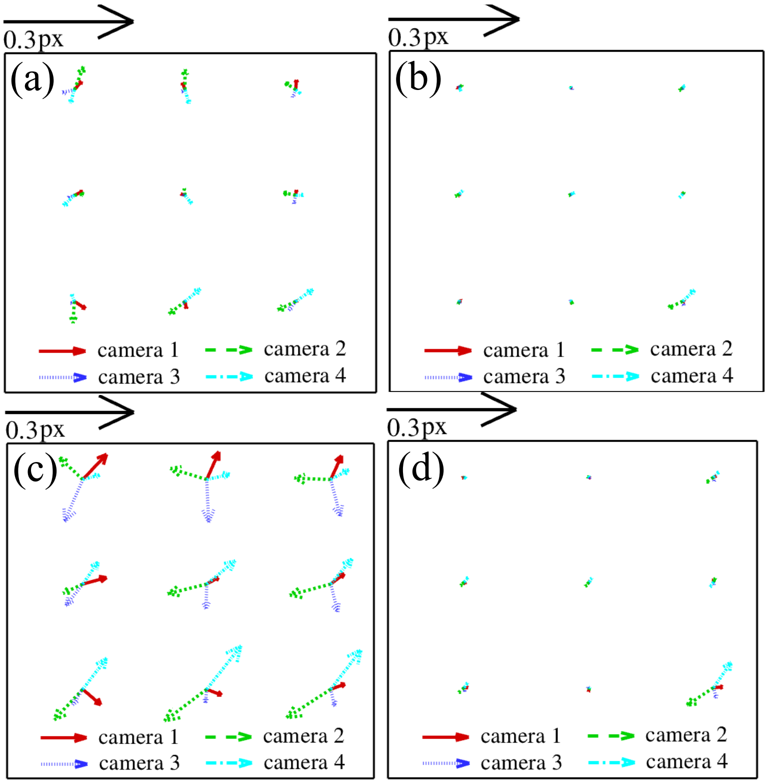

Figure 2.8: Mapping errors for all cameras in a plane located at a vertical position $z \approx 0.1$ mm volume self calibration of before (a) and after (b) in the stationary droplet on the stagnant substrate ($V_w = 0.0$ m/s), before (c) and after (d) in the dynamic droplet on the moving substrate ($V_w = 1.0$ m/s).

$$\begin{aligned} y = {} & b_0 + b_1 X + b_2 X^2 + b_3 X^3 + b_4 Y + b_5 Y^2 \\ & + b_6 Y^3 + b_7 XY + b_8 X^2 Y + b_9 XY^2, \end{aligned} \tag{2.3}$$

where the calibration coefficients a_i and b_i depend on the depth position. Note, that despite the image mapping and reconstruction via the calibration process it is often impractical to achieve a perfect overlap of all reconstructed images in multi-camera PIV measurements. Therefore, in addition, to match corresponding particle images in the volume the possible mismatch, or disparity, of the particle positions for each of the four cameras is resolved by applying a volumetric self-calibration. Wieneke (2008) first described a volumetric self calibration that is based on the computation of the 3D positions of matching particles by triangulation. After applying this procedure, the average mapping errors for the case of stationary substrate are reduced from 0.03 to 0.01 pixels (see figure 2.8(a-b)). For the

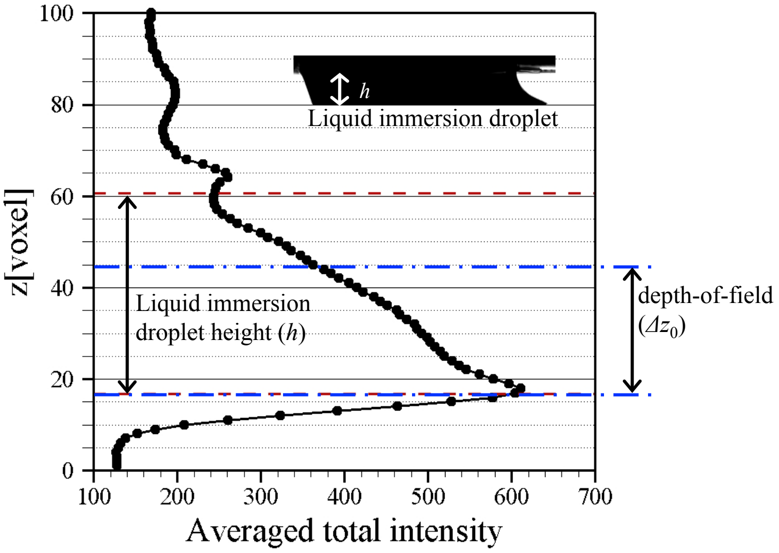

Figure 2.9: Distribution of average intensity peaks in depth. The red dash lines indicate the position of the immersion droplet height, h and the blue dash-dotted lines indicate the depth-of-field of the current setup, Δz_0.

moving substrate, the errors decrease from 0.04 to 0.02 pixels (see figure 2.8(c-d)). In both cases, the disparity errors are less than 0.2 μm. In the case of the immersion droplet on the moving substrate, there is an image disagreement in image results caused by differences in refractive indexes. As a consequence, the disparity errors in both cases are a little bit different.

2.3.3 Tomographic reconstruction

For 3D-3C velocity measurements, the tomographic reconstruction of 3D particles distributions is adopted (Elsinga, 2008). As can be seen in figure 2.4, tracer particles are illuminated by a pulsed light source within a volume and their images are recorded simultaneously from four viewing directions using CCD cameras. Reconstructing the 3D particle distribution by tomography is an inverse procedure using the relation between image planes and the real space as established by a 3D calibration and correction procedure (see Sect. 2.3.2). The 3D intensity distribution is reconstructed in a $2.5 \times 2.1 \times 0.4$ mm^3 volume discretized with $606 \times 510 \times 106$ voxels using the MART (multiplicative algebraic reconstruction technique) algorithm with 5 iterations and with the relaxation parameter $\mu = 1$. The resulting distribution of the average intensity profile in the reconstructed volumes is plotted against the depth-coordinate in figure 2.9. This 3D reconstructed intensity profile provides important information on the position of the droplet with seeding particles as well as the depth-of-field. Moreover, the average reconstructed intensity inside the measurement volume relative to the background intensity outside can be regarded as a measure for the reconstruction accuracy.

To increase the effective particle image density, the reconstructed 3D intensity volumes are averaged over 25 individual reconstructed volume pairs. This is possible when the flow is steady. This effectively increases the seeding density while keeping relative low amount of ghost particles. The 3D-3C velocity vectors of each data set are obtained by means of 3D particle image pattern cross-correlation. The particle image displacement within a chosen interrogation volume (8 × 8 × 8 voxels) with 50 % overlap is obtained by the 3D cross-correlation of the reconstructed particle distribution at the two exposures. The measured vector field contains 147 × 132 × 15 velocity vectors. The final vector results are averaged over 30 data sets (for the immersion droplet on a moving substrate) and 40 data sets (for the immersion droplet on a stagnant substrate).

The final result occasionally has vectors outside the liquid immersion droplet although actual particles must evidently be inside the droplet. This is due to ghost particles outside the measurement domain (Elsinga et al., 2010). In the case of Tomographic PIV the intensity information from actual and ghost particles both contribute to the cross-correlation. Therefore, further image processing is required to identify the internal flow field of the liquid immersion droplet. To eliminate spurious vectors every vertical plane to a mask is applied by considering the largest intensity gradient that represents the position of the droplet interface using average reconstructed intensity field.

2.4 Results and discussion

2.4.1 Error estimation

To assess the dynamic range, reliability, and accuracy of our measurement system, the mass conservation in every sub-volume is examined in the form of the continuity equation. Given that the fluid flow is approximated as incompressible, an estimate for the continuity equation has a relative error distribution for all voxels that can be expressed as (Adrian and Westerweel, 2010)

$$\overline{\left(\frac{\partial u}{\partial x}+\frac{\partial v}{\partial y}+\frac{\partial w}{\partial z}\right)^2} \cong \left(\frac{\sigma_{\Delta x}}{D_I \Delta t}\right)^2, \tag{2.4}$$

where $\sigma_{\Delta x}$ [pixel] is the overall error amplitude for the displacement; D_I the dimension of the square and non-overlapping interrogation domain [pixel] in the cross-correlation procedure; and Δt the time delay between two frames ($\Delta t = 10\ \mu$s). The relative measurement error in every sub-volume is considered. Figure 2.10 presents the histogram of the relative error in the form of the continuity equation. The width of the distribution in figure 2.10

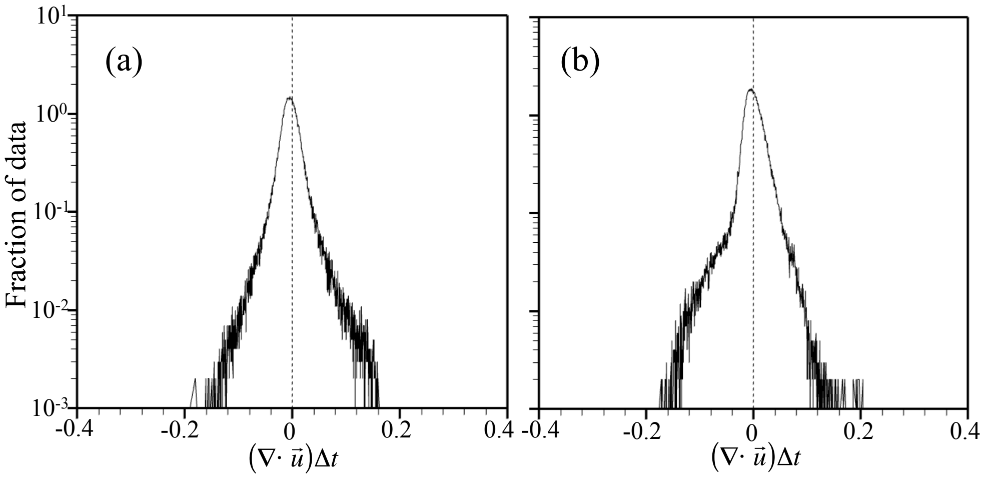

Figure 2.10: The histogram of the relative error of the liquid immersion droplet on (a) the stagnant substrate and (b) moving substrate. The data distribution is fitted by a Gaussian curve to determine the relative error in the form of the continuity equation where $\vec{u}$ has three velocity components, $\vec{u}$=(u,v,w). The standard deviation evaluated from the fit is (a) 0.0246 [pixel/pixel] and (b) 0.0251 [pixel/pixel], respectively.

indicates the error of the measurement; the fitted Gaussian distribution has a standard deviation of (a) 0.0246 [pixel/pixel] and (b) 0.0251 [pixel/pixel], respectively. Hence, given that $D_I = 8$ pixel, it is found through (3.1) that $\sigma_{\Delta x}$= 0.2 pixel. This error is consistent with, a typical the measurement uncertainty reported for tomographic PIV (Elsinga, 2008).

Furthermore, we check the mass conservation at $z = 100$ μm of the immersion droplet on the stagnant substrate. Due to the characteristics of flow field, the mass flow rate must be zero at that plane. The mass flow rate for the inlet and outlet is 0.5 g/min. The relative error for the mass conservation at the middle plane of the stationary droplet is found to be about 2 % with respect to the inlet flow, which is 39.34 g/min.

2.4.2 3D Flow field

Two exemplary cases are examined: a drop on the stationary substrate and a drop on the moving substrate. Note that all figures in this section depict the fluid field in absolute velocity in the stationary frame of coordinates of the immersion needle. Very close to the substrate this yields velocities identical to the local velocity of the wafer.

In the case of the stationary substrate, the internal flow field is largely defined as shown in the inset of figure 2.4. The inflow is driven by pressure at the center and the outflow

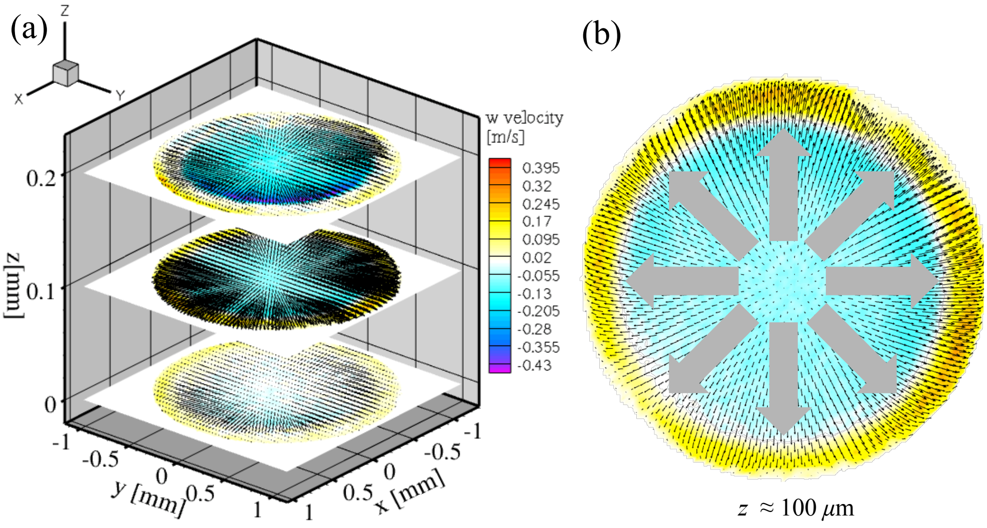

Figure 2.11: Full 3D-3C velocity distribution in the stationary droplet, $V_w = 0$ m/s with injection and extraction of fluids through the immersion needle; (a) Full 3D-3C scan of the flow field where the depth of the individual scanned plane is about 100 μm and (b) the flow field at the middle of the droplet, (at $z \approx 100\ \mu$m). The vectors show the in-plane (x, y) velocity components and the contour represents the out-of-plane velocity component.

is extracted out by the vacuum pressure. This global flow pattern is indeed reflected in figure 2.11 showing the full 3D-3C velocity vector results in the stationary droplet. The selected planes are separated by 100 μm. We show the in-plane (x, y) vectors and the contours for the out-of-plane velocity. The flow pattern has a radial symmetry, although the velocity distribution is not perfectly axi-symmetric. This is because the outlet is connected only to one side of the immersion needle, and hence the flow field is slightly skewed to that side. Alternatively, a non-parallel alignment of the immersion needle and substrate could also be a reason for the asymmetry.

As can be seen in figure 2.12, in the case of a moving substrate, the wafer spins with a velocity of $V_w = 1.0$ m/s at the position of the droplet. We used shadowgraphy to determine the projected external drop shape. For observing the lateral droplet shape, another CCD camera is installed on top of the x-y translation stage with micron resolution. The droplet has an advancing contact angle of about 145° and a receding contact angle of about 30°. The contact angle is measured from the image of the shadowgraph. At the rear of the droplet the shape has an opening half-angle of about 60°. The superimposed vectors in figure 2.12 represent the 3D-3C velocity measured by tomographic PIV. The vector planes are cross-sectional results. The internal flow of the immersion droplet is shown, which

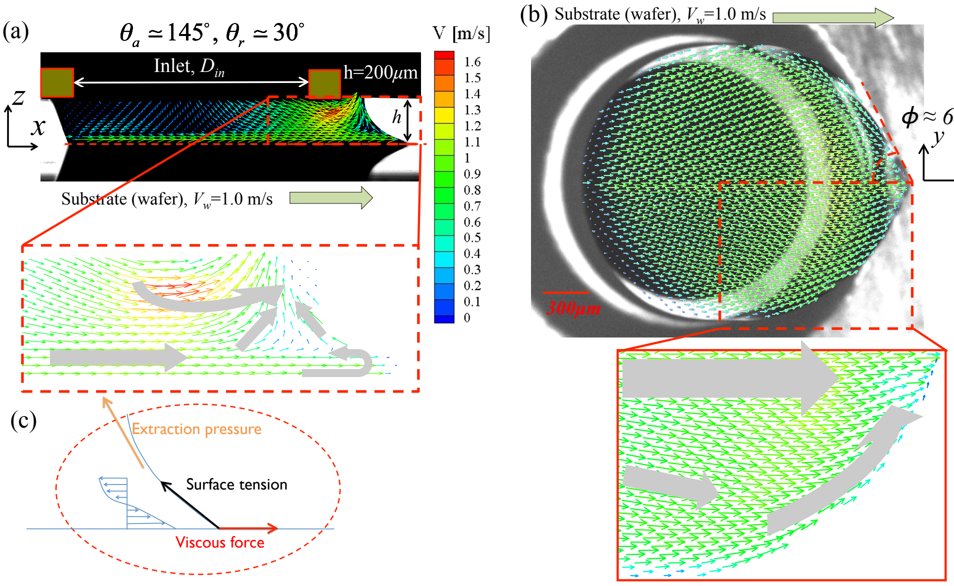

Figure 2.12: 3D-3C vector field and shadowgraphy of the immersion droplet for $\mathrm{Re} = 200$; (a) side view at the cross-sectional plane ($y = 0$) where θ_a is the advancing contact angle and θ_r is the receding contact angle, (b) bottom view at $z \approx 10\ \mu$m and ϕ is the half corner angle, and (c) illustration of the force balance near the corner of the droplet. Here, the vector colors are the magnitude of the velocity in three dimensions.

exhibits a complex, but symmetric, flow pattern. There is a small circulation region near the corner of the droplet (see figure 2.12(a)). This region is related to the force balance of the viscous force, surface tension, and outlet pressure, as shown in figure 2.12(b). The bottom result shown in figure 2.12(b) presents the flow field above the substrate ($z \approx 10$ μm). A detailed inspection of the flow near the moving contact line indicates that particles follow the contact line. The velocity gradient of the flow field is related to the substrate speed, surface tension and outlet pressure. Furthermore, there is a fast flow region near the rear outlet trench where the fluid is extracted from the droplet. Therefore, the rear trench of the immersion needle should be considered as an important parameter to extract fluid.

This experiment involves non-uniform optical properties of the media, e.g. different indices of refraction for air, substrate, and water. In figure 2.12, only few data could be obtained near the top of the advancing part of the droplet as a result of the rather large advancing contact angle, which limits the view in that part of the droplet.

The full 3D-3C flow field shown in figure 2.13 reveals the velocity distribution and streamlines inside the liquid immersion droplet on the moving substrate at $\mathrm{Re} = 200$. The vectors

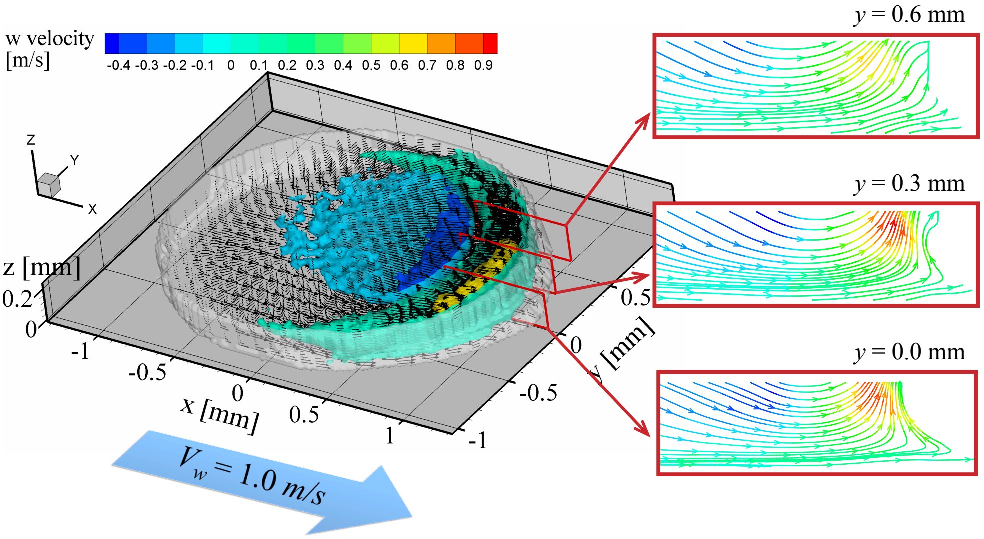

Figure 2.13: Full 3D-3C velocity distribution and iso-contour plot in the liquid immersion droplet on the moving substrate ($V_w = 1.0$ m/s) at Re = 200, where the vectors show 3D-3C velocity components and the iso-contour represents the out-of-plane velocity component. The red boxes show the streamline results at the cross sectional planes ($y = 0.0, 0.3, 0.6$ mm) where the streamline colors indicate the magnitude of w velocity. The white surface contour indicates the external shape of the liquid immersion droplet on the moving substrate.

indicate 3D-3C components of the velocity and the iso-contours represent the out-of-plane velocity component. Furthermore, the external shape (i.e. free surface) of the liquid immersion droplet is indicated in white, i.e. where the velocity magnitude is zero. Directly above the substrate, the flow direction is the same as the direction of the substrate motion, due to the viscous drag, as shown in figure 2.14(a). At $z \approx 30$ μm, the flow field of the front part of the droplet begins to flow towards the trench of the immersion needle, as shown in figure 2.14(b). On the other hand, in figure 2.14(c-e), the main flow is converging to the rear of the droplet, and there is a small flow region with reversed flow at the corner of the droplet. The small reversed flow region becomes smaller as the plane increases its position in the z-direction, as shown in figure 2.14(c-d). Figure 2.14(e) shows the fast flow region that is nearby the rear trench of the immersion needle, where there still is a small reversed flow region. Schuetter et al. (2006) and Riepen et al. (2008) showed that the droplet tail becomes longer as long as the substrate speed increases. The size of the reversed flow region near the corner of the droplet is related to the length of the droplet tail. The droplet will break up when the viscous force, surface tension and outlet pressure are no longer balanced. Consider figure 2.2(b-c), when the viscous drag force is further increased, i.e. the

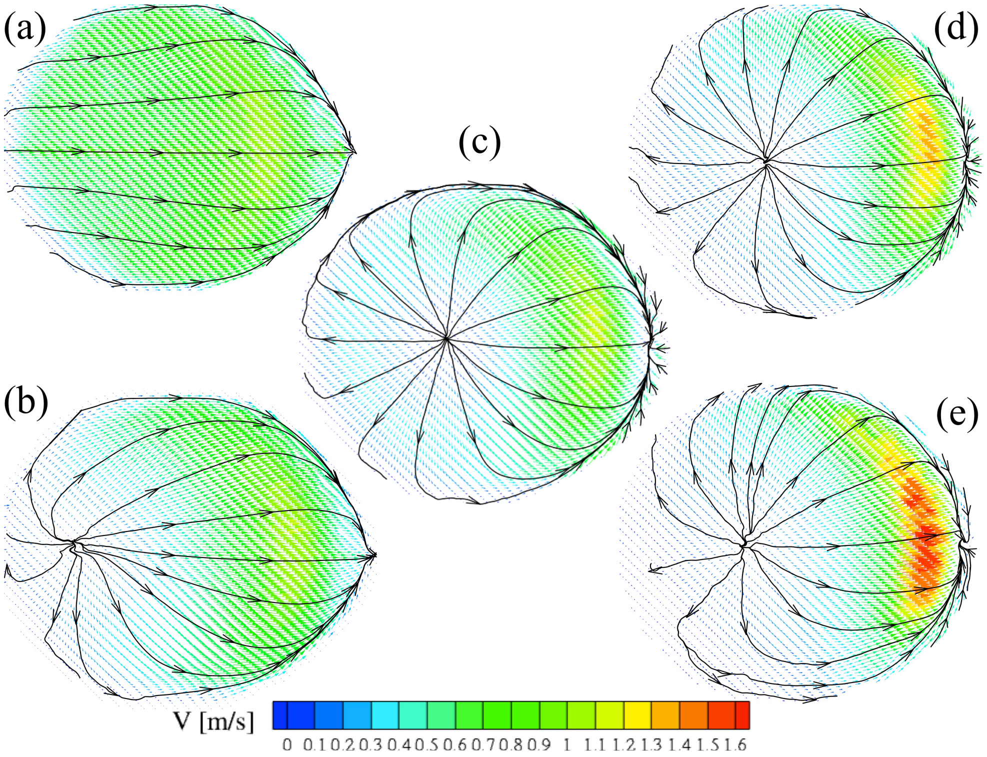

Figure 2.14: Full 3D-3C velocity distributions (colors) and streamlines (black) in the liquid immersion droplet ($V_w = 1.0$ m/s) at $\mathrm{Re} = 200$; Shown are five scan-planes at (a) $z \approx 0$ μm (b) $z \approx 30$ μm, (c) $z \approx 60$ μm, (d) $z \approx 120$ μm, and (e) $z \approx 180$ μm; vector colors represent the magnitude of the velocity in the three dimensions.

wafer speed approaches the critical velocity ($V_w = 1.4$ m/s), the liquid immersion droplet begins to show 'pearling'.

In this experimental case, the immersion droplet breaks up, when the critical dimensionless numbers are the capillary number of 0.02 and Reynolds number of 280. From the point of view of hydrodynamics, the Reynolds number is a general dimensionless number to characterize the flow field. However, according to Podgorski et al. (2001) and Riepen et al. (2008), the instability result is similar even though the Reynolds number is different. In this case, the capillary number is more important parameter to determine the droplet break-up. The capillary number represents the relative effect of viscous forces versus surface tension. By Laplace's theorem, the surface tension is expressed as

$$\Delta p = \gamma \kappa = \gamma \left(\frac{1}{R_1} + \frac{1}{R_2} \right), \tag{2.5}$$

where Δp is hydrostatic pressure, γ is the surface tension, κ is the mean curvature of the surface, and R_1 and R_2 are the principal radii of the curvature. The hydrostatic pressure is the pressure difference between the inside and outside surfaces. According to (5), by varying Δp we can change the curvature of the surface. Riepen et al. (2008) showed this by changing the ambient pressure distribution, and they increased the critical speed of the wafer in the immersion lithography system. In this experimental setup, the dynamic surface tension can be determined from the extraction force. Intuitively, as long as the extraction pressure is increased, the tail of the droplet is decreased. Therefore, in the immersion lithography system the capillary number would be properly defined by considering the pressure as the additional parameter.

2.5 Conclusion

For the first time the complex internal flow of a liquid immersion droplet on a moving substrate has been investigated by using tomographic PIV. The technique allows to obtain the full 3D-3C velocity vector fields. Current results help to understand the internal flow field of the liquid immersion droplet at relatively high Reynolds number, ($Re \gg 1$). The location of the measurement data is consistent with the shape of the droplet determined by means of shadowgraphy. The limited view on certain parts of the droplet can be improved, provided that the advancing contact angle is decreased. In addition, reducing the strong reflection light at the droplet interface improves the quality of the data near the free surface. The consistency of the measured data is quantified by means of the continuity equation for an incompressible fluid. We observe the separation flow region near the tail of the droplet. This is related to the droplet instability resulting in the rupture of the droplet tail. However, further investigation will be necessary to study these issues in detail. Future work will address a parameter study related to the flow instability as a function of the height of the droplet, different inlet and outlet conditions, different surface condition of the wafer (i.e. applied coatings), and the velocity of the substrate (wafer).

2.6 Acknowledgemet

We would like to thank R. Lindken for valuable advice and discussions on the PIV measurements at an early stage of the project. We also thank M. Franken for his contribution to the experimental setup. Additionally, we acknowledge a very useful conversation with B. Wieneke from LaVision GmbH on 3D PTV and a good support of experimental setups of F. Evangelista and M. Verdonck from ASML Holding NV.

2.7 Bibliography

R. J. Adrian and J. Westerweel. *Particle Image Velocimetry*. Cambridge University Press., 2010.

C. Brücker. Digital-Particle-Image-Velocimetry (DPIV) in a scanning light-sheet: 3D starting flow around a short cylinder. *EXP FLUIDS*, **19**, 255, 1995.

G. E. Elsinga. *Tomographic particle image velocimetry and its application to turbulent boundary layers*. Ph.D. thesis, Delft University of Technology, 2008.

G. E. Elsinga et al. Tomographic particle image velocimetry. *EXP FLUIDS*, **41**, 933, 2006.

G. E. Elsinga et al. On the velocity of ghost particles and the bias errors in Tomographic-PIV. *EXP FLUIDS*, 1–14, 2010.

R. H. French and H. V. Tran. Immersion lithography: photomask and wafer-level materials. *ANN REV MATER RES*, **39**, 93, 2009.

Y. G. Guezennec and N. Kiritsis. Statistical investigation of errors in particle image velocimetry. *EXP FLUIDS*, **10**, 138, 1990.

K. D. Hinsch. Holographic particle image velocimetry. *MEAS SCI TECHNOL*, **13**, R61, 2002.

K. H. Kang et al. Quantitative visualization of flow inside an evaporating droplet using the ray tracing method. *MEAS SCI TECHNOL*, **15**, 1104, 2004.

L. Limat and H. A. Stone. Three-dimensional lubrication model of a contact line corner singularity. *EUROPHYS LETT*, **65**, 365, 2004.

H. W. Lu et al. A study of EWOD-driven droplets by PIV investigation. *LAB CHIP*, **8**, 456, 2008.

H. G. Maas, A. Gruen and D. Papantoniou. Particle tracking velocimetry in three-dimensional flows. *EXP FLUIDS*, **15**, 133, 1993.

J. Mulkens et al. Benefits and limitations of immersion lithography. *J MICROLITH MICROFAB*, **3**, 104, 2004.

S. Owa and H. Nagasaka. Immersion lithography: its history, current status and future prospects. In *P SPIE*, volume 7140, 714015, 2008.

F. Pereira et al. Defocusing digital particle image velocimetry: a 3-component 3-dimensional DPIV measurement technique. Application to bubbly flows. *EXP FLUIDS*, **29**, 78, 2000.

F. Pereira et al. Microscale 3D flow mapping with μDDPIV. *EXP FLUIDS*, **42**, 589, 2007.

T. Podgorski, J. M. Flesselles and L. Limat. Corners, cusps, and pearls in running drops. *PHYS REV LETT*, **87**, 36102, 2001.

M. Riepen, F. Evangelista and S. Donders. Contact line dynamics in immersion lithography-dynamic contact angle analysis. In *Proc. 1st Euro. Conf. Microfluidics*, 2008.

S. Schuetter et al. Measurements of the dynamic contact angle for conditions relevant to immersion lithography. *J MICROLITH MICROFAB*, **5**, 023002, 2006.

J. Sheng, E. Malkiel and J. Katz. Buffer layer structures associated with extreme wall stress events in a smooth wall turbulent boundary layer. *J FLUID MECH*, **633**, 17, 2009.

J. H. Snoeijer et al. Self-similar flow and contact line geometry at the rear of cornered drops. *PHYS FLUIDS*, **17**, 072101, 2005.

S. M. Soloff, R. J. Adrian and Z. C. Liu. Distortion compensation for generalized stereoscopic particle image velocimetry. *MEAS SCI TECHNOL*, **8**, 1441, 1997.

B. Wieneke. Volume self-calibration for 3D particle image velocimetry. *EXP FLUIDS*, **45**, 549, 2008.

CHAPTER 3

EXPERIMENT II: COMPARISON OF TOMO-PIV AND 3D-PTV FOR MICROFLUIDIC FLOWS[1]

Abstract

Two 3D-3C velocimetry techniques for micro-scale measurements are compared: tomographic particle image velocimetry (Tomo-PIV) and 3D particle tracking velocimetry (3D-PTV). Both methods are applied to experimental data from a confined shear-driven liquid droplet over a moving surface. The droplet has 200 μm height and 2 mm diameter. Micro 3D-PTV and Tomo-PIV are used to obtain the tracer particle distribution and the flow velocity field for same set of images. It is shown that the reconstructed particle distributions are distinctly different, where Tomo-PIV returns a nearly uniform distribution over the height of the volume, as expected, PTV reveals a clear peak in the particle distribution near the plane of focus. In Tomo-PIV, however, the reconstructed particle peak intensity decreases in proportional to the distance from the plane of focus. Due to the differences in particle distributions, the measured flow velocities are also different. In particular, we observe Tomo-PIV to be in closer agreement with mass conservation. Furthermore, the random noise level is found to increase with distance to the plane of focus at a higher rate for 3D-PTV as compared to Tomo-PIV. Thus for a given noise threshold value the latter method can measure reliably over a thicker volume.

---

[1] The content of this chapter has been accepted for publication in Measurement Science and Technology (Kim et al. 2012).

3.1 Introduction

Fully three-dimensional velocimetry techniques now find increasing use in microfluidics investigations (Wereley and Meinhart (2010); Cierpka and Kähler (2012)). Some recent examples of three-dimensional three-component (referred to as 3D-3C) velocity measurements for micro flows include (a) mixing at the T-junction of micro channels (Balan et al. (2010); Lindken et al. (2006)), (b) an evaporating droplet (Pereira et al. (2007)), (c) a liquid immersion droplet on a moving substrate (Kim et al. (2011)), (d) the behavior of swimming microorganisms (Choi et al. (2011)), and (e) a brownian motion of the particle (Kihm et al.2004; Park et al.2005).

For steady and slowly evolving flows, the classic volumetric scanning approach can be used (e.g. Shinohara et al. (2005); Kinoshita et al. (2007); and Lu et al. (2008)). This technique relies on progressively changing the plane of focus by adjusting the microscope, thus building up a volume from the individual measurement planes. However, the measurement plane is not exactly a plane, but rather includes a region around the plane of focus, which is often substantial and introduces some inaccuracies related to the variation of velocity over the depth direction (Kloosterman et al. (2011)). The uncertainty can be dramatically improved when truly instantaneous 3D velocimetry techniques are used. These techniques first determine the 3D position of each particle within the measurement volume, in contrast to assuming all of them to be located in the plane of focus, and then evaluate their displacement. As a result, the particle displacement vector is positioned at the correct depth, which yields an improvement in the measurement accuracy. The improvement was recently demonstrated by comparing planar micro-PIV with an astigmatism particle tracking method that is fully 3D (Cierpka et al. (2012)). Apart from using astigmatism, the 3D particle distribution and velocity can also be obtained from a single view by means of in-line holography (Sheng et al. (2006); Ooms et al. (2009)). By using deconvolution microscopy, a single-camera micro-PTV introduced to simultaneously measure 3D-3C velocity vectors for three-dimensional micro-scale flow fields (Park et al.2006). Additionally, the confocal laser scanning microscopy is introduced by Park et al. (2004), which enables to precisely scan each horizontal plane in the normal direction.

Three-dimensional techniques based on multiple views and photogrammetry, i.e. 3D-PTV (Maas et al. (1993)) and Tomo-PIV (Elsinga et al. (2006)), are now being introduced to microfluidics as well. In this case, a large microscopic objective with several off-axis viewing ports allows imaging the particles from different directions simultaneously, as required. A main advantage of the techniques appears to be that they are applicable even in some challenging environments for particle imaging, such as in an immersion hood containing air-water interfaces and strong background light reflections (Kim et al. (2011)). Interestingly, early comparisons of micro 3D-PTV (2010) and Tomo-PIV (2011) based on the same recordings have indicated that the latter yields more reliable velocity data. That is, the velocity field is in much closer agreement with mass conservation (see also section 4.1). This was surprising since the particle image density in that experiment was relatively low, i.e. between 0.010 and 0.034 particles per pixel depending on the particle intensity threshold, and the volume thin (only 100 voxels deep). For such conditions the number of spurious particle detections, also known as ghost particles, is expected to be rather low (Maas et al. (1993); Elsinga et al. (2011)). Hence, we anticipated both 3D approaches to be equally valid. This was apparently not the case.

Therefore, the aim of the present paper is to perform a detailed comparison and assessment of both 3D-PTV and Tomo-PIV in a microfluidic application. The purpose is to identify the likely cause of the observed differences. The acquired insights can be useful for the design of future experiments.

The approach is to use the existing recordings of the flow in a confined shear-driven liquid droplet and to evaluate them by both 3D-PTV and Tomo-PIV. The experimental setup and the data processing steps are outlined in sections 2 and 3 respectively. The following properties are assessed: the conservation of mass in the droplet in a control volume analysis (section 4.1), the reconstructed particle distributions (section 4.2), the divergence of the local velocity field (section 4.3), and finally the velocity profiles themselves (section 4.4). The 3D-PIV methods are shown to break down at different distances from the plane of focus. In other words, the depth of the volume over which the velocity can be measured reliably is found to differ. The main conclusions are summarized in section 5.

3.2 Experimental set-up

An illustration of the used experimental setup is given in figure 3.1(a). The experiment used in the present investigation is described in detail by Kim et al. (2011). For completeness we recall here the main characteristics. A confined liquid droplet is generated by a device as shown in the red dashed box of the top right in figure 3.1(b). The device can generate a constant volume droplet that is 200 μm in height and has a 2 mm diameter. At the center of the device, water is supplied to the droplet. Then water and air are simultaneously extracted at the outlet. The substrate moves with a velocity of U=1.0 m/s at the position of the droplet, so that the flow conditions are characterized by a capillary number (Ca $= \mu U/\gamma$) of 0.014 and a Reynolds number (Re $= \rho U h/\mu$) of 200 (when μ is the viscosity, ρ the density, and γ the surface tension of the fluid).

For the measurement of the fluid velocity inside the droplet, the working fluid is seeded with 1.28-μm tracer particles (Microparticle GmbH) that are fluorescent (Rhodamine-B) and that have a polyethylene glycol (PEG) coating. The fluorescence is excited by illumination with a Nd:YLF laser, which emits light at a wavelength of 527 nm. The laser beam covers the whole droplet. For homogenizing the laser light, a diffuser plate is used. The particle image diameter is estimated by $d_\tau = \sqrt{(M_0 d_p)^2 + d_{diff}^2}$, where d_p is the particle diameter; M_0, the magnification of the lens; $f^\#$, the f-number of the lens. The diffraction limited minimum image diameter is $d_{diff} = 2.44[M_0+1]f^\#\lambda$ where λ is the

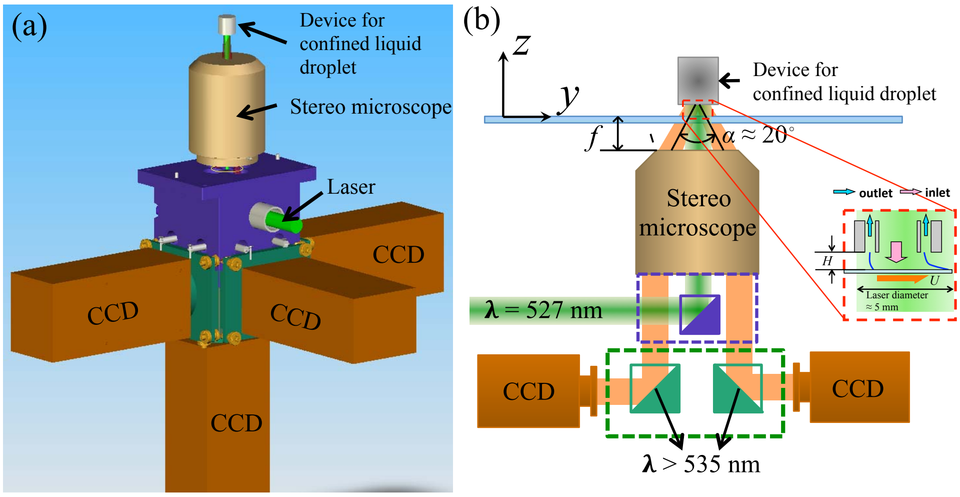
(a)
Device for confined liquid droplet
Stereo microscope
Laser
CCD
CCD
CCD
CCD
(b)
z
y
Device for confined liquid droplet
f
α ≈ 20°
Stereo microscope
outlet
inlet
H
U
Laser diameter ≈ 5 mm
λ = 527 nm
CCD
CCD
λ > 535 nm

Figure 3.1: Schematic of the experimental setup. (a) Four PIV cameras are mounted on a custom-made microscope, drawn by Sjoerd Donders (ASML). (b) The cross-sectional schematic of Figure 3.1(a). In the red-dashed box, the confined liquid droplet is described.

wavelength of the light. The estimated particle image diameter is approximately 2∼3 pixels, which is in good agreement with observations in the recorded raw images of particles in the plane of focus. The plane of focus coincides with the surface of the substrate. The present image density (N_I) is 5.38×10^{-1}, given by $N_I \equiv CA_I\Delta z_0/M_0^2$, where C is the mean number of particles per unit volume [m^{-3}], Δz_0, the depth-of-field [m], and A_I, the image interrogation area [m^2]. The depth-of-field is given approximately by $\Delta z_0 \cong 4(1+1/M_0)^2 f^{\#2}\lambda$. For the given optical parameters we have $\Delta z_0 \approx 120$ µm. In the present condition, the image density is low, $N_I < 1$. Directly counting particle images from the raw images yields a value of around 0.034 ppp (particles per pixel), which corresponds to a source density $N_S \simeq 0.09$ (Adrian and Westerweel (2010))

The four CCD cameras have a resolution of 1376 × 1040 pixels each and a 12-bit dynamic range. The optical path of each camera is off-axis through a single microscope objective lens with a magnification of 1.5. The offset angle between the optical axes of the cameras is about $\alpha \approx 20^\circ$ (see figure 3.1(b)). Due to the small viewing angle between cameras, particles appear elongated in the depth direction, as shown in figure 3.2, increasing the position uncertainty in that direction. If the diameter of a particle image is 2 pixels, then its length

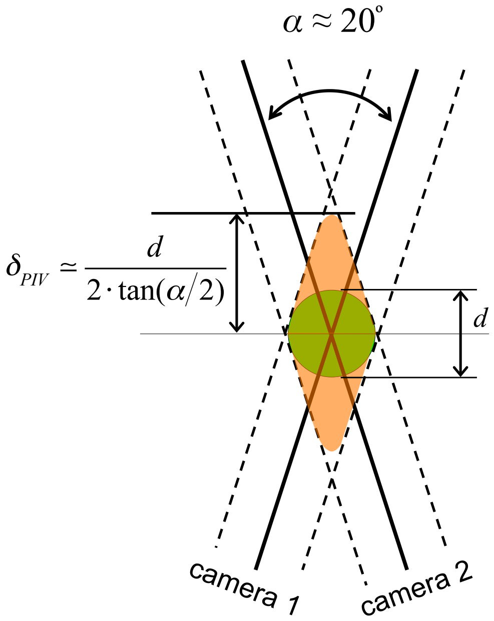
$\alpha \approx 20^{\circ}$
$\delta_{PIV} \approx \frac{d}{2 \cdot \tan(\alpha/2)}$
d
camera 1
camera 2

Figure 3.2: Measurement uncertainty in the present PIV system due to the small viewing angle (α) of multi-cameras where d is the particle image diameter, which is a measure for the in-plane uncertainty in 3D particle triangulation, and δ_{PIV} is the corresponding uncertainty in depth direction.

in the depth direction will be 12 pixels.

3.3 Methods

In this section, we describe the data processing for Tomo-PIV and 3D-PTV. As mentioned, we use the same images for both methods. To reliably detect the particles a proper preprocessing is essential. Here, we used a sliding minimum to subtract background illumination and a 3×3 Gaussian smoothing to reduce image noise of the particle images. For the calibration, we perform a 3D calibration with volume self calibration (2008), which reduces the calibration errors to 0.02 pixels corresponding to about 0.1 µm. The whole pre- and post-processing and calibration procedure are performed by means of a commercial code (Davis 7.4, LaVision GmbH). The subsequent particle displacement calculation is obviously different for 3D-PTV and Tomo-PIV (see figure 3.3), the details of which will be outlined below.

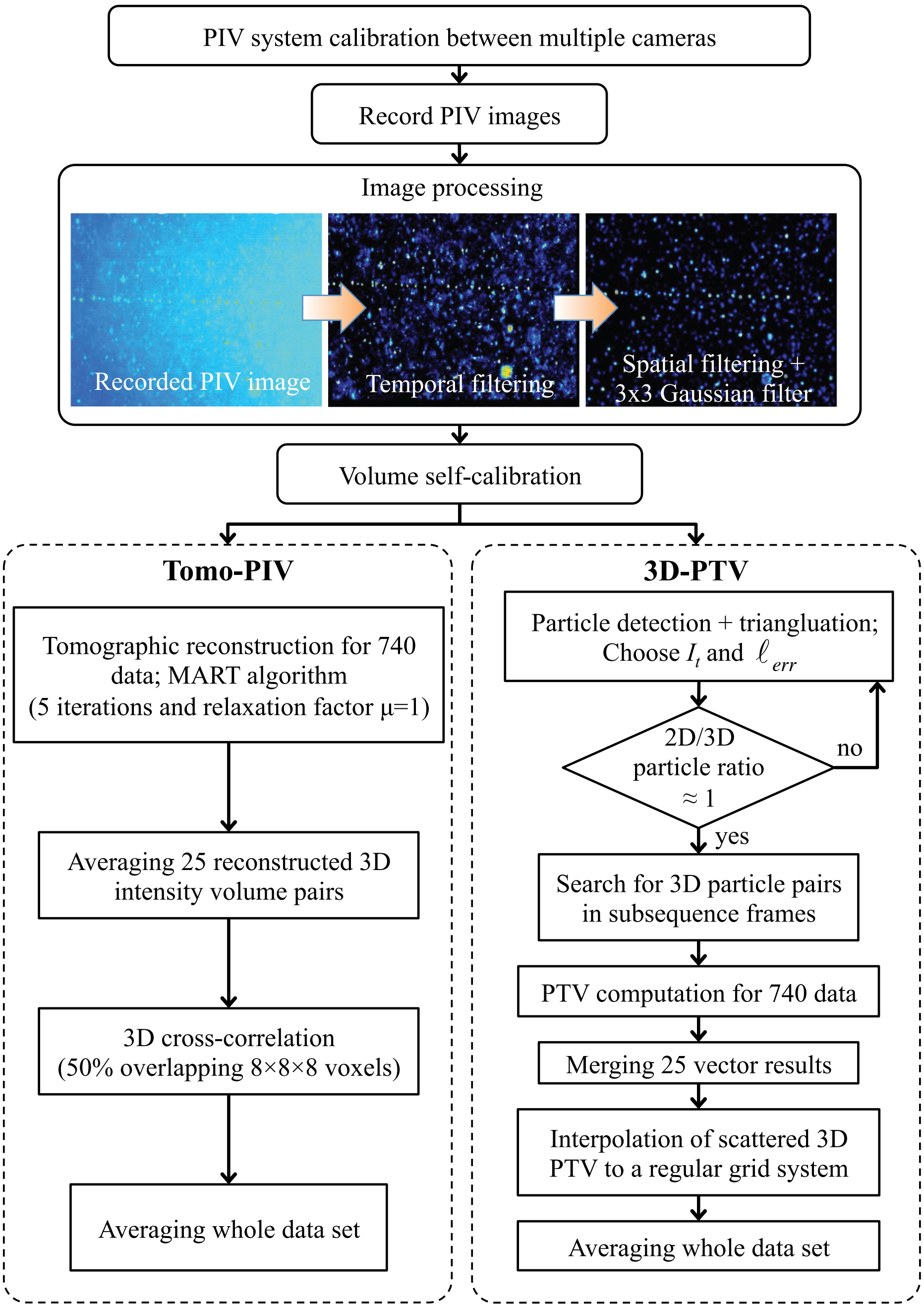
PIV system calibration between multiple cameras
Record PIV images
Image processing
Recorded PIV image
Temporal filtering
Spatial filtering +
3x3 Gaussian filter
Volume self-calibration
Tomo-PIV
Tomographic reconstruction for 740 data; MART algorithm (5 iterations and relaxation factor μ=1)
Averaging 25 reconstructed 3D intensity volume pairs
3D cross-correlation (50% overlapping 8×8×8 voxels)
Averaging whole data set
3D-PTV
Particle detection + triangulation; Choose I_t and ℓ_{err}
2D/3D particle ratio ≈ 1
no
yes
Search for 3D particle pairs in subsequence frames
PTV computation for 740 data
Merging 25 vector results
Interpolation of scattered 3D PTV to a regular grid system
Averaging whole data set

Figure 3.3: Flow chart of full 3D-3C velocity measurement techniques; Tomo-PIV (left) and 3D-PTV (right)

3.3.1 3D Particle Tracking Velocimetry

In this section, we describe the 3D-PTV processing steps (see the right part of figure 3.3). It essentially consists of two main steps; (1) the detection of particles in the pre-processed images and their triangulation into 3D space and (2) the identification of corresponding particles in the subsequent volumes (the actual particle tracking). The detection of the particle images relies on a peak intensity threshold value (I_t) (1993), for which we considered 1 or 10 counts and the allowable triangulation error ℓ_{err}, which is put at 1.9 and 2.3 pixels for the case of $I_t = 1$ and 10, respectively. Note that these intensity threshold values are significant compared to the maximum intensity in the pre-processed images, which is around 20 counts. The ℓ_{err} is similar to the particle image diameter and is chosen such that number of particles in the images ('2D particles') is about equal to the number of particles triangulated in the volume (referred to as '3D particles'). Then the resulting image seeding density (ppp) is 0.0148 (I_t = 10 counts) and 0.034 (I_t = 1 count). We use a two-frame particle tracking algorithm, taking into account a given allowed displacement range and the spatial coherence of neighboring groups of vectors (1996). The prescribed displacement range corresponds to a velocity magnitude $\mid \vec{U}(u,v,w) \mid \leq 2.0$ m/s. By accounting for a spatial coherence of neighboring vectors a preferred flow direction can be identified in which the most likely particle position is expected. Note that this option requires the mean distance between neighboring vectors to be small compared to the typical dimensions of the flow structures, otherwise spatial coherence would not necessarily exist. In this experimental condition, the typical particle displacement between subsequent frames is about 4 pixels. The prescribed spatial coherence field size is 10 pixels and the number of clustering particles is at least 1.

Agüí and Jiménez (1987) first introduced the interpolation of PTV data onto a regular grid by using a simple convolution with an adaptive Gaussian window. Here, we follow a similar process. However, before converting the particle displacement field onto a regular grid system, 25 individual vector fields are merged into one. This effectively increases the density of velocity vectors in the volume by a factor 25 while keeping a relative low amount of ghost particles. For the conversion process, the weighting factor takes into account the proximity to a center of a grid cell. Hence, if a vector is near a grid point it has a higher influence effect than a most distant vector, which yields this expression using a Gaussian weighting factor α_j,

$$\alpha_j = \exp\left(-2 \times \left\|c_i - v_j\right\|^2\right), \qquad j = 1, \cdots, N_j, \tag{3.1}$$

where c_i is a center position of a cell and v_j is a vector position Vectors at the cell center are weighted by unity. All weighted vectors are then summed yielding the interpolation vector value at all i,

$$\vec{U}_i' = \frac{\sum_{j=1}^{N_j} \alpha_j \cdot \vec{U}_j}{\sum_{j=1}^{N_j} \alpha_j}, \tag{3.2}$$

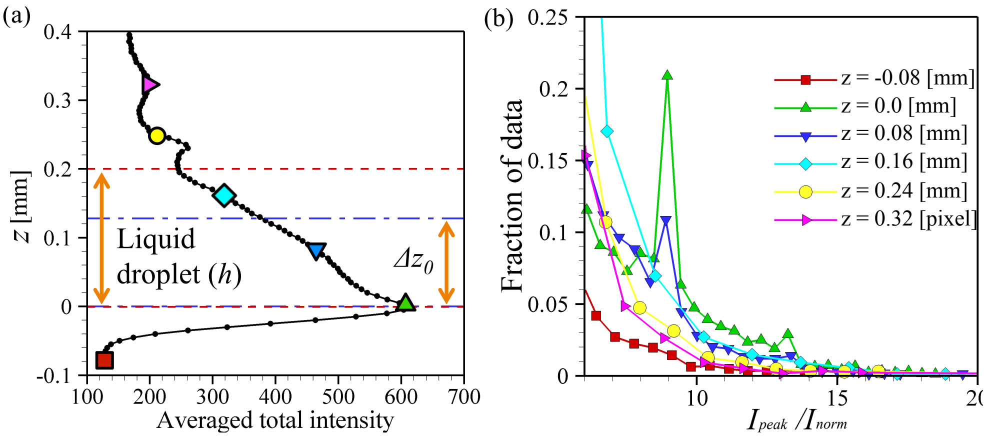

Figure 3.4: Tomographic reconstruction intensity profiles. (a) Distribution of average peak intensity in depth. The red-dashed lines indicate the position of the liquid droplet height, h, and the blue dash-dotted lines indicate the depth-of-field of the current setup, Δz_0. (b) PDF of the peak intensity for different z positions where the peak intensity is normalized by $I_{norm} = 600$. The different colors of figure 3.4(b) indicate the different z locations of figure 3.4(a).

where N_j is the total number of surrounding vectors in the 3×3×3 grid cells. In addition, if there is no vector close to the cell center, no resulting vector is assigned. In the end, choosing the proper grid size is important because of the given mean particle image density. In the present case, the selected grid spacing is $G = 4$ or 8 pixels. Then the final vector results on the grid are again averaged over 30 data sets. The whole data processing are performed by means of a commercial code (Davis 7.4, LaVision GmbH).

3.3.2 Tomographic Particle Image Velocimetry

We perform the tomographic reconstruction of 3D particles distributions starting from the same pre-processed images. The overall procedure of Tomo-PIV is described in figure 3.3. The reconstructed 3D intensity distribution volume covers $2.5 \times 2.1 \times 0.4$ mm^3, which is discretized with $606 \times 510 \times 106$ voxels. Reconstruction is performed using the MART (Multiplicative Algebraic Reconstruction Technique) algorithm with 5 iterations and with the relaxation factor $\mu = 1$. Figure 3.4(a) shows the resulting distribution of the averaged reconstructed intensity along the droplet height. From this reconstructed 3D intensity profile, we recognize the position of the plane of focus at the wall. Further, it is seen that the averaged intensity magnitude decreases with the distance to the wall, i.e. the plane of focus. In the present experimental condition, the whole measurement object is volumetrically illuminated and all particles in the volume are expected to scatter equal amounts of light. Hence, the decrease in reconstructed intensity must be explained by the particles moving out-of-focus with increasing wall normal distance, which decreases their peak image intensity and broadens their image diameter. Consistent with the previous, figure 3.4(b) shows that the PDF of the particle peak intensities becomes lower with increasing the depth coordinate. Nevertheless, the resulting distribution of the intensity profile depicts that the reconstructed particle signal inside the measurement volume ($0 \leq z \leq 0.2$ mm) exceeds the background intensity (see figure 3.4(a)), or reconstruction noise level, which is determined inside the glass wall (at $z =$ -0.08 mm) where no actual particles can be physically present.

The present seeding density is relatively low as to resolve the small-scale detail of the fluid motion. In order to increase the effective particle density, the reconstructed 3D intensity volumes are averaged over 25 individual reconstructed volume pairs. This effectively increases the seeding concentration while keeping a relatively low amount of ghost particles. The information density in the reconstructed particle volume is thus increased, similar to the increase in the vector density used before for the 3D-PTV. This is applicable when the fluid motion is steady. To obtain the 3D-3C velocity vectors, the volumetric cross-correlation on the resulting 3D intensity distribution is applied. The 3D cross-correlation is performed with a chosen interrogation volume 8 × 8 × 8 voxels at 50 % overlap. The measured vector field for the liquid droplet contains 147 × 132 × 15 velocity vectors. The final vector results are again averaged over 30 data sets.

In principle, actual particles should evidently be inside the liquid droplet. However, during the tomographic reconstruction, spurious particles outside the measurement domain can be detected, which are referred to as ghost particles. In Tomo-PIV, the reconstructed intensity information of actual and ghost particles both contribute to the cross-correlation (2011). The final result can have spurious vectors outside the relatively moving liquid droplet, as shown in figure 3.5(a), due to ghost particles. Hence, further image processing is essential to identify the real flow field inside the liquid droplet. The spurious vectors outside the droplet are eliminated by using a binarized volumetric mask (figure 3.5(b)). Figure 3.5(c)-(e) show how the droplet location can be detected in the average reconstructed intensity distribution. Every x-y plane is binarized by considering that the largest intensity gradient indicates the position of the liquid-gas droplet interface. Then, combining the masks from all x-y planes, we can reconstruct the droplet shape as shown in figure 3.5(b). This volumetric mask procedure is only available from the tomographic reconstruction result. Finally, the vector result after applying the mask is presented in figure 3.5(f).

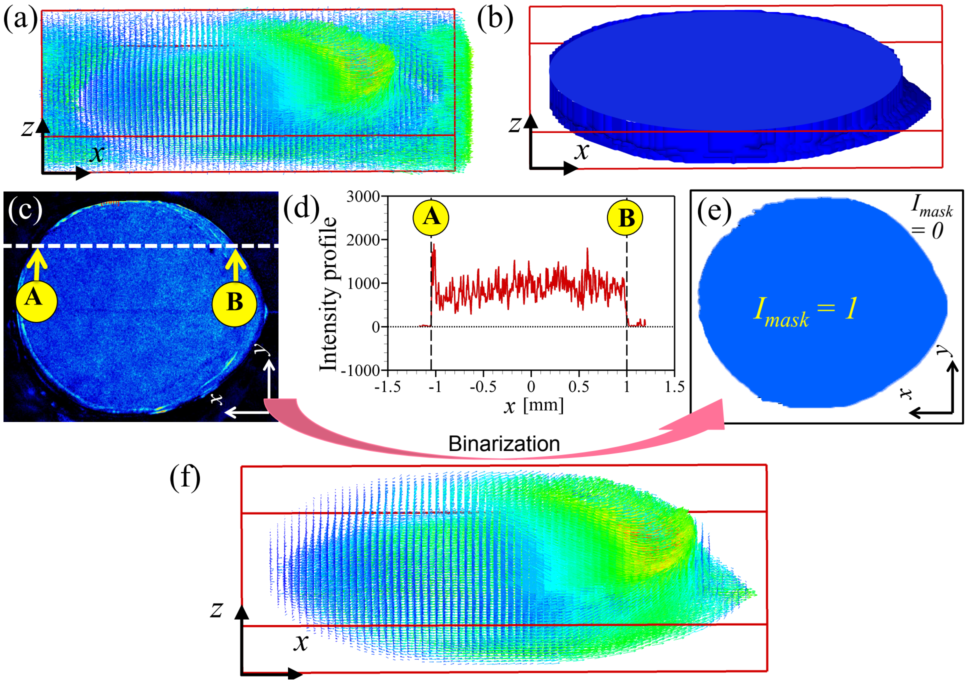

Figure 3.5: Volumetric mask function procedure. (a) the raw Tomo-PIV vector result, (b) the volumetric mask that is obtained by the collecting binarized intensity maps where the blue color indicates the value ‘1’ and otherwise ‘0’, (c) an averaged intensity map at a certain z-plane, (d) an intensity profile along the white-dashed line, (e) a binarized intensity map is obtained by recognizing the droplet interface A and B ($I_{mask} = 1$ for inside the droplet and 0 for outside the droplet), and (f) the final vector result is obtained by multiplying (a) by (b). The vector color indicates the magnitude of the velocity.

3.4 Results and discussion

3.4.1 Result comparison of 3D-PTV and Tomo-PIV

The three-dimensional flow fields obtained by 3D-PTV and Tomo-PIV are not in full agreement. In the case of 3D-PTV, the flow field close to the rear part of the droplet is weak, i.e. of lower velocity magnitude, as shown in figure 3.6(a). It is expected that the outflow should show higher velocity flow than the measurement result by 3D-PTV, because the fluid is mainly extracted over a small region at the rear part of the droplet. In addition, the flow field close to the substrate must be uniform and equal to the substrate velocity. At this position, 3D-PTV could not obtain the uniform flow as shown in figure 3.6(b). On the other

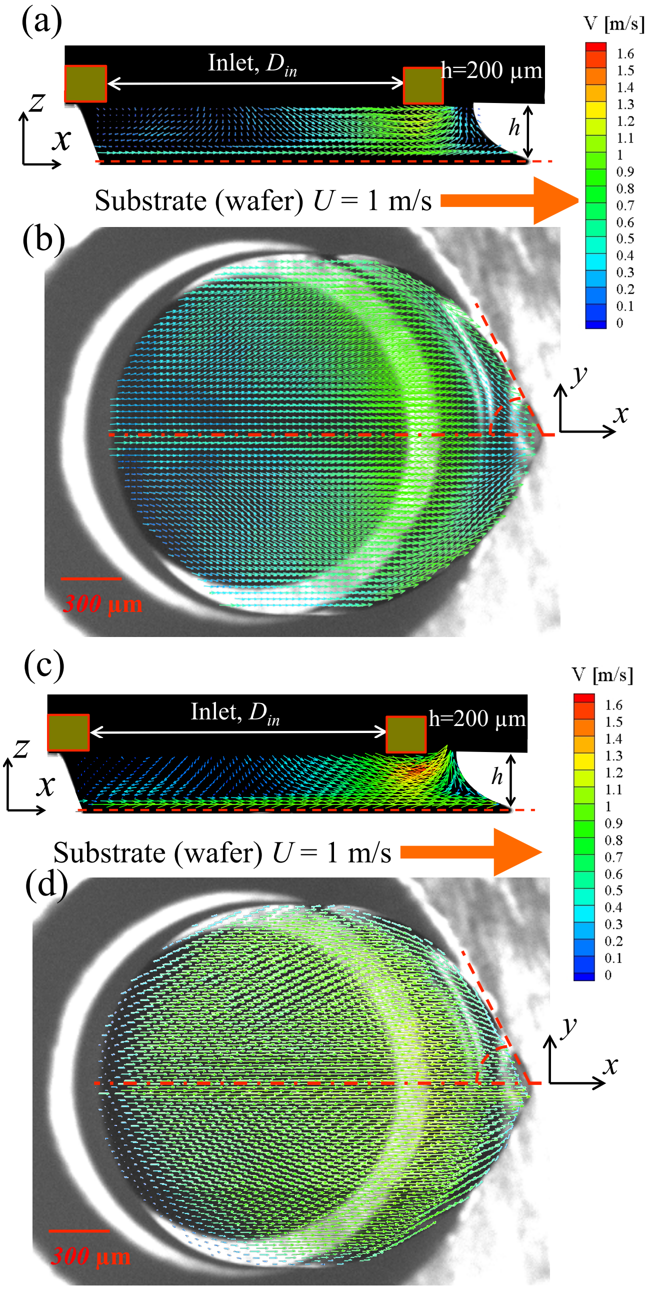

Figure 3.6: 3D-3C vector field obtained by 3D-PTV with $I_t = 10$ counts and $G = 8$ pixels (left) and Tomo-PIV with 50% overlapped 8×8×8 voxels (right) and shadowgraphy of the relatively moving liquid droplet for $\mathrm{Re} = 200$. (a) and (c) are side view at the cross-sectional plane ($y = 0$). (b) and (d) are bottom views at $z \approx 10$ µm. Here, the vector colors represent the magnitude of the 3C velocity vector.

hand, the Tomo-PIV results at the same positions, figure 3.6(c) and (d), provide a reasonable flow pattern based on a visual inspection. In order to quantify the differences the mass conservation at three specified planes, i.e. $z \approx 0$, 180 μm, and 200 μm, is calculated. Mass conservation requires the integral of the w velocity component over the horizontal x-y plane to be exactly zero, because the liquid can not escape the droplet and the droplet is steady. Furthermore, near the top of the droplet we distinguish between the inflow rate and the outflow rate, which are the integrals of the wall normal velocity (w) over the inlet and outlet area (A), respectively. The results are listed in Table 1. The independently measured volume flow rate in the water supply line is about 0.5 μl/s. However, the inflow rate measured by PIV is not exactly this value because of the strong extraction flow field at the outlet. A certain amount of fluid is directly extracted rather than supplied to the droplet. Therefore, the reported flow rate in the supply line is only indicative. Furthermore, the obtained vector plane at the top of the droplet does not match the inlet and outlet positions exactly. Nevertheless, in the case of 3D-PTV, the inflow and outflow are both underestimated in comparison with the Tomo-PIV result by 20 – 60 %. This suggests that Tomo-PIV presents a better result regarding the mass flow at the top of the liquid droplet. Moreover, near the moving substrate ($z = 0$), the net flow (ΔV) of 3D-PTV is three times larger than that of Tomo-PIV indicating larger errors in the 3D-PTV result. In the following sections, we will evaluate the measurement results in more detail in order to highlight the differences that exist between the techniques. First, the volume particle reconstructions are compared since it represents a critical factor determining the accuracy of the velocity field, which is examined thereafter.

3.4.2 Comparison of particle reconstructions

The assessment of the 3D particle reconstruction is not straight-forward, since the actual particle distribution in the volumetric illumination condition is unknown. However, in this problem, we can make estimates by dividing the volume into three different regions, i.e. the glass substrate, the liquid droplet, and the region inside immersion hood. Inside the liquid droplet, there should be actual particles that are uniformly distributed with the reconstruction noise (ghost particles) superimposed. In the glass substrate, there can be no actual particles, hence the reconstruction contains only noise or ghost particles. To evaluate the reconstruction result for Tomo-PIV and 3D-PTV, we count all detected particles in the different regions of the reconstruction. In 3D-PTV, the 3D particles from 25 individual recordings are counted. In Tomo-PIV, we averaged 25 individual reconstructed volume pairs to obtain the dense reconstructed 3D intensity volume. Then, we calculate the total number of intensity peaks.

The 3D-PTV particle distribution in the depth direction is plotted for different intensity threshold values, e.g. $I_t = 1$ count and 10 counts in figure 3.7. The detected particles below the liquid droplet are ghosts ($z < -15$ [px] allowing for some smearing due to the limited depth resolution of the present system due to rather narrow viewing angles). We

Table 3.1: Comparison of flow rates and mass conservations at the bottom and top of the liquid droplet where I_t is the threshold intensity value and G is the grid size. The net-flow rate (ΔV) is calculated by $\int_A w$ dA where w is a normal component and A is an area in the x-y plane.

at $z \approx 200$ µm

	3D-PTV				Tomo-PIV
(I_t [counts], G [pixels])	(1, 4 [px])	(1, 8 [px])	(10, 4 [px])	(10, 8 [px])	(–, 4 [px])‡
Inflow [µl/s]	-0.074	-0.112	-0.126	-0.150	-0.249
Outflow [µl/s]	0.076	0.078	0.103	0.106	0.210
ΔV [µl/s]	0.002	-0.034	-0.023	-0.044	-0.039
Relative error $\lvert\Delta V_{inflow}\rvert$	3%	30%	18%	29%	16%
Relative error $\lvert\Delta V_{outflow}\rvert$	3%	44%	22%	42%	19%

at $z \approx 180$ µm

	3D-PTV				Tomo-PIV
(I_t [counts], G [pixels])	(1, 4 [px])	(1, 8 [px])	(10, 4 [px])	(10, 8 [px])	(–, 4 [px])‡
Inflow [µl/s]	-0.118	-0.167	-0.157	-0.201	-0.253
Outflow [µl/s]	0.116	0.128	0.146	0.160	0.243
ΔV [µl/s]	0.002	-0.039	-0.011	-0.041	-0.010
Relative error $\lvert\Delta V_{inflow}\rvert$	2%	23%	7%	20%	4%
Relative error $\lvert\Delta V_{outflow}\rvert$	2%	30%	7%	26%	4%

at $z \approx 0$ µm

	3D-PTV				Tomo-PIV
(I_t [counts], G [pixels])	(1, 4 [px])	(1, 8 [px])	(10, 4 [px])	(10, 8 [px])	(–, 4 [px])‡
ΔV [µl/s]	0.242	0.207	0.304	0.212	0.086

‡ In the case of Tomo-PIV, the vector results are calculated within 8 × 8 × 8 voxels with 50% overlap. Therefore, the actual grid size is 4 pixels.

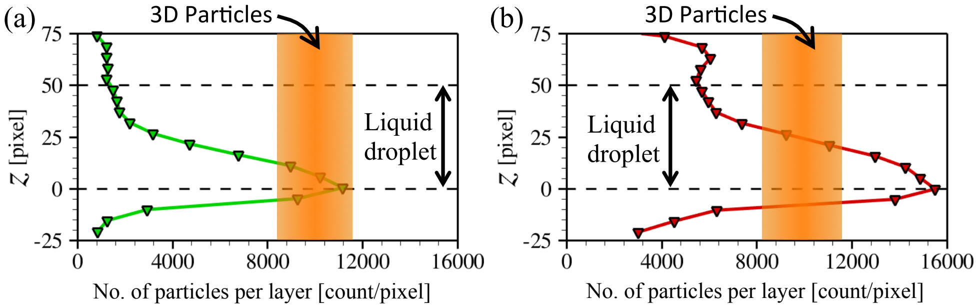

Figure 3.7: Comparison of the total number of particles by 3D-PTV with (a) $I_t = 10$ counts ($ppp = 0.0148$) and (b) $I_t = 1$ count ($ppp = 0.034$) threshold conditions. The orange color region is expected as the number of 3D particles based on the detected number of particles in the images ($I_t = 10$ counts).

can recognize a smooth jump of the detected number of particles at the glass wafer surface ($z = 0$), as shown in figure 3.7(a). In the liquid droplet ($0 \leq z \leq 50$ pixels), there should be both actual and ghost particles. The 3D particle distribution is expected inside the orange zone of figure 3.7 based on a particle count in the images and including ghosts. However, the number of detected particles decreases with the depth direction, so that many of the actual particles are missing at the top of the liquid droplet. This is due to the fact that the depth-of-field is small compared to the whole liquid droplet. Therefore the particle image peak intensity is much weaker near the top, eventually dropping below the threshold (see the section 3.3.2). Therefore, in the case of the stringent intensity threshold value ($I_t = 10$ counts), it can not detect actual particles far from the substrate (i.e. the plane of focus). Additionally, to reduce the effect of the intensity threshold we test the 1 count threshold value. For the 1 count threshold value, the 3D-PTV particle detection is overestimated close to the substrate, as shown in figure 3.7(b). At the substrate, the number of ghost particles are estimated to be more than 50% of the actual number of particles.

In both cases ($I_t = 1$ count and 10 counts), there is a certain level of ghost particles per z-layer, these are estimated at 1220 ghost particles/pixel for $I_t = 10$ counts and 4600 ghost particles/pixel for $I_t = 1$ count. The level of ghost particles is determined in the distribution as shown in figure 3.7 at $z = -15$ pixels. The number of ghost particles are further assumed to be constant with depth. Figure 3.8 shows the distribution of actual particles, which is estimated by subtraction of the ghost level from the profiles of figure 3.7. Although the low threshold value of the intensity provides more ghost particles, more actual particles can be detected far away from the substrate compared to the strict threshold value for the particle detection. Still, the 3D particle distribution inside the liquid droplet should be uniform in the normal direction, which is not the case. On the contrary, in 3D-PTV, the detected number of particles is highly dependent on the depth position, as shown in figure 3.8.

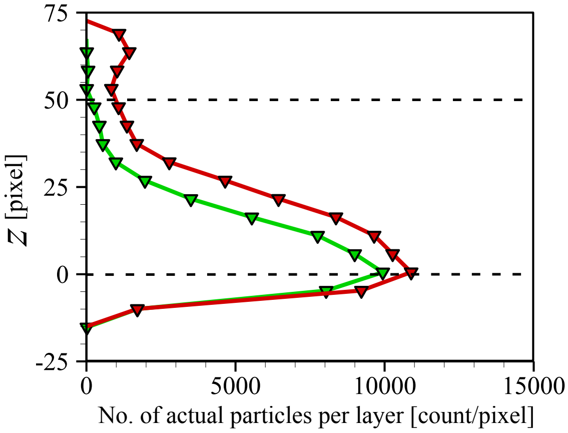

Figure 3.8: Comparison of 3D particle distribution results of 3D-PTV by varying the intensity threshold value ($I_t = 1$ count and 10 counts). Both cases are subtracted a certain amount of ghost particles, e.g. 1220 ghost particles for $I_t = 10$ counts and 4600 ghost particles for $I_t = 1$ count.

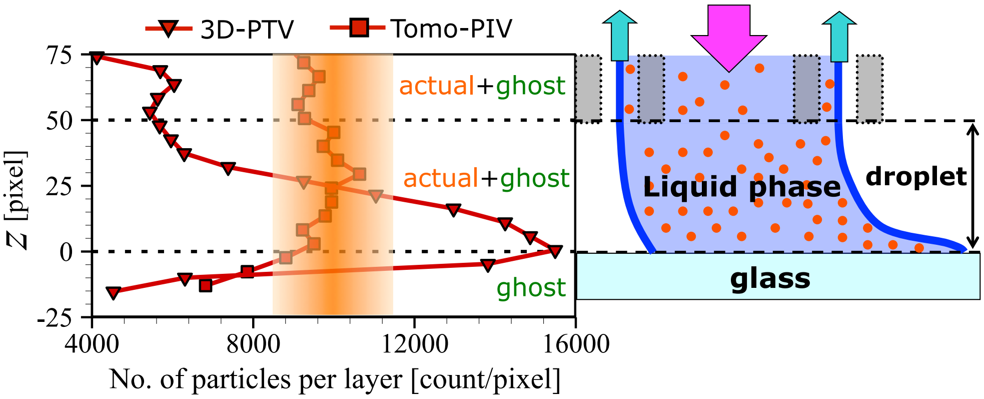

Figure 3.9: Comparison of the total number of particles by 3D-PTV (1 count threshold) and Tomo-PIV in the volume (left) and the schematic of the particle distribution in the droplet (right). The orange region indicates the anticipated number of particles per layer.

In the case of Tomo-PIV, we obtain the particle distribution by counting intensity peaks in the tomographic reconstruction. The peak intensity threshold for accepting the peak as a particle is 1500 counts (corresponding to 3 % of the maximum intensity in the volume). Please note that the tomographic reconstructed volume has been re-scaled to a 64k range, so that the 1500 count threshold should not be compared directly to particle intensity in the recorded images. Figure 3.9 shows the comparison of the 3D-PTV result with $I_t = 1$ count and the Tomo-PIV result. For Tomo-PIV, the detected number of particles (i.e. peaks) inside the liquid droplet is more or less constant (as expected), and equal to about 10^4 particles per depth layer. Moreover, the total number of 3D particles at each z-plane is identical to the expected number of actual particles. We observe that the actual particles are uniformly distributed inside the droplet, as expected. The number of ghost particles can be estimated by using the ppp value. The ghost particles at each z-plane is estimated at about 4700 and the number of actual particles at 5300 per z-layer. The corresponding particle image density can then be estimated by multiplying the number of particles per layer by the height of the volume (50 pixels) and dividing it by the number of sub-volumes used in the volume intensity averaging (25) and the field of view (606×510 pixels). The resulting particle image density is 0.034 ppp. Both the number of ghost particles as well as the derived particle image density are in a good agreement with the case of 3D-PTV for $I_t = 1$ count. Although the peak intensity magnitude decays in the depth direction, as mentioned in section 3.3.2, Tomo-PIV provides the expected uniform distribution of reconstructed 3D particles.

We also examine the consistency between the number of particles in the recorded images and in the reconstructed result for 3D-PTV. In the raw images, the seeding density (ppp) is 0.034 ($I_t = 1$ count). In the reconstructed volume, the number of actual particles integrated over the height of the droplet is about 2.5×10^5 actual particles in the volume, which is agreement with the total number of actual particles in tomographic reconstructed volume and the corresponding particle image seeding density of 0.034 ppp. However, the 3D particle reconstruction by PTV has a very different distribution over the volume height. It is difficult to firmly conclude which one is absolutely correct, but based on the discrepancy between the measured and the expected velocity distribution at the bottom wall (figure 3.6), it can be said that 3D-PTV likely suffers from falsely detected particle images near the wall (z=0), which introduces artifacts in the measured velocity distribution.

Furthermore, we conclude that the particle reconstruction signal-to-noise ratio in the present experimental study decreases with height. In the case of Tomo-PIV, it is observed that the number of reconstructed particles per unit volume remains constant although there is a certain level of ghost particles. However, the reconstructed intensity of actual particles decreases, as shown in figure 3.4. As a result, the signal strength decreases compared to the noise level, which is assumed to be approximately constant. Consequently, the signal-to-noise ratio drops. In the case of 3D-PTV, the number of reconstructed particles per unit volume is reduced with height as shown in figure 3.7. The particle intensity is irrelevant in the triangulation (and each triangulated particle pair equally contributes a displacement vector). Again, assuming an approximately constant density of ghost particles,

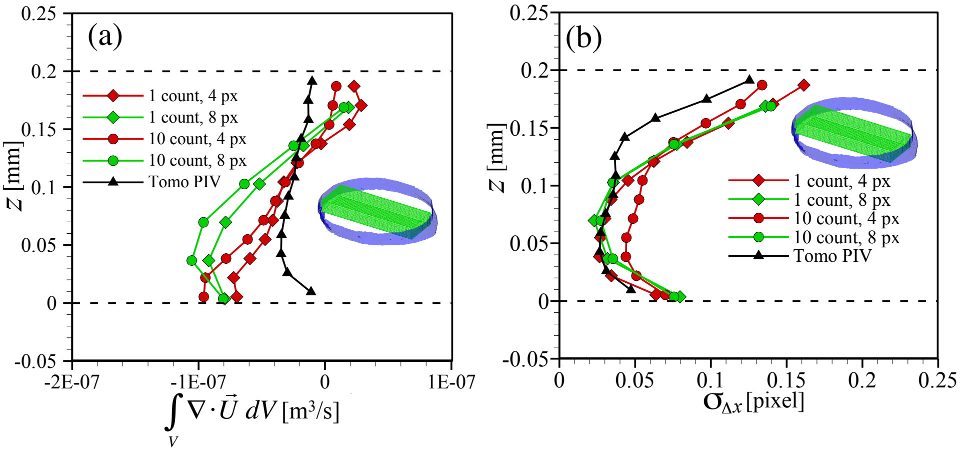

Figure 3.10: Comparison of accuracy of 3D-PTV and Tomo-PIV for the confined shear-driven liquid droplet at Re = 200. (a) Divergence error and (b) measurement accuracy are calculated for the green rectangular domain inside the liquid droplet. For 3D-PTV case, two intensity threshold values ($I_t = 1$ and 10) and two different grid systems (grid size = 4 and 8 pixels) are examined. Tomo-PIV is applied with the 3D cross-correlation with the 8×8×8 voxels interrogation volume with 50 % overlap.

the reconstruction signal-to-noise ratio also decreases with height, but for a different reason. In turn, the decreasing reconstruction signal-to-noise ratio is expected to increase the velocity measurement uncertainty and accuracy, which is investigated next.

3.4.3 Assessment of velocity accuracy and divergence

We quantitatively assess the velocity results of the two measurement methods. In the case of 3D-PTV, the final vector result depends on the PTV settings, in particular the intensity threshold value (I_t) and the grid system size (G). We consider $I_t = 1$ and 10 counts and $G =$ 4 and 8 pixels. Then, to assess the reliability and accuracy of our measurement system, the mass conservation in every point is examined from the continuity equation, i.e. local flow divergence. To investigate the errors along the depth direction, we choose a sub-volume inside the droplet, as shown in the inset (the green rectangular zone) of figure 3.10. The divergence RMS error can be related to the overall amplitude for the particle displacement error $\sigma_{\Delta x}$ [pixel] (Adrian and Westerweel 2010). To take into account the propagation of uncertainty, the systematic errors can be estimated by:

$$\overline{\left(\frac{\partial u}{\partial x}+\frac{\partial v}{\partial y}+\frac{\partial w}{\partial z}\right)^2} \cong C\left(\frac{\sigma_{\Delta x}}{2D_I\Delta t}\right)^2, \tag{3.3}$$

where D_I is the dimension of the grid step; Δt, the time delay between two frames ($\Delta t =$ 10 µs); and C, a constant depending of the differential scheme. The velocity gradients are calculated with the central second-order difference scheme, for which $C = 6$.

The results are presented in figure 3.10 where the black solid line indicates the Tomo-PIV result and the red ($G = 4$ pixels) and green ($G = 8$ pixels) solid lines are for 3D-PTV. The average divergence errors are plotted in figure 3.10(a), indicating a larger bias error in the 3D-PTV over the volume height. The accuracy of the particle displacement is assessed by comparing the results based on equation 3.3, which is shown in figure 3.10(b). The divergence error distributions are fitted against a Gaussian function and then the standard deviation at each z-plane is plotted. Both methods present the error amplitude of the particle displacement $\sigma_{\Delta x}$ between 0.03 – 0.17 pixels. This error is consistent with a typical the measurement uncertainty reported for Tomo-PIV (2008). However, the error varies strongly with depth, being lowest near the plane of focus, where the signal in the particle reconstruction is highest, as shown in the previous section. Exactly at the wall ($z = 0$) the error increases, but this is more likely due to local inaccuracies in determining the velocity gradient from central differences.

3.4.4 Quantitative comparison of velocity profiles

In this section, profiles are extracted from data at three specific points to quantitatively compare the 3D-3C velocity components and shown in figure 3.11. Overall, the streamwise velocities are in a good agreement between 3D-PTV and Tomo-PIV. However, the normal velocity components reveal significant deviations. In particular, at the extraction part (figure 3.11c), the result of 3D-PTV underestimates the normal velocity components in comparison with Tomo-PIV. In addition, the flow pattern must be parallel to the substrate at the wall ($z = 0$) but 3D-PTV shows an upward fluid motion. Furthermore, for the same settings, the 3D-PTV gives inconsistent results in the local velocity profiles. For instance, in the case of $I_t = 1$ counts and $G = 4$ pixels, 3D-PTV gives the best agreement with Tomo-PIV for the w-velocity component, as shown in figure 3.11(i). On the other hand, figure 3.11 (c) shows that the case of $I_t = 10$ counts and $G = 8$ pixels matches with the Tomo-PIV result and the case of $I_t = 1$ count and $G = 4$ pixels appears to present the worst result locally; there should be inflow ($w < 0$) but with these settings PTV gives $w \approx 0$. As a conclusion, the 3D-PTV accuracy is highly dependent on the local flow structure and no setting is found to yield consistently accurate results throughout the volume of the droplet.

Furthermore, we compare the RMS velocity profiles between 3D-PTV and Tomo-PIV to further evaluate these results. In this study, the flow is steady and hence the RMS velocity is representative of a measurement uncertainty. We choose the same spatial resolution, i.e. $G = 4$ pixels. Figure 3.12s (a)-(c) show the local RMS fluctuations at $(x, y) = (0.88, 0.0)$ mm, which is close to the extraction part (location C in figure 3.11). The profiles show that the Tomo-PIV result has a lower RMS error in comparison with the 3D-PTV results. Furthermore, we compare the RMS fluctuations averaged over the x and y direction within

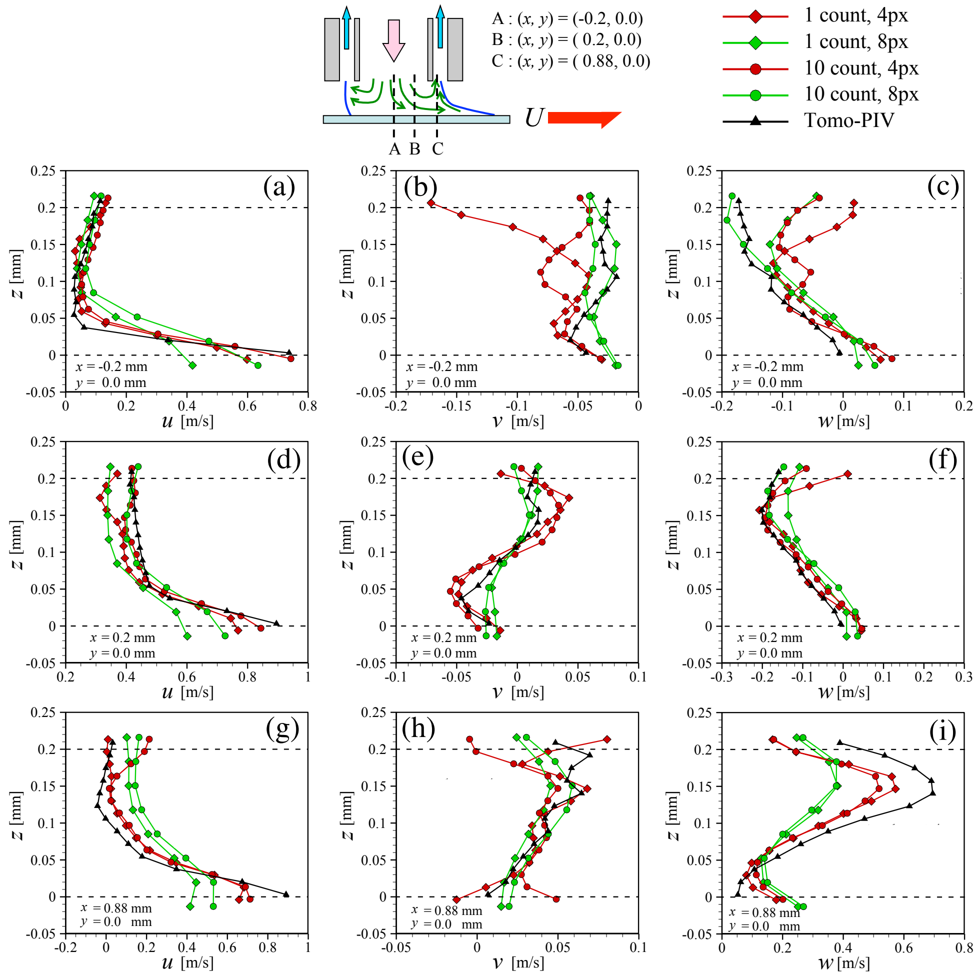

Figure 3.11: Comparison of profiles for u, v, w velocity components at position A (a, b, c), B (d, e, f) and C (g, h, i) positions inside the liquid droplet over the moving substrate with $U = 1$ m/s (see schematic of the droplet at the top). For 3D-PTV, the different symbols indicate the intensity threshold value, e.g., the diamond symbol is for 1 count and the circle is for 10 counts. The black triangular symbol is for Tomo-PIV (see also the legend at the top).

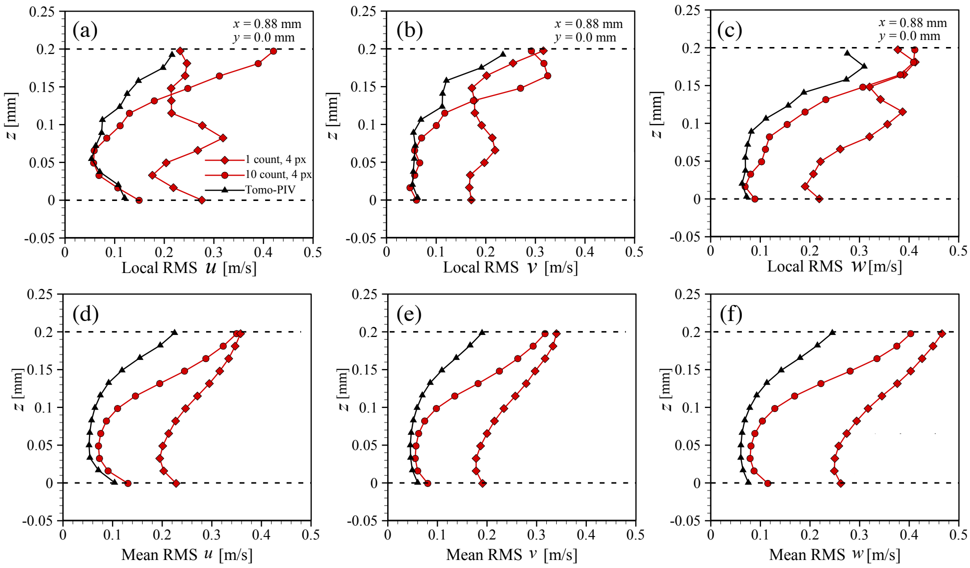

Figure 3.12: Comparison of the (a) local and (b) mean RMS fluctuations of u, v, w velocity components averaged over a z-plane. The local error is plotted along the depth direction at $(x, y) = (0.88, 0)$ mm. and the mean error is averaged in every z-plane for the sub-volume (see the inset of figure 3.10) inside the liquid droplet.

the sub-volume (see the green rectangular inset of figure 3.10). For the RMS errors, the Tomo-PIV results show smaller errors. For 3D-PTV, the result of $I_t = 10$ counts has a low RMS error compared to $I_t = 1$ count. Still, the RMS error of 3D-PTV is higher than the result of Tomo-PIV. In particular, at the top of the liquid droplet, the error becomes larger, which appears consistent with the increase in the average error near the top (figure 3.10) and the decreasing particle reconstruction signal-to-noise ratio, as discussed in section 3.4.2.

3.5 Discussion and conclusion

We used two 3D-3C velocity measurement techniques, i.e. Tomo-PIV and 3D-PTV, to measure the steady flow in a droplet. The methods are assessed experimentally comparing the particle reconstructions and the resulting velocity fields. We observe considerable differences. Firstly, the 3D particle distributions in the volume obtained by 3D-PTV varied along the droplet height, while Tomo-PIV gives a constant 3D particle distributions over the depth. However, in the latter case, the average intensity of the reconstructed particles decreases with depth. Therefore, the strength of the signal, that is the reconstructed particles, decreases with the distance to the wall for both methods, but in different ways. For 3D-PTV, the number of detected particles decreases, whereas in Tomo-PIV the reconstructed particle intensity drops. The depth variation in the particle reconstructions of both methods is caused by the particles at increasing wall normal distance being progressively imaged out of focus, which increases their image diameter and decreases their image peak intensity. Note that the plane of focus was located at the wall in this experiment. In addition, differences in the velocity field between two measurement results are clearly observed at certain regions where the shear is rather strong. In particular near the substrate and near the rear part of the outlet, significant differences exist in the degree to which mass conservation of the experimental data is satisfied. Overall Tomo-PIV shows smaller random errors (figure 3.10). Furthermore, the uncertainty in the velocity measurement is less for Tomo-PIV (figure 3.12). For both methods, the RMS fluctuations of the three velocity components increase towards the top of the liquid droplet, which indicates increasing measurement uncertainty. These results are related to the present experimental conditions, mainly a small depth-of-field compared to the droplet height, and a complex flow pattern at a small scale. This causes the signal-to-noise ratio to drop with the height for both methods but for different reasons (decreasing number of reconstructed particles versus decreasing reconstructed intensity). Therefore, the rate at which the methods break down is different. Suppose we specify a threshold for the acceptable measurement uncertainty in this experiment at 0.1 m/s, then the thickness over which the methods yield good results increases by 20-50% for Tomo-PIV compared to 3D-PTV (figure 3.12). Moreover, it is worth noting that no single set of PTV processing parameters, i.e. I_t and G, produces the best possible 3D-PTV measurement result throughout the entire domain. Using high I_t and G yields more accurate velocity vectors near the center of the drop, whereas using low I_t and G returns better results near the extraction part (figure 3.11). Therefore, it is concluded that Tomo-PIV appears capable of measuring the complex micro-scale flow patterns more robustly and accurately, over an increased volume thickness compared to 3D-PTV.

3.6 Acknowledgments

We would like to thank B. Wieneke from LaVision GmbH for his contribution to the data post-processing and valuable advice.

3.7 Bibliography

R. J. Adrian and J. Westerweel. *Particle Image Velocimetry*. Cambridge University Press., 2010.

J. Agüí and J. Jimenez. On the performance of particle tracking. *J FLUID MECH*, **185**, 447, 1987.

C. M. Balan, D. Broboana and C. Balan. Mixing process of immiscible fluids in microchannels. *INT J HEAT FLUID FL*, **31**, 1125, 2010.

Y. S. Choi et al. Advances in digital holographic micro-PTV for analyzing microscale flows. *OPT LASER ENG*, 2011.

C. Cierpka and C. J. Kähler. Particle imaging techniques for volumetric three-component (3D3C) velocity measurements in microfluidics. *J VISUAL-JAPAN*, 1–31, 2012.

C. Cierpka et al. A comparative analysis of the uncertainty of astigmatism-μPTV, stereo-μPIV, and μPIV. *EXP FLUIDS*, **52**, 605, 2012.

T. Dracos and T. Dracos. *Three-dimensional velocity and vorticity measuring and image analysis techniques: lecture notes from the short course held in Zuerich, Switzerland, 3-6 September 1996*, volume 4. Kluwer Academic Pub, 1996.

G. E. Elsinga. *Tomographic particle image velocimetry and its application to turbulent boundary layers.* Ph.D. thesis, Delft University of Technology, 2008.

G. E. Elsinga et al. Tomographic particle image velocimetry. *EXP FLUIDS*, **41**, 933, 2006.

G. E. Elsinga et al. On the velocity of ghost particles and the bias errors in tomographic-PIV. *EXP FLUIDS*, **50**, 825, 2011.

K. D. Kihm et al. Near-wall hindered brownian diffusion of nanoparticles examined by three-dimensional ratiometric total internal reflection fluorescence microscopy (3-D R-TIRFM). *EXP FLUIDS*, **37**, 811, 2004.

H. Kim et al. Experimental investigation of internal flow in an immersion droplet by 3D-PTV. In *Proc. of the 14th International Symposium on Flow Visualization*, 2010.

H. Kim et al. Full 3D-3C velocity measurement inside a liquid immersion droplet. *EXP FLUIDS*, **51**, 395, 2011.

H. Kinoshita et al. Three-dimensional measurement and visualization of internal flow of a moving droplet using confocal micro-PIV. *LAP CHIP*, **7**, 338, 2007.

A. Kloosterman, C. Poelma and J. Westerweel. Flow rate estimation in large depth-of-field micro-PIV. *EXP FLUIDS*, **50**, 1587, 2011.

R. Lindken, J. Westerweel and B. Wieneke. Stereoscopic micro particle image velocimetry. *EXP FLUIDS*, **41**, 161, 2006.

H. W. Lu et al. A study of EWOD-driven droplets by PIV investigation. *LAB CHIP*, **8**, 456, 2008.

H. G. Maas, A. Gruen and D. Papantoniou. Particle tracking velocimetry in three-dimensional flows. *EXP FLUIDS*, **15**, 133, 1993.

T. Ooms, R. Lindken and J. Westerweel. Digital holographic microscopy applied to measurement of a flow in a T-shaped micromixer. *EXP FLUIDS*, **47**, 941, 2009.

J. S. Park, C. Choi and K. D. Kihm. Optically sliced micro-PIV using confocal laser scanning microscopy (CLSM). *EXP FLUIDS*, **37**, 105, 2004.

J. S. Park, C. K. Choi and K. D. Kihm. Temperature measurement for a nanoparticle suspension by detecting the brownian motion using optical serial sectioning microscopy (OSSM). *MEAS SCI TECHNOL*, **16**, 1418, 2005.

J. S. Park and K. D. Kihm. Three-dimensional micro-PTV using deconvolution microscopy. *EXP FLUIDS*, **40**, 491, 2006.

F. Pereira et al. Microscale 3d flow mapping with μDDPIV. *EXP FLUIDS*, **42**, 589, 2007.

J. Sheng, E. Malkiel and J. Katz. Digital holographic microscope for measuring three-dimensional particle distributions and motions. *APPL OPTICS*, **45**, 3893, 2006.

K. Shinohara et al. Development of a three-dimensional scanning microparticle image velocimetry system using a piezo actuator. *REV SCI INSTRUM*, **76**, 106109, 2005.

S. T. Wereley and C. D. Meinhart. Recent advances in micro-particle image velocimetry. *ANNU REV FLUID MECH*, **42**, 557, 2010.

B. Wieneke. Volume self-calibration for 3D particle image velocimetry. *EXP FLUIDS*, **45**, 549, 2008.

CHAPTER 4

EXPERIMENTAL AND THEORETICAL INVESTIGATION OF DEWETTING CORNER [1]

Abstract

We study a partial dewetting corner flow with moving contact line at a finite Reynolds number, $0 < Re < O(100)$. When the speed of the moving contact line increases, the receding contact line appears with a corner shape that is also observed in a gravity-driven liquid droplet on an incline and on a plate withdrawn from a bath. This problem can be described by a three-dimensional lubrication model that is limited to low Reynolds numbers ($Re \ll 1$) and low receding contact angles. However, surprisingly enough, this corner feature also appears in a liquid-immersion lithography machine where the Reynolds number is of the order of 100. Furthermore, $Re{\cdot}\epsilon$ is larger than unity where ϵ is the aspect ratio of the flow structure. The classical lubrication model is then not appropriate. We develop a modified three-dimensional lubrication model for the dewetting corner structure at $Re{\cdot}\epsilon > 1$ by taking into account the internal flow pattern and by scaling arguments. The key requirement is that the streamlines in the corner are straight and parallel. Then we can obtain a modified pressure consisting of the capillary pressure and the dynamic pressure. This model describes the three-dimensional dewetting corner structure at the rear of the moving droplets at $Re \sim O(100)$ and furthermore shows that the dynamic pressure effects become dominant at a small opening angle. Additionally, this model provides analytical results for the internal flow velocity, which is a self-similar flow pattern. To validate the analytical results, we perform high-speed shadowgraphy and tomographic particle image velocimetry. We find a good agreement between the theoretical and the experimental results.

---

[1] The content of this chapter will be submitted to Journal of Fluid Mechanics (Kim et al. 2013).

4.1 Introduction

From nature to industry, wetting and de-wetting flow structures occur in various hydrodynamic problems (Bonn et al., 2009). There is an unbalanced divergence of the viscous stress in the vicinity of the contact line due to a hydrodynamic singularity (Huh and Scriven, 1971). It is still difficult to provide a fundamental description of moving contact lines. To resolve the logarithmically divergent viscous dissipation, different approaches are used. For instance, molecular dynamics (MD) simulations (Blake, 2006; Gentner et al., 2003) and Lattice-Boltzman (LB) simulations (Blake et al., 1995; Mo et al., 2005) are done to study mechanism of contact line dynamics. However, MD simulations are not well suited and the small simulation volume to study macroscopic systems due to the limited number of particles (Bonn et al., 2009) and LB simulations require a proper diffusion boundary condition at the liquid-gas interface (Briant and Yeomans, 2004). From a hydrodynamic point of view, two methodologies have arisen to remove the singularity: either a slip boundary condition at the contact line is applied (Brochard-Wyart and De Gennes, 1992), or a partial wetting structure near a contact line is assumed between the macroscopic layer and the thin film (Gennes, 1985). Based on these approaches, the wetting and de-wetting dynamics can be described by means of the Navier-Stokes equations.

To study wetting and de-wetting flow problems, classical lubrication theory is a useful approach to simplify the governing equations. When $Re{\cdot}\epsilon$ is much smaller than unity, the flow field can be assumed to be in the Stokes regime, i.e. with negligible nonlinear convective acceleration terms (Reynolds, 1886; White, 2005). Here, Re ($= \rho U H/\mu$; ρ denotes density; U, the substrate speed; H, the characteristic length; μ, viscosity) is the Reynolds number and ϵ ($= h/L$; h, the height; L, the streamwise length) represents the flow geometry.

Recently, Limat and Stone (2004) presented a three-dimensional lubrication model for the de-wetting corner structure of a droplet sliding down on an inclined substrate in the framework of lubrication theory. They used a similarity solution to describe the contact line shape of the three dimensional structure near the corner singularity. Then, they showed that two angles θ (dynamic receding contact angle) and Φ (corner opening angle) are linked to each other. Furthermore, based on this model, Snoeijer et al. (2005) obtained the analytical solution for the internal flow field near the corner structure, which showed a self-similar flow pattern. These models are limited to low Reynolds number ($Re \ll 1$) and low dynamic receding contact angle ($\theta < 20°$).

Interestingly, in an industrial application, qualitatively similar results are observed in flows where the conventional lubrication approximation no longer holds, i.e. $Re{\cdot}\epsilon > 1$. An example of this similarity is shown in figure 4.1, i.e. a gravity-driven liquid droplet on an incline ($Re \ll 1$) and an immersion droplet over a moving substrate ($Re \sim O(100)$). For the gravity-driven liquid droplet case, the droplet speed is proportional to the inclination angle of the substrate. The immersion droplet speed is determined by the moving substrate. The confined liquid droplet (i.e. the immersion droplet) over a moving substrate (i.e.

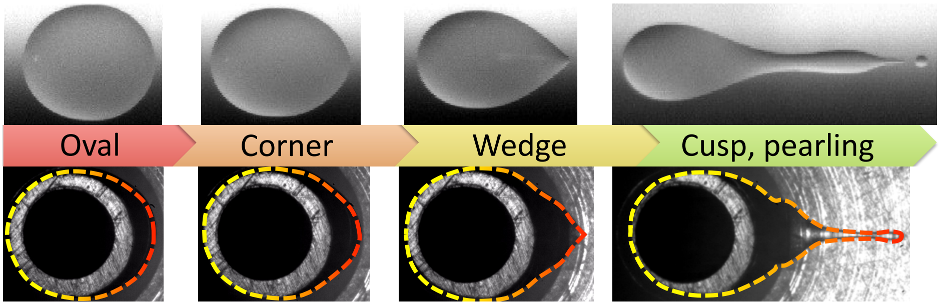

Figure 4.1: Comparison of the transition of the droplet shape in two different geometries and at different Reynolds numbers. The upper row shows sessile drops on an inclined substrate at $Re \ll 1$. Images taken from Podgorski et al. (2001). The bottom row shows a droplet in a model for an immersion lithography machine at $Re \sim O(100)$. In the bottom row, the gray-rounded rim that can be seen inside the droplet is the needle device to supply the flow. The yellow-red-dashed lines represent the contour of the droplet. Both sets of image are views from the bottom through the transparent glass substrate.

partially wetting and dewetting flow structure) is used to improve the spatial resolution of optical lithography, i.e. the so-called immersion lithography (Mulkens et al., 2004; Owa and Nagasaka, 2008). In this case, the wetting and dewetting speed of contact lines increases to about 1 m/s, i.e. $Re \sim O(100)$ for water (Kim et al., 2011; Riepen et al., 2008). In particular, in both cases, the rear part of the droplet evolves from a round shape to a cusp shape when the contact line speed increases. Furthermore, droplet break-up occurs when the corner opening angle Φ becomes sharper than an angle close to $\Phi = 30°$ (Podgorski et al., 2001; Riepen et al., 2008; Stone et al., 2002). However, so far no explanation for this similarity has been reported.

In this chapter, we perform experimental and theoretical analysis for the dewetting corner flow problem at $Re{\cdot}\epsilon > 1$. First, we observe the shape of a partial dewetting flow structure from the side and bottom view by means of shadowgraphy. From this result, we construct a scaling argument and then we obtain an empirical model to depict the corner structure of the partial dewetting at $Re \sim O(100)$. This model describes the conical structure by θ and Φ (see the definition of symbols in figure 4.2 (b)). Furthermore, based on a scaling argument, we assume that the normal components of the velocity and vorticity are negligible compared to the other components. To measure the three-dimensional three-component (referred to as 3D-3C) velocity vectors in a volume, we perform tomographic particle image velocimetry (referred to as Tomo-PIV). Through further investigation of the flow pattern, we postulate that the streamlines are straight and nearly parallel in different cross-sectional planes. Based on these results, we present a modified three-dimensional lubrication model for the dewetting corner structure at $Re{\cdot}\epsilon > 1$. The model shows that dynamic receding contact angles θ and corner opening angles Φ are correlated

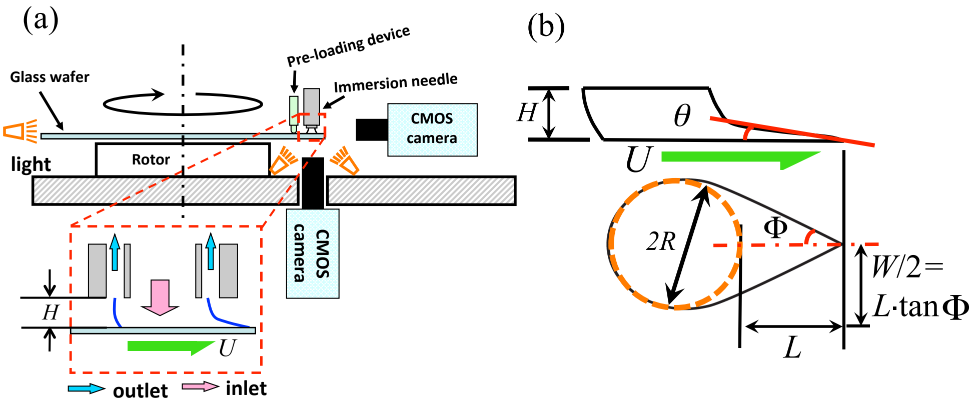

Figure 4.2: High-speed recording shadowgraphy technique for the side and bottom views; (a) schematic of the experimental setup. The red-dashed box shows a sketch of a liquid immersion droplet over the moving substrate, where H is the height of the droplet and U is the velocity of the substrate. (b) the geometry and definition of the coordinate systems in the droplet shape, where θ is the dynamic receding contact angle, Φ is the half opening angle, R is the radius of the main drop, and L is the length of the elongated tail.

with each other. In the model, the modified pressure consists of the capillary pressure and the dynamic pressure. When the corner shape is sharper (small Φ or high speed U), the dynamic pressure effects become important, which is validated by the approximate analytical and the experimental results. Furthermore, the model shows that the depth-averaged velocity profile of the corner structure resembles a self-similar flow pattern. We measure the flow pattern for two cases where $\Phi = 40°$ and $75°$, by means of Tomo-PIV. The analytical results are validated and confirmed by the experimental data.

4.2 Experiments

4.2.1 High-speed shadowgraphy recording

We perform a high-speed shadowgraphy measurement to observe the shape of partial dewetting droplet over a moving substrate. The schematic of the experimental setup is shown in figure 4.2. The liquid droplet is generated by a so-called immersion needle (see the red-dashed box of figure 4.2 (a)). To maintain a constant volume of the droplet, water is supplied to the center of the droplet through the inner part of the immersion needle. Then water and air are simultaneously extracted through an annular tube around the inlet. The volume of generated drops ranges from about 200 nl to 950 nl by varying the height (H) of the droplet, $200\ \mu\text{m} \leq H \leq 300\ \mu\text{m}$. The droplet has a 1 mm radius (R). The liquid droplet is located near the edge of a 12 inch glass wafer, which spins with a constant acceleration up to the critical velocity. Above the critical velocity, the droplet starts to loose satellite droplets at its tail (pearling, figure 4.4 (d) and 4.5 (e)). While rotating the wafer, a pre-loading device maintains a constant position of the wafer in the vertical direction. It has been demonstrated earlier that there is no noticeable centrifugal force effect in the flow pattern (Kim et al., 2011).

Three different substrate conditions are used, where the static contact angle θ_s is 89±8°, 76±8°, and 63±15°. The substrates are coated by ASML Holding NV. To observe the contour of the bottom view a transparent glass wafer is used. The glass wafer is provided from Silicon Valley Microelectronics, Inc. The working fluid is distilled water with a dynamic viscosity $\mu = 10^{-3}$ Pa·s, a surface tension $\gamma = 72$ mN/m, and a density $\rho = 10^3$ kg/m^3. The working fluid is continuously circulating to maintain the constant room temperature (298 K). Here, it should be noted that the Reynolds number ($Re = \rho U H/\mu$) characterized by the height of the droplet is of the order of 100, where U is the speed of the wafer and H is the total height.

The motion is recorded via a high-speed CMOS camera (Photron SA3), with a resolution of 1024 ×1024 pixels and a 12-bit dynamic range and a framing rate of one thousand frames per second. The camera is equipped with a long range microscope (Navitar 10X Telecentric Zoom system) giving a resolution of 5 μm/pixel for the side view and 3 μm/pixel for the bottom view. The wafer substrate is accelerating with 1 m/s^2 at the position of the droplet during the measurement. Nevertheless, we assume a quasi-steady state, because the time scale for the interface change is very short, which is the order of 10^{-6} [s] (Blake and Shikhmurzaev, 2002; Eggers and Evans, 2004). This time scale is given by the time scale of momentum diffusion. The required time scale for the interfacial formation is extremely short compared with other dynamic values.

4.2.2 Tomographic particle image velocimetry

Recently, Tomo-PIV has become widely used to measure three-dimensional three-component (referred to as 3D-3C) velocity vectors that can be applied to both microscopic scales (Kim et al., 2011) and a large scale turbulent problems (Elsinga, 2008). Furthermore, Tomo-PIV is able to reconstruct the liquid-air interface, and hence it is possible to apply the velocity measurement to a flow domain with a free surface (Kim et al., 2012). Figure 4.3 shows the experimental setup for the volumetric flow measurement. To obtain the three velocity components in a volume we install four CCD cameras (LaVision Imager Intense), each with a resolution of 1376 × 1040 pixels and a 12-bit dynamic range. In this experimental configuration, the equivalent linear dimension of a single pixel in the object domain is 4 μm. To observe the internal flow field of the partial dewetting flow, the entire volume needs to be accessed without minimal distortion, due to refraction at the interface. Also we must avoid shading reflection. Therefore, the four cameras are mounted on an inverted custom-made microscope, as shown in figure 4.3 (b). The optical path of each camera is

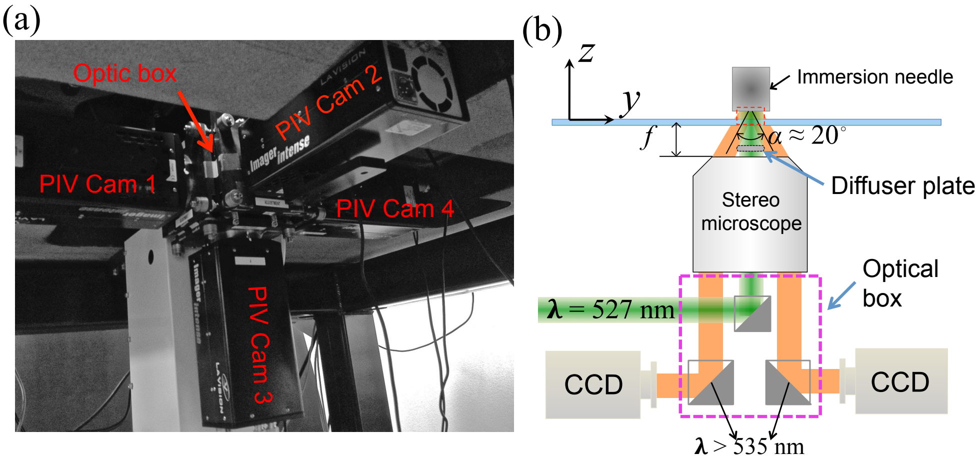

Figure 4.3: Tomographic particle image velocimetry set-up. (a) Illustration of the PIV setup, with four PIV cameras mounted on a custom-made microscope at the bottom of the setup. (b) Cross-sectional schematic of the PIV set-up. The focal length f is about 31 mm and the inner aperture is about 7 mm inside the lens. The particles inside the immersion droplet are volumetrically illuminated at 527 nm wavelength. A diffuser plate is installed before the laser beam enters stereo microscope. In the optical box, the filters are installed in front of each CCD camera that only transmit light with wavelengths longer than 535 nm. The laser beam path is also included in the optical box.

off-axis through a single microscope objective lens with a magnification of 1.5. The offset angle between the optical axes of the cameras is about $\alpha \approx 20^{\circ}$ (see figure 4.3 (b)). The laser beam diameter L_d is almost 5 mm. An optical diffuser plate is used to avoid speckle effects. As shown in figure 4.3 (b), the custom-made microscope is installed at about 30 mm below the wafer surface. The depth-of-field is given approximately by $\Delta z_0 \cong 4(1+1/M_0)^2 f^{\#2}\lambda$, where Δz_0 is the depth-of-field; M_0, the magnification of the lens; $f^{\#}$, the f-number of the lens; λ, the wavelength of the light. For the given optical parameters we have $\Delta z_0 \approx 120\,\mu$m. The accuracy of the present experimental system is evaluated in preceding studies (Kim et al., 2012, 2011).

To measure the flow field, the working fluid is seeded with 1.28 μm tracer particles (Microparticles GmbH, Germany). The particles are labeled with a fluorescent dye (Rhodamine-B) and the particles are coated with polyethylene glycol (PEG). This PEG-coating avoids particle coagulation and attachment to the solid surface and to the free-surface. Fluorescence is excited by a dual cavity frequency-doubled pulsed Nd:YLF ($\lambda = 527$ nm, Pegasus - New wave research) high-speed laser. The final image density (N_I) is 5.38×10^{-1}, given by $N_I \equiv C A_I \Delta z_0 / M_0^2$, where C is the mean number of particles per unit volume [m^{-3}], M_0, the magnification of the lens, Δz_0, the depth-of-field [m], and A_I, the image interrogation area [m^2]. The particle image seeding density ppp is 0.034 (particles per pixel) as determined from a raw image. The value corresponds to a source density $N_S \simeq 0.09$ (Adrian and Westerweel, 2010). Those values are considered to represent a relatively low seeding density. This is not adequate for resolving the small-scales of the fluid motion close to the moving contact line. In order to effectively increase the density of the reconstructed particle, the 3D intensity volumes are averaged over 25 individually reconstructed volume pairs.

For the multi-camera PIV system, calibration is necessary to correct for the different projections recorded on each of the CCD cameras. A calibration of the image mapping is performed by 3D calibration, and the calibration is corrected by means of volume self-calibration (Wieneke, 2008). After the calibration, the disparity error between the different views is less than 0.05 pixels. The whole pre- and post-processing and calibration procedures are performed by means of a commercial code (Davis 8.05, LaVision GmbH).

For Tomo-PIV, the MART (multiplicative algebraic reconstruction technique) algorithm is used with 5 iterations and with the relaxation parameter $\mu = 1$ (Elsinga, 2008). The velocity is obtained by performing 3D cross-correlations of the reconstructed particle distribution in the measurement volume with an interrogation volume of 8 × 8 × 8 voxels with 50% overlap. The spatial discretization is 250 voxels/mm. The PIV experimental details are described in detail by Kim et al. (2012, 2011).

4.3 Experimental results and discussion

4.3.1 Scaling analysis

We observe the shape of the partial dewetting flow from the bottom and side view by means of shadowgraphy. Figure 4.4 and 4.5 show an example of the evolution of the partial dewetting by increasing the substrate speed where the substrate is hydrophobic, $\theta_s = 89 \pm 8^\circ$. At the early stage, the tail structure has a large slope (θ) and a short tail (L) as shown in figure 4.4 (a). As the substrate speed increases, the tail becomes elongated as shown in figure 4.4 (b-c). When the critical speed is reached, it begins to lose a fluid (i.e. droplet breakup), as shown in figure 4.4 (d). Figure 4.5 shows the shape change of the partial dewetting contact lines in the bottom view, i.e. oval ⇒ corner ⇒ cusp ⇒ pearling. Furthermore, figure 4.6 shows the evolution of the aspect ratio ($\epsilon = h/L$) by increasing the substrate speed. The tail length (L) is defined in figure 4.4 and the local height (h) is defined in the inset of figure 4.6. At the early stage, the aspect ratio is $\epsilon \geq 1$. In particular, in the case of $\theta_s = 89 \pm 8^\circ$ (square symbols in figure 4.6), the elongated droplet tail is short compared to the local height (h). This is due to the hydrophobic surface. In the case of hydrophilic substrates, the aspect ratio is smaller than for the hydrophobic one in the early stage. However, for all cases, as the substrate speed increases, the droplet shape becomes elongated and thin like a thin-film flow structure.

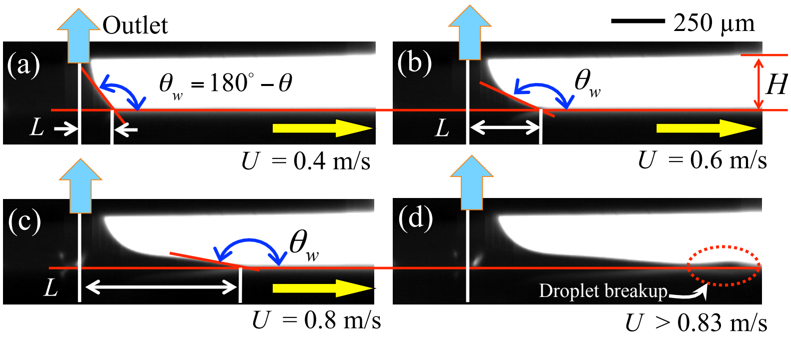

Figure 4.4: Evolution of the dynamic receding contact angle $\theta = 180^\circ - \theta_w$ where the height of the structure is 250 µm. The elongated liquid droplet tail L varies with the speed of the substrate U, which is observed from side by a shadowgraphy measurement. The blue arrow indicates the outlet of the device.

Based on the shadowgraphy results, we perform a scaling analysis for the partial dewetting flow at intermediate Reynolds number. The following representative scales are taken into consideration:

- Local height of the liquid drop: $50\ \mu\text{m} \leq h \leq 100\ \mu\text{m}$
- Length of the liquid drop tail: $0 \leq L \leq 1$ mm (for $R = 1$ mm)
- Substrate speed: $U \leq 1$ m/s

Let L be the characteristic length in the direction of the substrate movement, as shown in figure 4.4. The local height h is determined according to the inset of figure 4.6. Then, the dimensionless variables are as follows,

$$t' = t\frac{U}{L}, x' = \frac{x}{L},\ z' = \frac{z}{h},\ u' = \frac{u}{U},\ w' = \frac{w}{\epsilon U},\ p' = \frac{\epsilon^2 L}{\mu U} p, \tag{4.1}$$

where ϵ is the aspect ratio h/L. The pressure is normalized by the viscous force and the aspect ratio. Substitution of equation 4.1 in the momentum equation for u yields:

$$\frac{\rho U^2}{L}\left(\frac{\partial u'}{\partial t'} + u'\frac{\partial u'}{\partial x'} + w'\frac{\partial u'}{\partial z'}\right) = -\frac{\mu U}{L^2 \cdot \epsilon^2}\frac{\partial p'}{\partial x'} + \frac{\mu U}{L^2}\left(\frac{\partial^2 u'}{\partial x'^2} + \frac{1}{\epsilon^2}\frac{\partial^2 u'}{\partial z'^2}\right), \tag{4.2}$$

Given that $h \ll L$, we have $\partial^2/\partial x^2 \ll \partial^2/\partial z^2$ in the viscous terms, and we further divide by $\mu U/L^2$, so that

$$Re \cdot \epsilon \left(\frac{\partial u'}{\partial t'} + u'\frac{\partial u'}{\partial x'} + w'\frac{\partial u'}{\partial z'}\right) \cong -\frac{\partial p'}{\partial x'} + \left(\frac{\partial^2 u'}{\partial z'^2}\right), \tag{4.3}$$

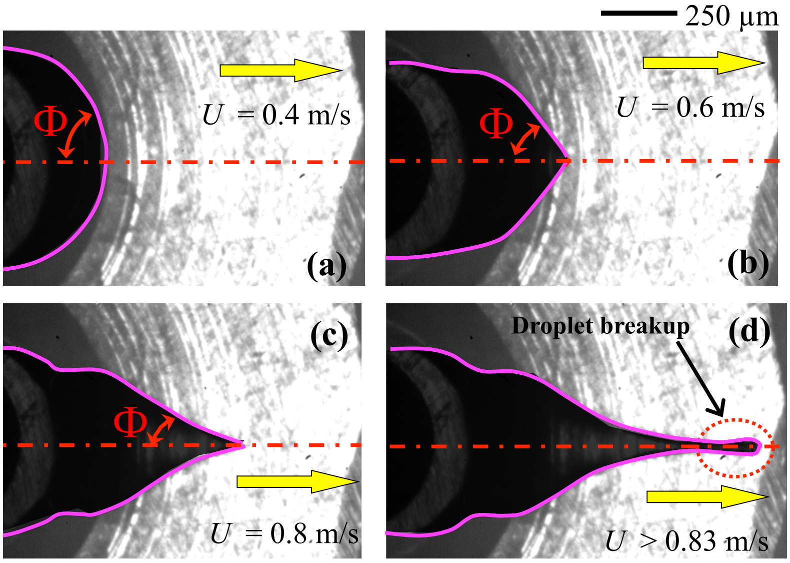

Figure 4.5: Evolution of the partial dewetting contact line (i.e. purple solid lines) by varying the speed of the substrate U where the height of the structure is 250 µm. Images observed from below by means of shadowgraphy. The dashed-dot line is the symmetry line of the partial dewetting and Φ is the half opening angle. (a) Oval shape, (b) corner shape, (c) corner to cusp shape, and (d) droplet breakup.

where Re is the instantaneous Reynolds number, $Re = \rho U h/\mu$. Here, $Re\cdot\epsilon$ is larger than unity as shown in figure 4.7. The inertia forces, i.e. the left hand side of equation 4.3, are thus not negligible in comparison with pressure and viscous forces.

In the same manner, in the wall normal direction, we find

$$\frac{\epsilon\rho U^2}{L}\left(\frac{\partial w'}{\partial t'}+u'\frac{\partial w'}{\partial x'}+w'\frac{\partial w'}{\partial z'}\right)=-\frac{\mu U}{\epsilon^2 Lh}\frac{\partial p'}{\partial z'}+\frac{\epsilon\mu U}{L^2}\left(\frac{\partial^2 w'}{\partial x'^2}+\frac{1}{\epsilon^2}\frac{\partial^2 w'}{\partial z'^2}\right). \tag{4.4}$$

where the viscous terms, $\partial^2/\partial x^2 \ll \partial^2/\partial z^2$, and we further divide $\epsilon\mu U/L^2$, so that

$$Re\cdot\epsilon^3\left(\frac{\partial w'}{\partial t'}+u'\frac{\partial w'}{\partial x'}+w'\frac{\partial w'}{\partial z'}\right)\cong-\frac{\partial p'}{\partial z'}+\epsilon^2\left(\frac{\partial^2 w'}{\partial z'^2}\right). \tag{4.5}$$

In this result, if the flow structure becomes very thin and long, i.e. $\epsilon \ll 1$, the pressure in the liquid is hydrostatic.

Figure 4.7 shows that in the observed flow $Re\cdot\epsilon$ is larger than unity. In particular, at the early stage, when the droplet has a oval shape at the rear part (see figure 4.5 (a)), $Re\cdot\epsilon$ increases with the substrate velocity. The aspect ratio is not small enough compared to

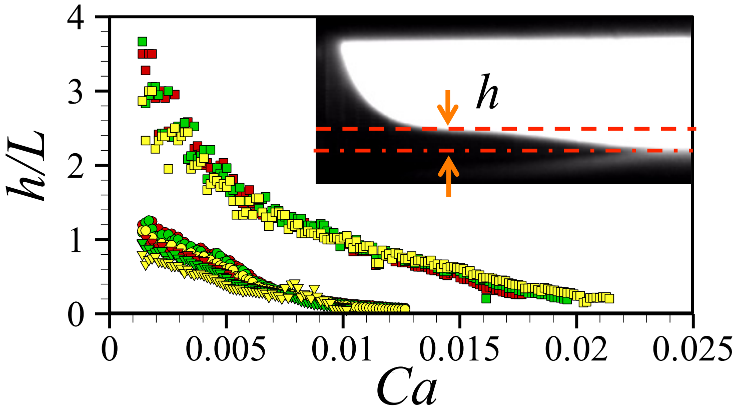

Figure 4.6: Evolution of the aspect ratio $\epsilon = h/L$ by varying the capillary number where the red symbol is for $H = 300$ μm; green, $H = 250$ μm; yellow, $H = 200$ μm above the different surface conditions, i.e., the □ symbol is $\theta_s = 89\pm8°$; ∘, $\theta_s = 76\pm8°$; and ∇, $\theta_s = 63\pm15°$ The dashed-dotted line indicates the substrate surface.

the Reynolds number (see figure 4.6). After the droplet assumes the corner shape, the flow structure begins to elongate further and then $Re\cdot\epsilon$ decreases. However, it remains large, i.e. $Re\cdot\epsilon > 1$.

Through further consideration of the scaling analysis, we obtain a result that describes the relation between θ and Φ and then we follow the analysis of (Limat and Stone, 2004). Let us consider the Navier-Stokes equations in the x- and z-direction. Then, in order to eliminate the pressure terms, we take the curl of the equations, which then yields:

$$\begin{aligned}&\frac{\partial}{\partial z}\left[\rho\left(\frac{\partial u}{\partial t}+u\frac{\partial u}{\partial x}+w\frac{\partial u}{\partial z}\right)\right]-\frac{\partial}{\partial x}\left[\rho\left(\frac{\partial w}{\partial t}+u\frac{\partial w}{\partial x}+w\frac{\partial w}{\partial z}\right)\right]\\&=\frac{\partial}{\partial z}\left[\mu\left(\frac{\partial^2 u}{\partial x^2}+\frac{\partial^2 u}{\partial y^2}+\frac{\partial^2 u}{\partial z^2}\right)\right]-\frac{\partial}{\partial x}\left[\mu\left(\frac{\partial^2 w}{\partial x^2}+\frac{\partial^2 w}{\partial y^2}+\frac{\partial^2 w}{\partial z^2}\right)\right].\end{aligned}\tag{4.6}$$

In a dimensionless form, using the scaling, defined in equation 4.1,

$$\begin{aligned}&\epsilon^2\left(\frac{\rho UL}{\mu}\right)\frac{\partial}{\partial z'}\left[\left(\frac{\partial u'}{\partial t'}+u'\frac{\partial u'}{\partial x'}+w'\frac{\partial u'}{\partial z'}\right)\right]-\epsilon^4\left(\frac{\rho UL}{\mu}\right)\frac{\partial}{\partial x'}\left[\left(\frac{\partial w'}{\partial t'}+u'\frac{\partial w'}{\partial x'}+w'\frac{\partial w'}{\partial z'}\right)\right]\\&\cong\left[\frac{\partial}{\partial z'}\left(\epsilon^2\frac{\partial^2 u'}{\partial x'^2}+\frac{\partial^2 u'}{\partial z'^2}\right)\right]-\epsilon^2\left[\frac{\partial}{\partial x'}\left(\epsilon^2\frac{\partial^2 w'}{\partial x'^2}+\frac{\partial^2 w'}{\partial z'^2}\right)\right],\end{aligned}\tag{4.7}$$

where $\epsilon^2(\rho UL/\mu) > \epsilon^4(\rho UL/\mu)$ on the left hand side and $1 > \epsilon^2$ on the right hand side. The

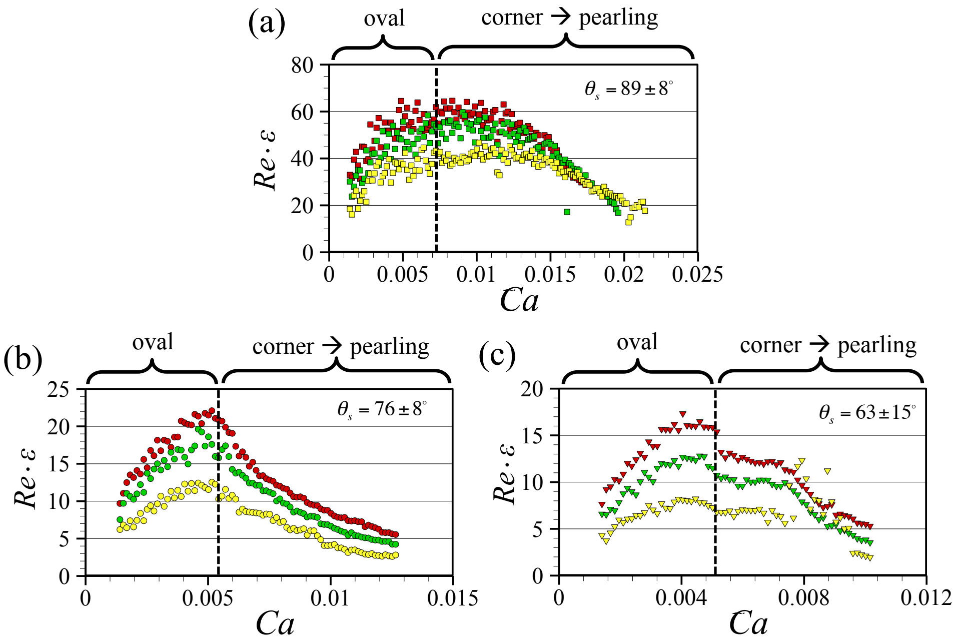

Figure 4.7: The evolution of $Re{\cdot}\epsilon$ with respect to the capillary number Ca. The red symbol notes for $H = 300$ µm; the green, $H = 250$ µm; the yellow, $H = 200$ µm above the different surface conditions, i.e., (a) $\theta_s = 89{\pm}8°$; (b) $\theta_s = 76{\pm}8°$; and (c) $\theta_s = 63{\pm}15°$.

result yields that the inertia forces are balanced with the viscous forces as follows:

$$\overbrace{\frac{\rho U L}{\mu}\epsilon^2}^{\text{inertia}} \sim \overbrace{1}^{\text{viscous}}. \tag{4.8}$$

According to figure 4.2 (b), the elongated tail length L can be described by the opening angle Φ and the radius of the liquid droplet R,

$$L \approx R\left(\sin\Phi^{-1} - 1\right). \tag{4.9}$$

Furthermore, if we assume that the aspect ratio (ϵ) can be written as $\tan\theta$, then equation 4.8 becomes,

$$L \approx R\left(\frac{1}{\sin\Phi} - 1\right) \sim \frac{\mu}{\rho U \tan^2\theta}. \tag{4.10}$$

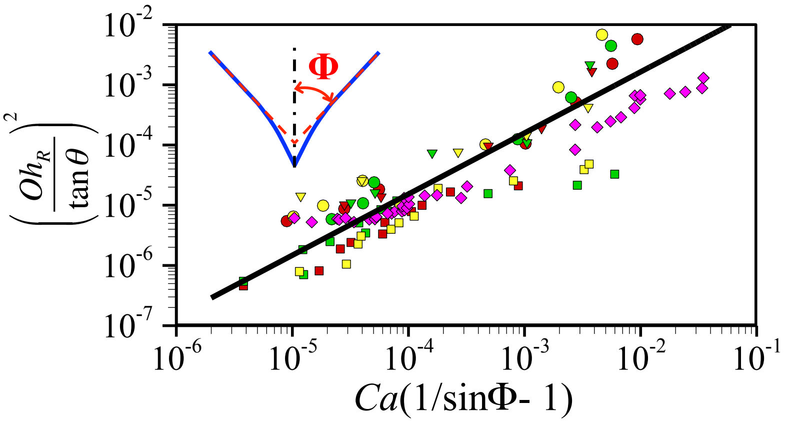

Figure 4.8: $(Oh_R/\tan\theta)^2$ $Vs.$ $Ca(1/\sin\Phi - 1)$ for three different substrates where the ∘ symbol is for $\theta_s = 76 \pm 8°$, the ∇ is for $\theta_s = 63 \pm 15°$, and □ and ⋄ symbols are for $\theta_s = 89 \pm 8°$. The red symbol ($R = 1$ mm) notes for $H = 300$ µm; the green ($R = 1$ mm) and purple ($R = 0.5$ mm), $H = 250$ µm; the yellow ($R = 1$ mm), $H = 200$ µm. The solid line represents linear fits to the measurement results.

This results in the following expression

$$\left(\frac{Oh_R}{\tan\theta}\right)^2 \cong \left[Ca \cdot \left(\frac{1}{\sin\Phi} - 1\right)\right], \tag{4.11}$$

where θ is the dynamic receding contact angle and Φ is the half opening angle. The Ohnesorge number Oh_R is $\mu/\sqrt{\rho\gamma R}$ where R is the radius of the immersion droplet. This dimensionless number describes the ratio of viscous forces to inertial and surface tension forces. We evaluate the equation 4.11 experimentally. The dynamic receding contact angle θ is determined from a fit to the liquid interface data within a distance of 50 µm from the corner tip of the droplet. We measure the half opening angle Φ as shown in the inset of figure 4.8. This result presents that dynamic receding contact angles and corner opening angles are correlated with each other according to the relation in equation 4.11.

4.3.2 Internal flow pattern

We obtain the 3D-3C flow field inside the liquid immersion droplet on the moving substrate at $U = 0.7$ m/s by means of Tomo-PIV, as shown in figure 4.9 (a). The obtained flow field contains 147 × 132 × 15 velocity vectors. The corner opening angle is $\Phi = 40°$. The external shape (i.e., the liquid-air interface) of the liquid immersion droplet is indicated in the white contour, i.e., where the velocity magnitude is zero. This was determined from the

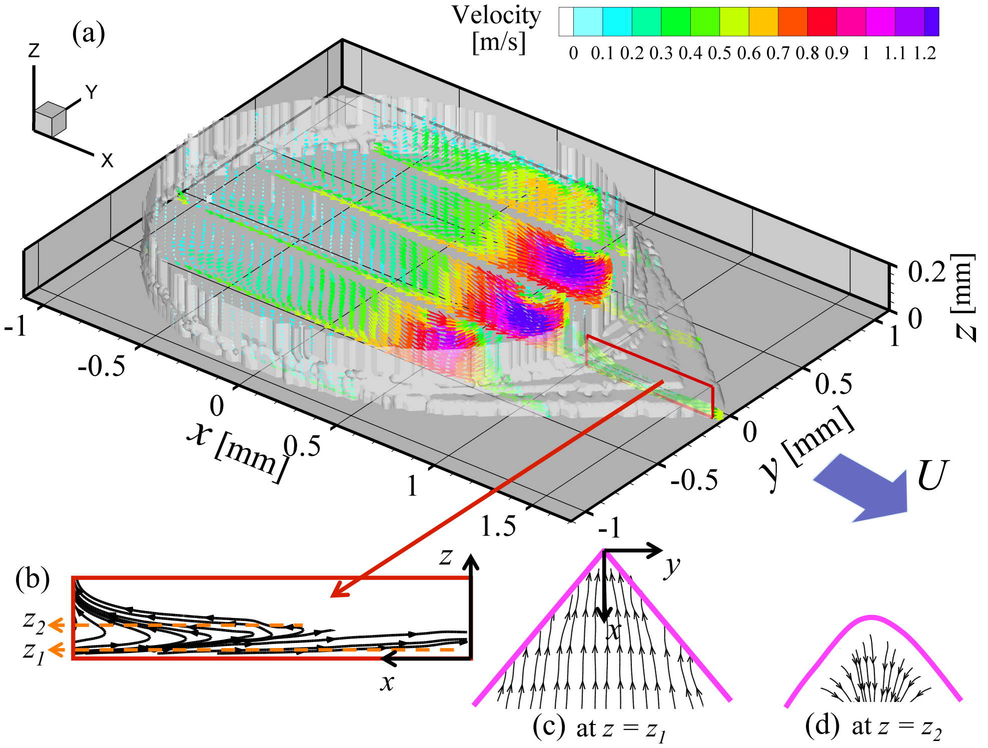

Figure 4.9: Full 3D-3C velocity distribution and streamlines in the liquid immersion droplet on the moving substrate ($U = 0.7$ m/s) at $Re = 140$ (a) 3D-3C velocity components at given arbitrary cross-sectional planes, where the white surface contour indicates the external shape of the liquid immersion droplet on the moving substrate. (b) The streamlines (the red box) at the cross-sectional plane (y = -0.04 mm). (c) In-plane streamlines at $z = 15$ µm. (d) In-plane streamlines at $z = 80$ µm.

reconstructed 3D tomographic images. We only plot velocity vector profiles at five arbitrary cross-sectional planes in figure 4.9 (a). The color of the vectors represents the velocity magnitude. The flow field is mainly driven by the moving substrate and the boundary conditions of the immersion needle (see figure 4.2(a)). Near the rear part of the outlet ($x =$ 0.75 mm), we observe the strong extraction flow field. Given the current experimental setup where the internal flow pattern is observed from below, it is difficult to obtain the velocity vectors at the advancing part where the contact angle is large. At the advancing part, only few data was obtained and the liquid-gas interface shape is difficult to reconstruct. In this study, we focus on the dewetting corner. Figure 4.9 (b) shows the streamline results at arbitrary cross-sectional plane ($y =$ -0.04 mm). Two in-plane streamlines at different z positions are plotted in figure 4.9 (c) and (d) where the purple solid lines indicate the contact lines. Note that streamlines at cross-sectional planes are more or less straight and parallel.

4.4 Model problem

4.4.1 Modified three-dimensional lubrication model for the dewetting corner

This section is devoted to a presentation of a three-dimensional lubrication model for the corner structure at $Re{\cdot}\epsilon > 1$. The model problem describes the rear part of the partial dewetting, as shown in figure 4.10 (a). The flow is governed by the incompressible Navier-Stokes equations and continuity equation,

$$\nabla \cdot \vec{u} = 0, \quad \rho \left[\frac{\partial \vec{u}}{\partial t} + (\vec{u} \cdot \nabla)\vec{u} \right] + \nabla p = \mu \nabla^2 \vec{u}, \tag{4.12}$$

where $\vec{u} = (u, v, w)$ and assuming that the gravity does not play a role in this problem. We use the vector identities, $(\vec{u} \cdot \nabla)\vec{u} \equiv \nabla \left(\frac{1}{2} \vec{u} \cdot \vec{u} \right) - \vec{u} \times \vec{\omega}$ and $\nabla^2 \vec{u} \equiv \nabla(\nabla \cdot \vec{u}) - \nabla \times (\nabla \times \vec{u})$ where $\vec{\omega} = (\omega_x, \omega_y, \omega_z) = \nabla \times \vec{u}$.

Let us first consider here a scaling analysis for the de-wetting flow problem at $Re \sim O(100)$, which will assist in deriving the extended lubrication model. The flow condition is representative of the flow in a liquid drop applied in a model of a liquid-immersion lithography machine, as sketched in the red-dashed box of figure 4.2 (a). The device generates a constant liquid volume over either a stagnant or a moving surface. For the model problem, we focus on the tail part of the de-wetting problem. If the substrate is moving with a speed U, then the de-wetting flow structure resembles a finite thin and long conical shape, as shown in figure 4.10 (a). For the scaling argument, we consider the following relevant length scales $x \sim L, y \sim W$, and $z \sim h$. By increasing the substrate speed up to 1 m/s, typical length scales are $L \sim 10^{-3}$ [m], $W \sim 10^{-4}$ [m], and $h \sim 10^{-5}$ [m], so $(h/W)^2$ and $(h/L)^2 \ll 1$. Furthermore, the stream-wise and span-wise velocities are dominant compared to the wall-normal component, $w \ll u, v$.

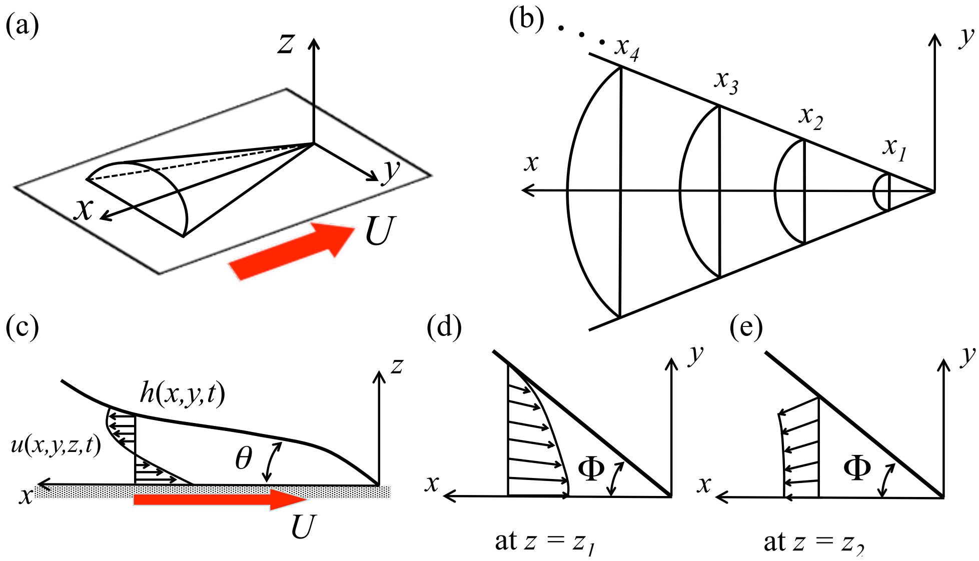

Figure 4.10: (a) Sketch of the partial dewetting contact line shapes observed for the moving substrate with a certain speed with respect to the droplet curvature. (b) Local cross-sectional plane at each x position. (c) Usual cross-sectional flow pattern near a contact line at $y = 0$. (d) Example of the planar flow field at $z = z_1$. (e) Another example of the planar flow field at $z = z_2$. Here, z_1 is at a plane where the flow is towards the tip of the tail and z_2 is at a plane where the flow is away from the tail.

In section 4.3.2, we presented the internal flow patterns in figure 4.9. At the de-wetting rear part of the droplet, we show that the flow patterns are approximately parallel between the free surface and the moving substrate. In this case, we can assume the cross-sectional flow structure as in figure 4.10 (c)-(e), i.e., the streamlines are straight and nearly parallel (see figure 4.9 (b)). This assumption implies $w \cong 0$ compared to (u, v). Then the pressure is independent of z, and is determined by the spanwise droplet curvature $p(x, y) = -\gamma \Delta h$ by the Young-Laplace equation, where the flow is assumed as incompressible, h describes the interface height, and $\Delta \equiv \partial^2/\partial x^2 + \partial^2/\partial y^2$ (Snoeijer et al., 2005).

By scaling arguments, the viscous terms are reduced to $\mu\left(\partial^2 \vec{u}/\partial z^2\right)$ where $\vec{u} = (u, v, 0)$. In this sense, the right hand side (viscous terms) of equation 4.12 should be the same as $\mu\left(\partial^2 \vec{u}/\partial z^2\right)$. For an incompressible flow, the continuity equation is satisfied, so that $\nabla \cdot \vec{u} = 0$. Then, the viscous terms are deduced to $-\nabla \times (\nabla \times \vec{u})$. This must be $\mu\left(\partial^2 \vec{u}/\partial z^2\right)$ by the scaling argument. To satisfy this condition, the z component of the vorticity ω_z is negligible compared to other vorticity components ω_x and ω_y (except for the region very close to the moving contact lines), which is validated by the experimental results (see figure 4.9). As a consequence, we can assume that the in-plane flow field is a simply two-dimensional flow pattern between interfaces. Then, we can assume that the normal component of vorticity ω_z is negligible compared with ω_x and ω_y.

Based on these assumptions ($w = 0$ and $\omega_z = 0$), the modified pressure is defined as $p^*(x,y){=}{-}\gamma\Delta h{+}\frac{1}{2}\rho q^2$ where $q = \|\vec{u}\|$ is the magnitude of the local fluid velocity. For the steady case the following modified governing equation, including dynamic pressure effects, can be formulated:

$$-\tilde{\nabla} p^* + \mu \frac{d^2\vec{u}}{dz^2} \cong 0, \tag{4.13}$$

where μ is the dynamic viscosity and $\tilde{\nabla} \equiv \left(\partial/\partial x, \partial/\partial y, 0\right)$. As a result, the viscous forces are balanced with the capillary pressure ($-\gamma\Delta h$) and the dynamic pressure ($\frac{1}{2}\rho q^2$).

In a contact line dynamics problem, the most important length scale is the capillary length, κ^{-1}. The capillary length can be determined by $(\Delta h)^{-1}$. Generally, it can be estimated by a force balance between the Laplace pressure $\gamma\kappa$ and the hydrostatic pressure $\rho g \kappa^{-1}$, i.e. $\kappa^{-1} = \sqrt{\gamma/\rho g}$. In equilibrium, the capillary length for water is normally about 3 mm, with a surface tension γ of 72 mN/m, a density ρ of 10^3 kg/m^3, and a gravitational acceleration $g = 9.8$ m/s^2. However, if it is not only driven by the gravity but also another force, then the capillary length needs to be modified. The capillary length can be re-defined as

$$\kappa^{-1} = \left(\frac{\gamma}{\rho g + \rho q^2/2\ell}\right)^{1/2}, \tag{4.14}$$

where $\rho g \kappa^{-1}$ and $\frac{1}{2}\rho q^2(\kappa^{-1}/\ell)$ are the hydrostatic pressure and dynamic pressure, respectively. ℓ is characteristic length scale and q^2 is the local velocity magnitude inside the flow field. For a raindroplet on a window, the characteristic length scale ℓ is O(1 mm) and the internal flow velocity q is O(1 cm/s) and then $\rho g \sim 10^4$ and $\rho q^2/2\ell \sim 10^2$. Therefore, the dynamic pressure effect can be neglected. So we retrieve the original expression for the capillary length (see above), $\kappa^{-1} \cong \sqrt{\gamma/\rho g}$. However, when the droplet speed reaches O(1 m/s), then $\rho q^2/2\ell \sim 10^6$ and $\rho g \sim 10^4$. As a result, the dynamic pressure effect becomes dominant. For negligible gravity, the capillary length is $\kappa^{-1} \cong \sqrt{2\gamma\ell/\rho q^2}$ (Biance et al., 2006; Reyssat et al., 2009).

In the dynamic situation of dewetting, the local free surface curvature (i.e. the inverse of the capillary length) varies with the x-position as shown in figure 4.10 (b). The curvature becomes large as one approaches the corner tip at $(x, y) = (0, 0)$ mm. To estimate the local curvature profile, we suggest that the local capillary length is described by

$$(\Delta h)^{-1} = \left(\frac{2h\gamma}{\rho q^2 \epsilon_x^2}\right)^{1/2}, \tag{4.15}$$

where ℓ is defined as h/ϵ_x^2 where considering the flow geometry. h is the local height of the partial dewetting flow and ϵ_x is the local aspect ratio h/x. As a consequence, the dynamic pressure can be expressed in terms of the dynamic capillary length, $\frac{1}{2}\rho q^2 = \gamma\ell(\Delta h)^2$.

From this equation, we have $q^2 \sim x(\Delta h)^2/\tan\theta$. The curvature (Δh) increases as one approaches to the corner tip, i.e. $x \to 0$, where $\tan\theta$ $(=h/x)$ is constant. Then, we assume that the local fluid velocity magnitude is independent of the x-position, i.e. constant. This hypothesis is validated by the experimental and theoretical results in section 4.4.3.

To obtain the velocity profile, the boundary conditions are given as the no slip boundary condition at the wall and the stress free condition at the free surface. The velocity profile is then obtained by substituting equation 4.15 into equation 4.13 for the dynamic pressure and integrating the equation in the z direction:

$$\vec{u} = \frac{1}{2\mu}\tilde{\nabla}\left(-\gamma\Delta h + \frac{\gamma x^2}{h}(\Delta h)^2\right)\left(z^2 - 2hz\right) - U, \tag{4.16}$$

where U is the substrate speed and $h(x,y)$ is the free surface profile. The velocity profile is described as a combination of Poiseuille flow and Couette flow.

The modified total pressure consists of the capillary pressure and the dynamic pressure, so that equation 4.13 can be expressed as

$$\tilde{\nabla}\left(\underbrace{-\gamma\Delta h}_{\text{capillary pressure}} + \overbrace{\frac{\gamma x^2}{h}(\Delta h)^2}^{\text{dynamic pressure}} \right) - \underbrace{\frac{3\mu\mathbf{U}}{h^2}}_{\text{viscous force}} = 0, \tag{4.17}$$

where $\mathbf{U}$ is the 2D depth-averaged velocity profile in a coordinate system relative to the moving substrate, $\mathbf{U}(x,y) = \frac{1}{h}\int_0^h dz\,\vec{u}$. If the surface tension is constant, then equation 4.17 can be re-written as

$$\tilde{\nabla}\Delta h - \frac{3\mu\mathbf{U}}{\gamma h^2}\left[1 + \overbrace{\frac{\gamma h^2}{3\mu\mathbf{U}}\tilde{\nabla}\left(\frac{x^2}{h}(\Delta h)^2\right)}^{\text{dynamic pressure effect}}\right] = 0. \tag{4.18}$$

This result is similar to the classical lubrication equation, but now accounting for the dynamic pressure. For a sliding droplet in the Stokes regime, the lubrication model is $\tilde{\nabla}\Delta h = 3\mu\mathbf{U}/\gamma h^2$ (Limat and Stone, 2004). The conventional lubrication theory model can be modified for the dynamic pressure, provided that the flow pattern at the corner has straight and nearly parallel streamlines.

4.4.2 Modified interface equation $H(\zeta)$ for dewetting corner

Recently, Limat and Stone (2004); Stone et al. (2002) presented the interface equation $H(y/x)$ to describe the three dimensional corner structure using a similarity solution $h(x,y) = Ca^{1/3}xH(y/x)$ where $Ca = \mu U/\gamma$ is the capillary number. The final equation is a nonlinear 4th-order ordinary differential equation that was validated using experimental data. Although it is limited to the Stokes flow regime and the small receding contact angle, the model is useful to understand the shape transition mechanism of partial dewetting contact lines.

In this section, we extend the lubrication model to $Re{\cdot}\epsilon > 1$ for the case of a flow pattern with straight and nearly parallel streamlines. To obtain the interface equation $h(x,y)$, equation 4.17 should satisfy the depth-averaged mass conservation and if the interface is considered in a reference frame moving with the droplet, then

$$\frac{\partial h}{\partial t} + \nabla\cdot(h\mathbf{U}) = 0, \tag{4.19}$$

where $h(x-Ut,y)$ describes the partial dewetting interface in the moving reference frame. Then, we substitute **U** from equation 4.17 into equation 4.19 and then we obtain a result for the interface $h(x,y)$,

$$3\mathrm{Ca}\frac{\partial h}{\partial x} = \nabla\cdot\left[h^3\nabla\left(\Delta h - \frac{x^2}{h}(\Delta h)^2\right)\right]. \tag{4.20}$$

This is the modified three-dimensional corner structure equation at $Re{\cdot}\epsilon > 1$. Then, if we adopt the similarity Ansatz $h(x,y) = Ca^{1/3}xH(\zeta)$ where $\zeta = y/x$ (Limat and Stone, 2004), then the result yields

$$\begin{aligned}
&3(H-\zeta H_\zeta) = (1+\zeta^2)^2(H^3H_{\zeta\zeta\zeta})_\zeta + 3\zeta(1+\zeta^2)(H^3H_{\zeta\zeta})_\zeta + 2\zeta(1+\zeta^2)H^3H_{\zeta\zeta\zeta}\\
&+(1+3\zeta^2)H^3H_{\zeta\zeta} - [(1+\zeta^2)^3(-HH_\zeta H_{\zeta\zeta}^2 + 2H^2H_{\zeta\zeta}H_{\zeta\zeta\zeta})_\zeta +\\
&4\zeta(1+\zeta^2)^2(4HH_{\zeta\zeta\zeta} + H_\zeta H_{\zeta\zeta})HH_{\zeta\zeta} + 2\zeta(1+\zeta^2)^2(HH_{\zeta\zeta\zeta} + H_\zeta H_{\zeta\zeta})HH_{\zeta\zeta}\\
&+3(1+5\zeta^2)(1+\zeta^2)H^2H_{\zeta\zeta}^2],
\end{aligned} \tag{4.21}$$

where $H(\zeta)$ is independent of the capillary number and the Reynolds number. The derivative of $H(\zeta)$ with respect to ζ is written as H_ζ.

The partial dewetting corner structure $H(\zeta)$ is described by a 4th-order ordinary differential equation. To solve this equation, two boundary conditions are $H_\zeta(0) = H_{\zeta\zeta\zeta}(0) = 0$ because of the symmetry. Further, there are two independent parameters $H(0) = H_0$ and $H_{\zeta\zeta}(0)$. However, each H_0 has several $H(0)_{\zeta\zeta}$ solutions (Limat and Stone, 2004). To choose the proper value for $H(0)_{\zeta\zeta}$, Limat and Stone (2004) suggested that when the curvature $H(\zeta)$ obeys the mass conservation, there is a unique $H_{\zeta\zeta}(0)$ for each H_0. As shown in figure 4.11, for equation 4.21, each H_0 also has several $H(0)_{\zeta\zeta}$. To find out the matching solution, the x-flux integrated over a cross-sectional plane must be zero. This statement can be expressed as

$$F(\zeta) = \int_0^\zeta \left[H^3\left(\left[\zeta[1+\zeta^2]H_{\zeta\zeta} - \frac{H_{\zeta\zeta}^2}{H}\left[1+\zeta^2\right]^2\zeta\right]_\zeta + \frac{3}{H^2}\right)\right]d\zeta = 0, \tag{4.22}$$

where the flux is integrated between $y = -\zeta x$ and $y = \zeta x$. This integrated equation can be derived in the same manner as mentioned in the literature (Limat and Stone, 2004). As

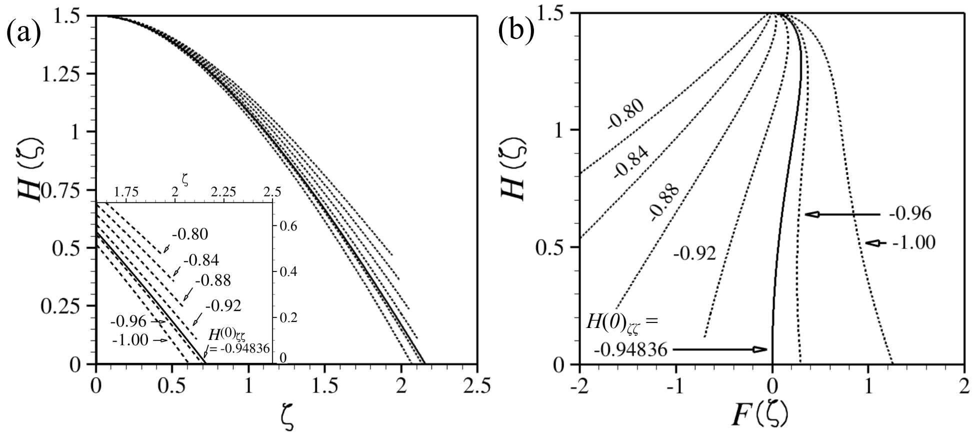

Figure 4.11: Solutions of the interface $H(\zeta)$ equation. (a) $H(\zeta)\ Vs.\ \zeta$; different solutions of equation 4.21 with $H(0) = 1.5$ by different initial $H(0)_{\zeta\zeta}$. The solid line is the exact solution to satisfy equation 4.22 (b) $H(\zeta)\ Vs.\ F(\zeta)$ shows that there is only one pair $H(0)$ and $H(0)_{\zeta\zeta}$ to satisfy the mass conservation.

shown in figure 4.11 (b), each $H(0)$ has a unique $H_{\zeta\zeta}(0)$ solution that satisfies $F(\zeta) \to 0$ and $H(\zeta) \to 0$. In this problem, the solution is $H(0)_{\zeta\zeta}$ = -0.94836 for $H_0 = 1.5$. To obtain the proper $H_{\zeta\zeta}(0)$, we use the shooting method with a 4th-order Runge-Kutta method.

We numerically solve equation 4.21 and plot the results as the solid line in figure 4.12, which is the relationship between the corner angle Φ and $H_0 (= Ca^{-1/3} \tan\theta)$. This prediction is validated using experimental data. We measure two angles, Φ and θ, and then we plot all measurement results of the present partial dewetting problem in figure 4.12. The dashed-dot-line is the numerical result for the gravity-driven droplet on an inclined plane, which was investigated by Limat and Stone (2004); Snoeijer et al. (2005). They used the classical lubrication approximation ignoring convective acceleration (inertial) terms. Our model (i.e. solid-line) provides a better prediction for the relation between Φ and H_0 as the corner angle becomes smaller, i.e. at large substrate speeds.

Limat and Stone (2004) assumed that the cross-sectional plane of the conical shape can be approximated by a parabolic shape, i.e. $h(x, y) \approx H_0 Ca^{1/3} x[1 - y^2/(x^2 \tan^2\phi)]$. We use this same assumption to describe the shape of the partial dewetting flow at $Re \sim O(100)$. From equation 4.17, we obtain the approximate analytical solution,

$$\tan^3\theta \approx \overbrace{\frac{3}{2} Ca \tan^2\Phi}^{\text{capillary pressure}} + \overbrace{\frac{3}{4} Ca \tan^4\Phi}^{\text{dynamic pressure}} . \tag{4.23}$$

Figure 4.13 shows that when $\Phi < 60°$, $3/4Ca \cdot \tan^4\Phi$ becomes dominant. In contrast, when

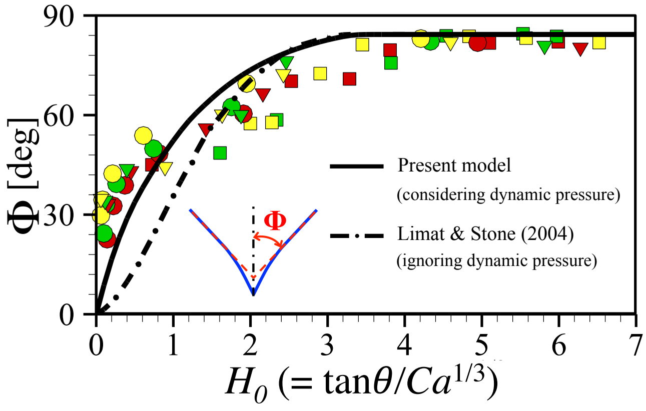

Figure 4.12: Comparison of numerical results for the relation between corner angles Φ and tan$\theta/Ca^{1/3}$. The solid line has been obtained numerically from equations 4.21 and 4.22. The dashed-dot-line is the numerical result of Limat and Stone (2004) that is based on the Stokes flow regime. The symbols are experimental data on this partial dewetting flow probelm for three different surface conditions and colors indicate the different drop volumes. The red symbol notes for $H = 300$ µm; the green, $H = 250$ µm; the yellow, $H = 200$ µm where the radius of droplets is $R = 1$ mm.

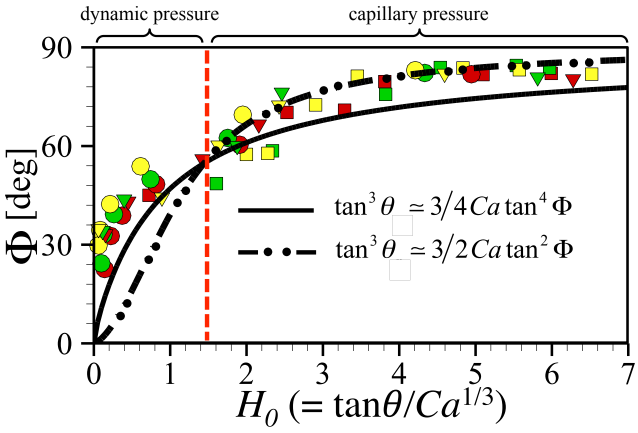

Figure 4.13: Approximate analytical solutions for the relation between the corner angle Φ and tan$\theta/Ca^{1/3}$. The solid line is $\tan^3\theta \approx 3/4$ Ca $\tan^4\Phi$ for $30° < \Phi < 60°$ and the dashed double-dot line is $\tan^3\theta \approx 3/2$ Ca $\tan^2\Phi$ for $\Phi > 60°$. The symbols are experimental data for three different surface conditions and colors indicate the different drop volumes. The red symbol notes for $H = 300$ µm; the green, $H = 250$ µm; the yellow, $H = 200$ µm where the radius of droplets is $R = 1$ mm.

the angle Φ is larger than about 60°, $3/2Ca \cdot \tan^2\Phi$ term is dominant. Hence, we can postulate that there are two approximate solutions to describe the relationship between θ and Φ. In the present partial dewetting flow at $Re \sim O(100)$, the dynamic pressure effects become important when the corner opening angle is getting smaller.

4.4.3 Self-similar flow pattern at $Re \sim O(100)$

Based on the present lubrication model, we can obtain the two-dimensional mean velocity profile at the corner structure. From equation 4.17, we express the 2D mean velocity profile in a coordinate system relative to the moving substrate:

$$\mathbf{U}(x,y) = \frac{\gamma h^2}{3\mu}\left(\tilde{\nabla}\Delta h - \tilde{\nabla}\left[\frac{x^2}{h}(\Delta h)^2\right]\right). \tag{4.24}$$

By the similarity Ansatz $h(x,y) = Ca^{1/3}xH(\zeta)$, we can obtain the velocity profile in a polar coordinate system (r,ϕ):

$$\begin{aligned} U_r &= \overbrace{-\frac{U}{3}\frac{H^2H_{\zeta\zeta}}{\cos\phi}}^{\text{capillary pressure}} + \overbrace{\frac{U}{3}\frac{HH_{\zeta\zeta}^2}{\cos^3\phi}}^{\text{dynamic pressure}}, \\ U_\phi &= \underbrace{\frac{U}{3}\frac{H^2}{\cos^3\phi}\left(H_{\zeta\zeta\zeta} + \frac{3}{2}H_{\zeta\zeta}\sin2\phi\right)}_{\text{capillary pressure}} \\ &\quad - \underbrace{\frac{U}{3}\frac{HH_{\zeta\zeta}}{\cos^5\phi}\left(-\frac{H_\zeta H_{\zeta\zeta}}{H} + 2H_{\zeta\zeta\zeta} + \frac{5}{2}H_{\zeta\zeta}\sin2\phi\right)}_{\text{dynamic pressure}}, \end{aligned} \tag{4.25}$$

where $x = r \cos \phi$; $y = r \sin \phi$. We use the (r, ϕ) coordinates to indicate the local position (r) from the corner tip and the angle (ϕ) within the corner shape, where $-\Phi \leq \phi \leq \Phi$. The derivative of $H(\zeta)$ with respect to ζ is written as H_ζ.

To validate this result, we compare this solution with the measurement results obtained with Tomo-PIV. We measure the volumetric flow field at the rear part of two partial dewetting droplets where the half opening angles are $\Phi = 40°$ and 75°. The experiments are performed in the same manner as in a previous study (Kim et al., 2011). The obtained flow field contains 179 × 133 ×15 velocity vectors for $\Phi = 75°$ and 147 × 132 × 15 velocity vectors for $\Phi = 40°$, as shown in figure 4.14. In figure 4.14 (a) and (b), each symbol indicates a different slice with respect to the corner tip $(x,y) = (0,0)$ mm of the partial dewetting flow where each slice is separated by 50 μm. To compare the measurement results with analytical results we have plotted the depth-averaged radial velocity U_r and angular velocity U_ϕ results as a function of the position ϕ in figure 4.14 (c) and (d). The red solid and dashed lines indicate the analytical results, which are U_r and U_ϕ, respectively.

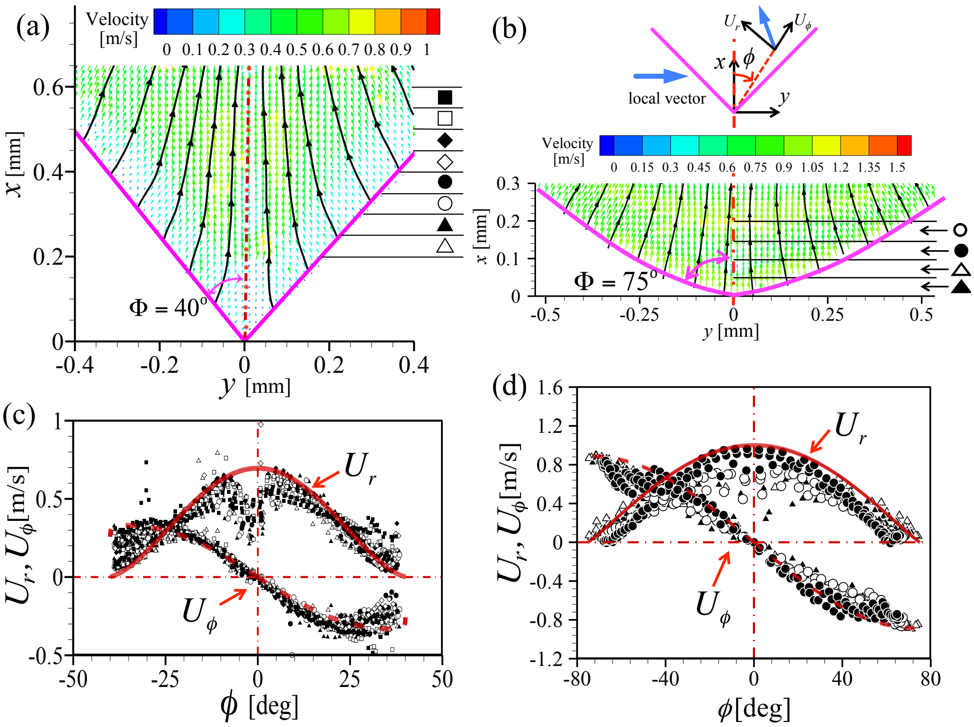

Figure 4.14: Comparison of Tomo-PIV results and the analytical solution: The depth-averaged velocity vectors (colors) and streamlines (black) of the partial dewetting flow where the vectors are the apparent velocities in the moving frame of coordinates where the half opening angles are (a) $\Phi = 40°$ and (b) $\Phi = 75°$. Self-similar flow pattern: U_r (red-solid) and U_ϕ (red-dashed) indicate the radial and angular velocity components, respectively, (c) $\Phi = 40°$ and (d) $\Phi = 75°$ We have divided the data into slices of $\Delta x = 50$ µm distance each from the corner of the drop. The center of the droplet is the red dashed-dot line and the purple solid lines indicate the contact lines.

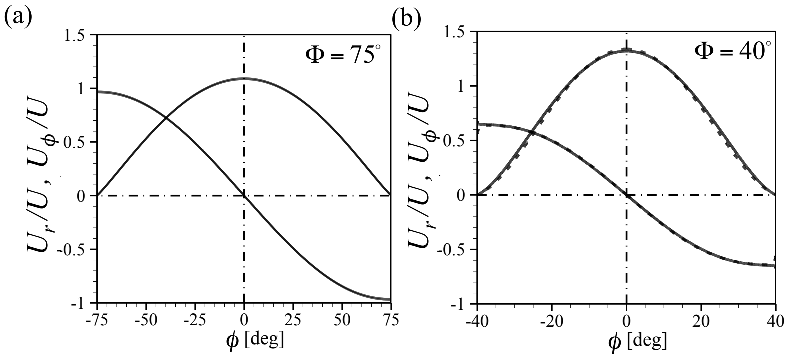

Figure 4.15: Comparison of analytical velocity profiles for (a) $\Phi = 75°$ and (b) $\Phi = 40°$. The solid-line is the analytical solution based on the Stokes flow by Snoeijer et al. (2005) and the dashed-line is for equation 4.25 based on the modified lubrication theory.

During the PIV measurement, there are some particles that attach to the moving substrate. To obtain the velocity vector, the cross-correlation of the recorded particle distribution at the two exposures is performed. The particles that remain on the substrate can bias the local velocity measurements at off-wall positions. In particular, this results in a higher data scatter near the contact lines ($\phi = 40°$) and along the corner tip of the droplet ($\phi = 0$), as shown in figure 4.14 (c). Nevertheless, our measurement results are in a good agreement with the analytical results. The analytical and experimental results show that the velocity components are independent of the distance from the corner tip, which is indicative of a self-similar flow pattern.

In fact, Snoeijer et al. (2005) first showed the self-similar flow pattern in the corner structure at $Re \ll 1$. Interestingly, this similarity occurs over a wide range of Reynolds numbers, i.e. a droplet sliding down an incline ($Re \ll 1$) and a liquid immersion droplet ($Re \sim O(100)$). If the dynamic pressure is neglected in equation 4.25, then the velocity expressions are same as the result of Snoeijer et al. (2005). For $\Phi = 40°$ and 75°, we compare the analytical velocity profiles for both problems as shown in figure 4.15 where the velocity components are normalized by the relative droplet velocity, U. Surprisingly enough, both solutions are more or less identical, although the differential equations are not identical, $cf.$ equation 4.21 and equation (8) by Limat and Stone (2004) and equation (10) by Snoeijer et al. (2005). In the case of $\Phi = 75°$, two different solutions are exactly same and U_r and U_ϕ profiles collapse as shown in 4.15 (a). In the case of $\Phi = 40°$, the velocity profiles are slightly different but not much.

As shown in figure 4.15, both results show that the velocity profiles are independent of the local distance. In particular, the radial velocity component U_r becomes zero close to the contact line and the angular velocity shows $U_\phi \cong -U{\cdot}\sin\Phi$. To interpret the difference

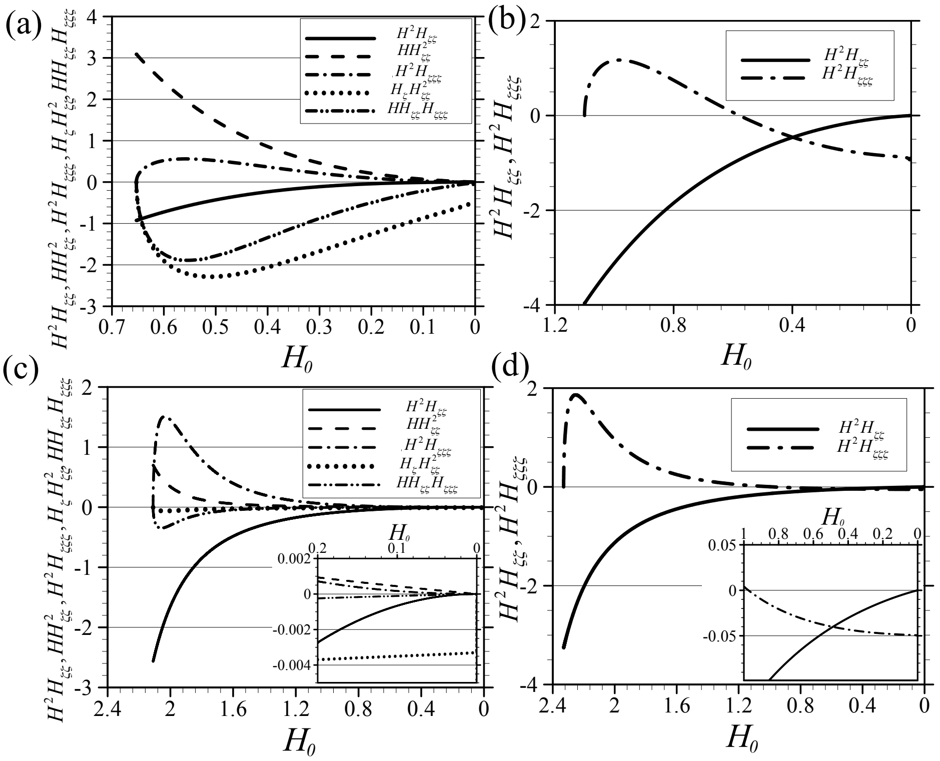

Figure 4.16: Derivative term profiles in the velocity profiles. (a) and (b) are for $\Phi = 40°$ and (c) and (d) are for $\Phi = 75°$. The corner velocity profile including the inertia effect is (a) and (c). At the contact lines ($H_0 = 0$), $H_\zeta H_{\zeta\zeta}^2$ has a non-zero finite value. On the other hand, the corner velocity profile in the Stokes flow regime is (b) and (d). At the contact lines ($H_0 = 0$), $H^2 H_{\zeta\zeta\zeta}$ has a non-zero finite value.

in the two analytical solutions, we plot the profile of each derivative term of equation 4.25 of this paper and equation (13) of Snoeijer et al. (2005) in figure 4.16. If $H(0)$ approaches 0, it means $\phi \to \Phi$. Contrarily, when $H(0) = H_0$, i.e. the center line of the partial dewetting flow, $\phi \to 0$. For the problem in the Stokes flow regime, $H^2 H_{\zeta\zeta} \to 0$ as $H \to 0$. At the contact line, the $H^2 H_{\zeta\zeta\zeta}$ term determines the angular velocity U_ϕ and then $U_\phi = UH^2 H_{\zeta\zeta\zeta}/3\cos^3\Phi$. On the other hand, in the case of the problem considering dynamic pressure effects, except for $H_\zeta H_{\zeta\zeta}^2$, all the terms vanish at the contact line. Therefore, for the angular velocity component U_ϕ at the contact line, $U_\phi = -UH_\zeta H_{\zeta\zeta}^2/3\cos^5\Phi$. This result can also be obtained from equation 4.21. If ζ approaches the contact line, $\zeta \to \tan\Phi$, equation 4.21 is dominated by the highest order of ζ. Hence, equation 4.21 reduces to:

$$-3(\tan\Phi)H_\zeta \cong -(1+\tan^2\Phi)^3\left(-HH_\zeta H_{\zeta\zeta}^2 + 2H^2 H_{\zeta\zeta} H_{\zeta\zeta\zeta}\right)_\zeta, \qquad (4.26)$$

where $\zeta \to \tan\Phi$, and we integrate this with respect to ζ once, so that

$$3\cdot\sin\Phi\cdot\cos^5\Phi = -H_\zeta H_{\zeta\zeta}^2 + 2HH_{\zeta\zeta}H_{\zeta\zeta\zeta} + \frac{C}{H}, \qquad (4.27)$$

where C is the integration constant, which is zero to prevent the divergence of the equation where $H \to 0$. Furthermore, $HH_{\zeta\zeta}H_{\zeta\zeta\zeta} \to 0$ and $H_\zeta H_{\zeta\zeta}^2$ has a finite value, when $H \to 0$. Then, we have $\sin\Phi = -H_\zeta H_{\zeta\zeta}^2/(3\cdot\cos^5\Phi)$ at the contact line. From the analytical velocity profile, we show that the angular velocity at the contact line ($H \to 0$) is $U_\phi = -UH_\zeta H_{\zeta\zeta}^2/3\cos^5\Phi$. Thus, we obtain the same result $U_\phi \cong -U\cdot\sin\Phi$, as shown in figure 4.15. After all, although the value to determine the velocity profile is different, the result shows a self-similar flow pattern when the rear shape of the droplet has a corner. Moreover, the interesting result is that the flow pattern is determined by the interface equation $H(\zeta)$, i.e. the shape of the droplet tail.

4.5 Discussion and conclusion

In this chapter, we study the partial dewetting flow problem at intermediate Reynolds number. We observe the evolution of the dewetting contact lines, i.e. from oval to corner, wedge, and pearling droplets, which is similar to that of the gravity-driven droplet on an incline. The lubrication theory is not suitable for the present problem, because of $Re\cdot\epsilon > 1$. However, based on the flow pattern analysis and scaling analysis, we obtain a modified pressure that consists of the capillary pressure and the dynamic pressure. Then, the governing equation becomes a linear equation although $Re \gg 1$ and $Re\cdot\epsilon > 1$. To apply the modified lubrication theory, the key requirement is that the streamlines are straight and nearly parallel.

Limat and Stone (2004); Snoeijer et al. (2005); Stone et al. (2002) first studied the three-dimensional lubrication model for the dewetting corner at $Re \ll 1$. In this case, it is assumed that the flow is entirely driven by gradients of the transverse curvature, which is determined by the relation between the viscous force and the capillary force. Due to the low Reynolds number, the convective acceleration terms are simply neglected. The opening angle Φ for the droplet tail predicted by the conventional model (see the inset of figure 2 of Limat and Stone (2004) and figure 5 of Snoeijer et al. (2005)) deviates significantly from experimental data when the contact line speed increases, i.e high Ca and small θ. The theoretical model underestimates the half corner opening angle. In particular, around $H_0 = 1.5$, the difference of the theoretical prediction and measurement results increases. This value for H_0 is the same as the one determined from the approximate analytical solution by our model (see figure 4.13). We show that there are two solutions $\tan^3\theta \approx \frac{3}{4}Ca \tan^4\Phi$ for $\Phi < 60°$ (dynamic pressure is dominant) and $\tan^3\theta \approx \frac{3}{2}Ca \tan^2\Phi$ for $60° < \Phi$ (capillary pressure is dominant).

Here, in the dewetting corner flow, we assume that streamlines are more or less straight and nearly parallel at cross-sectional planes. In the x-y plane, fluid elements are deformed and accelerated along the streamlines due to the converging flow (Faber, 1995). In the case of the gravity-driven droplet, the flow velocity is approximately a few mm/s to a few cm/s whereas in the present investigation the flow velocity is of the order of 1 m/s. Except where the velocity is relatively small compared to the present problem (the immersion droplet), the typical flow pattern is almost the same, as shown in figure 4.15. Furthermore, at the contact line, the angular velocity is also identical, i.e. $U_\phi \cong -U\cdot\sin\Phi$. When the dewetting corner shape occurs, the flow acceleration and viscous stress may be taken into account at the same time. Likewise, Hancock et al. (1981); Moffatt (1964) pointed out that inertia becomes significant at a certain distance from the corner although the flow is in the Stokes regime. As a consequence, we presume that the inertia forces may begin to play a role when the corner shape at the dewetting contact lines appears. A further investigation is recommended.

The similarity solution $h(x,y) = Ca^{1/3}xH(\zeta)$ is still useful in this problem although this similarity solution is limited to the conical geometry case. In reality, the partial dewetting flow structure has a more complicated interface and therefore the three-dimensional corner interface equation needs to be studied further and must be improved. Furthermore, the given similarity solution is expressed as the capillary number and the flow structure aspect ratio. It is believed that a further examination with the methods outlined is worthwhile to find a new similarity solution. In addition, to interpret the effects of inertia, the results must be described by a different parameter that includes the inertia forces.

4.6 Acknowledgments

We would like to thank L. van Bokhoven and K. in de Braekt for a help in the shadowgraphy experiment performed at ASML Holding NV.

4.7 Bibliography

R. J. Adrian and J. Westerweel. *Particle Image Velocimetry*. Cambridge University Press., 2010.

A. L. Biance et al. On the elasticity of an inertial liquid shock. *J FLUID MECH*, **554**, 47, 2006.

T. D. Blake. The physics of moving wetting lines. *J COLLOID INTERF SCI*, **299**, 1, 2006.

T. D. Blake, J. De Coninck and U. d'Ortona. Models of wetting: immiscible lattice boltzmann automata versus molecular kinetic theory. *LANGMUIR*, **11**, 4588, 1995.

T. D. Blake and Y. D. Shikhmurzaev. Dynamic wetting by liquids of different viscosity. *J COLLOID INTERF SCI*, **253**, 196, 2002.

D. Bonn et al. Wetting and spreading. *REV MOD PHYS*, **81**, 739, 2009.

A. J. Briant and J. M. Yeomans. Lattice Boltzmann simulations of contact line motion. II. Binary fluids. *PHYS REV E*, **69**, 031603, 2004.

F. Brochard-Wyart and P. G. De Gennes. Dynamics of partial wetting. *ADV COLLOID INTERFAC*, **39**, 1, 1992.

J. Eggers and R. Evans. Comment on "dynamic wetting by liquids of different viscosity," by TD blake and YD shikhmurzaev. *J COLLOID INTERF SCI*, **280**, 537, 2004.

G. E. Elsinga. *Tomographic particle image velocimetry and its application to turbulent boundary layers*. Ph.D. thesis, Delft University of Technology, 2008.

T. E. Faber. *Fluid dynamics for physicists*. Cambridge Univ. Press, 1995.

P. G. Gennes. Wetting: statics and dynamics. *REV MOD PHYS*, **57**, 827, 1985.

F. Gentner, G. Ogonowski and J. De Coninck. Forced wetting dynamics: a molecular dynamics study. *LANGMUIR*, **19**, 3996, 2003.

C. Hancock, E. Lewis and H. K. Moffatt. Effects of inertia in forced corner flows. *J FLUID MECH*, **112**, 315, 1981.

C. Huh and L. E. Scriven. Hydrodynamic model of steady movement of a solid/liquid/fluid contact line. *J COLLOID INTERF SCI*, **35**, 85, 1971.

H. Kim, J. Westerweel and G. E. Elsinga. Comparison of Tomo-PIV and 3D-PTV for microfluidic flows. *revised, MEAS SCI TECHNOL*, 2012.

H. Kim et al. Full 3D-3C velocity measurement inside a liquid immersion droplet. *EXP FLUIDS*, **51**, 395, 2011.

L. Limat and H. A. Stone. Three-dimensional lubrication model of a contact line corner singularity. *EUROPHYS LETT*, **65**, 365, 2004.

G. C. H. Mo, W. Liu and D. Y. Kwok. Surface-ascension of discrete liquid drops via experimental reactive wetting and lattice boltzmann simulation. *LANGMUIR*, **21**, 5777, 2005.

H. K. Moffatt. Viscous and resistive eddies near a sharp corner. *J FLUID MECH*, **18**, 1, 1964.

J. Mulkens et al. Benefits and limitations of immersion lithography. *J MICROLITH MICROFAB*, **3**, 104, 2004.

S. Owa and H. Nagasaka. Immersion lithography: its history, current status and future prospects. In *P SPIE*, volume 7140, 714015, 2008.

T. Podgorski, J. M. Flesselles and L. Limat. Corners, cusps, and pearls in running drops. *PHYS REV LETT*, **87**, 36102, 2001.

O. Reynolds. On the theory of lubrication and its application to mr. beauchamp tower's experiments, including an experimental determination of the viscosity of olive oil. *P R SOC LONDON*, **40**, 191, 1886.

M. Reyssat, F. Pardo and D. Quéré. Drops onto gradients of texture. *EUROPHYS LETT*, **87**, 36003, 2009.

M. Riepen, F. Evangelista and S. Donders. Contact line dynamics in immersion lithography-dynamic contact angle analysis. In *Proc. 1st Euro. Conf. Microfluidics*, 2008.

J. H. Snoeijer et al. Self-similar flow and contact line geometry at the rear of cornered drops. *PHYS FLUIDS*, **17**, 072101, 2005.

H. A. Stone et al. Singularité anguleuse d'une ligne de contact en mouvement sur un substrat solide. *C R PHYS*, **3**, 103, 2002.

F. M. White. *Viscous Fluid Flow*. McGraw-Hill, 2005.

B. Wieneke. Volume self-calibration for 3D particle image velocimetry. *EXP FLUIDS*, **45**, 549, 2008.

CHAPTER 5

NUMERICS: SIMPLIFIED DROPLET MODELS[1]

Abstract

A simplified numerical model has been developed for a liquid immersion droplet. We study a partially dewetting flow problem at a Reynolds number of the order of 100. This problem corresponds to the flow in an immersion drop applied in a liquid-immersion lithography machine. For the numerical computation domain, we adopt a flat cylinder. We apply a zero flux boundary condition at the gas-liquid interface. The numerical results are compared with measurement results and give a good agreement.

5.1 Introduction

In an immersion lithography machine, a confined liquid layer (i.e. a liquid immersion droplet) is generated by an immersion hood. The hood is supposed to keep a constant liquid volume between a lithography lens and a silicon wafer during semiconductor production. When the substrate (wafer) reaches a critical velocity, the liquid droplet begins to lose mass (liquid) behind the main immersion droplet. The droplets that remain on the substrate cause a defect on the wafer (French and Tran, 2009). Therefore, it is important to prevent droplet breakup during the operation. To improve performance, a partially dewetting flow problem at relatively high Reynolds numbers is studied (Kim et al., 2011, 2012; Riepen et al., 2008; Winkels et al., 2011). Furthermore, Harder (2007) pointed out the importance of designing an immersion hood.

---

[1] The content of this chapter was presented at Physics@FOM Veldhoven 2012 (Kim et al. 2012c).

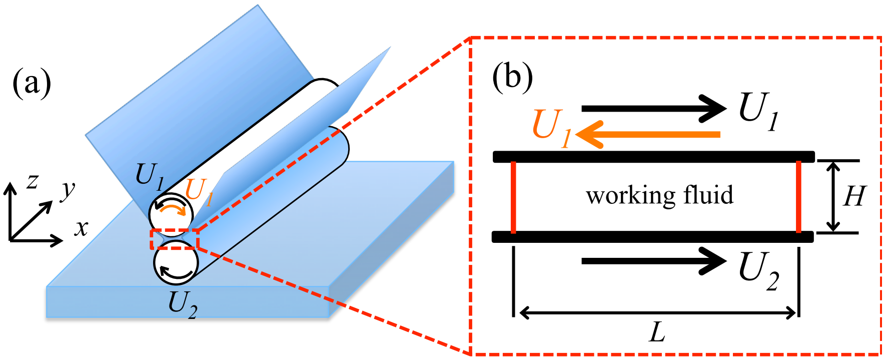

Figure 5.1: A simplified example: (a) schematic of a meniscus roll coating system and (b) a simplified zero flux model for the flow in between rollers. The red-solid lines indicate the zero flux boundary. Gaskell et al.'s model is summarized in this figure.

It is evident that to understand the flow field a direct flow measurement is the best method. In preceding chapters, we performed tomographic particle image velocimetry (referred to as Tomo-PIV), which is able to obtain three-dimensional three-component (referred to as 3D-3C) velocity vectors in a volume. However, this technique is used to measure a specific flow geometry. The immersion droplet stability is related to many variables (e.g. fluid, the drop height, the contact angle, the inlet and outlet boundary condition, and so on). It is therefore difficult and laborious to perform the 3D-3C velocimetry method for every single case. Hence, it is desirable to investigate the internal flow pattern in a different way.

To further investigate the liquid immersion droplet, we hereby introduce a simplified numerical model, the so-called zero flux model (Canedo and Denson, 1989; Gaskell et al., 1995, 1998). The model was previously used in an open cavity problem where the flow was driven by a side moving wall (Canedo and Denson, 1989). Later on, Gaskell et al. (1995, 1998) also used a similar approach to simplify the model for a meniscus roll coater, as shown in figure 5.1. The boundary condition for a free surface is treated as a zero flux surface. The numerical study was performed for the flow in a double-lid-driven cavity with free surface side walls. They showed a good agreement between the numerical and the experimental results. Furthermore, they found out the overall diagram for the flow bifurcation by varying the aspect ratio (H/L) and the speed ratio (U_1/U_2) at top and bottom walls.

In this chapter, we perform a numerical computation for the simplified immersion droplet model. We assume that the liquid droplet shape is a flat cylinder (see figure 5.2(b)). A zero flux boundary condition is applied for the gas-liquid interface (Canedo and Denson, 1989; Gaskell et al., 1995, 1998). For the inlet and outlet, the boundary conditions are

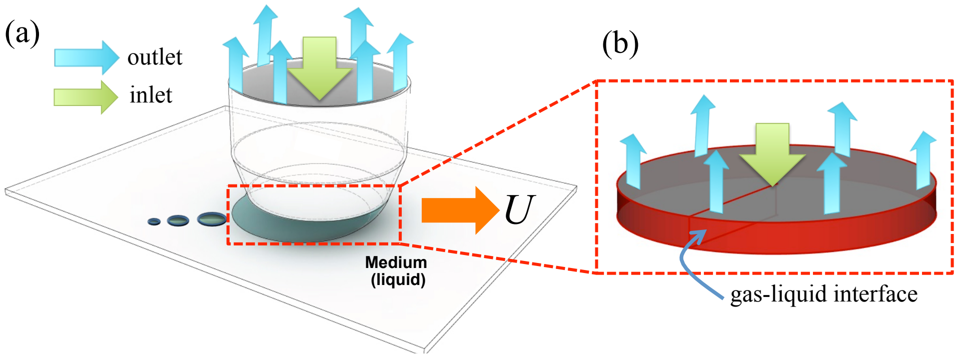

Figure 5.2: Model problem: (a) a sketch of the liquid immersion droplet. (b) a simplified 3D computation model where the red area (side) is treated as the zero flux boundary. The green and blue arrows indicate inlet and outlet, respectively.

applied that are based on the practical condition as shown in figure 5.3(c). At the bottom, a moving boundary condition is applied. The numerical results are compared with the Tomo-PIV results. We show that both results are in a good agreement.

5.2 Model problem

Consider a zero flux model in an liquid immersion droplet on a moving substrate with a velocity U, as shown in figure 5.2. The present problem (see figure 5.2(a)) is simplified as a cylindrical computation domain, as shown in figure 5.2(b). The domain has a 200 µm height (thickness) and 2 mm diameter (width). A moving boundary condition is applied to the bottom. At the top of the droplet, the inlet and outlet boundary conditions are applied as shown in figure 5.3(c). The water is supplied at the center of the immersion hood device. Around the inlet, there is a outlet. In this study, we do not consider moving contact lines. At 3-phase point, the contact lines are fixed. The side wall (i.e. the gas-liquid interface) of the droplet are not deformed. Furthermore, the free surface is treated as a zero flux boundary condition.

Let us consider the governing equations that describe a fluid motion in a confined liquid droplet (a liquid immersion droplet). The continuity equation expresses the mass conservation for the incompressible flow:

$$\frac{1}{r}\frac{\partial}{\partial r}(r u_r)+\frac{1}{r}\frac{\partial u_\phi}{\partial \phi}+\frac{\partial u_z}{\partial z}=0. \tag{5.1}$$

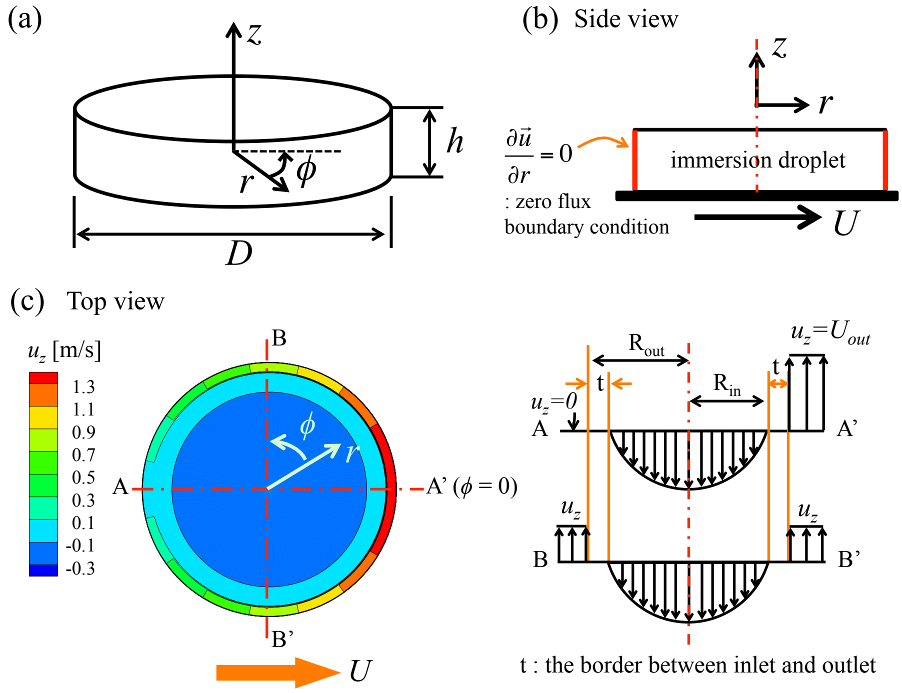
(a)
z
h
r
ϕ
D
(b) Side view
z
r
$\frac{\partial \vec{u}}{\partial r} = 0$
: zero flux
boundary condition
immersion droplet
U
(c) Top view
u_z [m/s]
1.3
1.1
0.9
0.7
0.5
0.3
0.1
-0.1
-0.3
B
A
A' ($\phi = 0$)
B'
ϕ
r
U
$u_z=U_{out}$
R$_{out}$
R$_{in}$
t
t
$u_z=0$
A
A'
u_z
u_z
B
B'
t : the border between inlet and outlet

Figure 5.3: Sketch of the simplified model and the boundary conditions. (a) A numerical computation domain of a flat cylinder. (b) Side view: a moving boundary at the bottom and a zero flux boundary condition at the gas-liquid interface (the red-solid lines). (c) Top view: inlet and outlet conditions are applied that are based on the practical flow condition. At the inlet ($r \leq \mathrm{R_{in}}$), Poiseuille flow is applied. The droplet is dragged by the moving substrate (see figure 2.12(a)) and therefore flow pattern is skewed toward the rear part of the droplet. Hence, the outlet profiles are applied as shown in figure 5.3(c).

The incompressible Navier-Stokes equations, i.e. the conservation of momentum, are:

$$\rho\left(\frac{\partial u_r}{\partial t}+u_r\frac{\partial u_r}{\partial r}+\frac{u_\phi}{r}\frac{\partial u_r}{\partial \phi}+u_z\frac{\partial u_r}{\partial z}-\frac{u_\phi^2}{r}\right)$$
$$=-\frac{\partial p}{\partial r}+\mu\left[\frac{1}{r}\frac{\partial}{\partial r}\left(r\frac{\partial u_r}{\partial r}\right)+\frac{1}{r^2}\frac{\partial^2 u_r}{\partial \phi^2}+\frac{\partial^2 u_r}{\partial z^2}-\frac{u_r}{r^2}-\frac{2}{r^2}\frac{\partial u_\phi}{\partial \phi}\right], \tag{5.2}$$

$$\rho\left(\frac{\partial u_\phi}{\partial t}+u_r\frac{\partial u_\phi}{\partial r}+\frac{u_\phi}{r}\frac{\partial u_\phi}{\partial \phi}+u_z\frac{\partial u_\phi}{\partial z}+\frac{u_r u_\phi}{r}\right)$$
$$=-\frac{1}{r}\frac{\partial p}{\partial \phi}+\mu\left[\frac{1}{r}\frac{\partial}{\partial r}\left(r\frac{\partial u_\phi}{\partial r}\right)+\frac{1}{r^2}\frac{\partial^2 u_\phi}{\partial \phi^2}+\frac{\partial^2 u_\phi}{\partial z^2}-\frac{u_\phi}{r^2}+\frac{2}{r^2}\frac{\partial u_r}{\partial \phi}\right], \tag{5.3}$$

$$\rho\left(\frac{\partial u_z}{\partial t}+u_r\frac{\partial u_z}{\partial r}+\frac{u_\phi}{r}\frac{\partial u_z}{\partial \phi}+u_z\frac{\partial u_z}{\partial z}\right)$$
$$=-\frac{\partial p}{\partial z}+\mu\left[\frac{1}{r}\frac{\partial}{\partial r}\left(r\frac{\partial u_z}{\partial r}\right)+\frac{1}{r^2}\frac{\partial^2 u_z}{\partial \phi^2}+\frac{\partial^2 u_z}{\partial z^2}\right], \tag{5.4}$$

where $(u_r,\ u_\phi,\ u_z)$ is the velocity component in the $(r,\ \phi,\ z)$ domain (see figure 5.3(a)); p, pressure. The fluid physical properties are the density $\rho = 10^3$ kg/m^3 and the dynamic viscosity $\mu = 10^{-3}$ Pa·s. We assume that gravity is negligible. We solve the dimensional equations.

From the problem description of figure 5.3(b) and (c), the boundary conditions are given as follows:

At the liquid interface $(r = R)$,

$$\frac{\partial u_r}{\partial r}=0, \tag{6.5(a)}$$

where a zero flux condition is considered at the interface.

At the bottom $(z = 0)$,

$$u_r = U\cos\phi, u_\phi = U\sin\phi, u_z = 0, \quad \text{where} \quad 0 \le \phi \le 2\pi, \tag{6.5(b)}$$

where U is the substrate velocity.

At the top $(z = h)$, for the inlet and the rim boundary,

$$u_r = u_\phi = 0, u_z(=u_{in}) = -2U_{mean}\left[1-\left(\frac{r}{R_{in}}\right)^2\right], \qquad \text{for} \quad r \le R_{in}; \tag{6.5(c)}$$

$$u_r = u_\phi = u_z = 0, \qquad \text{for} \quad R_{in} < r < R_{out}. \tag{6.5(d)}$$

Here, R_{in} and R_{out} positions are indicated in figure 5.3(c). U_{mean} is an average velocity of Poiseuille flow at inlet where $U_{mean} = 0.1$ m/s.

At the top $(z = h)$, for the outlet $(R_{out} \le r \le R)$,

$$u_r = u_\phi = 0, u_z(=u_{out}) = U_{out}\left|1-\frac{\phi}{\pi}\right|, \quad \text{for} \quad 0 \le \phi \le 2\pi. \tag{6.5(e)}$$

As the substrate velocity increases, the droplet is dragged by the moving substrate and then the droplet tail is elongated. (see figure 2.2 (b) and (c)). Furthermore, The droplet is tilted to the substrate moving direction and the outflow volume at the rear part of the outlet is larger than that at the advancing part, as shown in figure 2.12(a). Therefore, the outflow volume can be assumed linearly decreasing to the advancing outlet part. Therefore, we assume the outflow rate is zero at $\phi = \pi$ and at the rear part of the droplet ($\phi = 0$ or 2π) the outflow velocity is U_{out}, as shown in 5.3(c). The velocity U_{out} is determined by considering the mass conservation at $z = h$, i.e. $\int_A u_z \,|_{z=h}\, \mathrm{d}A = 0$ or $\int_{A_{in}} u_{in} \,|_{z=h}\, \mathrm{d}A_{in} = \int_{A_{out}} u_{out} \,|_{z=h}\, \mathrm{d}A_{out}$, where A is the total area; A_{in}, the inlet area; and A_{out}, the outlet area.

We use the cylindrical LES (Large-Eddy-Simulation) code developed by J.G.M. Eggels and M.J.B.M. Pourquie (Brethouwer et al., 1999; Eggels et al., 1994). A finite volume method is used to discretize the governing equations. A uniform staggered grid is used in this problem. The advection terms are discretized using second order accurate central differences. The time-stepping is done using the leap-frog method (central differences in time) for the advective terms and Euler-forward for the diffusive terms in the r- and z-direction. In the ϕ-direction, the equations are solved implicitly, with the Crank-Nicholson scheme for the advective terms and Euler-Backward for the diffusive terms. For all computations, a $(128 \times 96 \times 48)$ grid network was employed in the (r, ϕ, z) domain, respectively. In our problem, the typical Reynolds is $O(100)$ and therefore we assume there is no turbulence. We found that the flow became stationary after some time, and consider only the final, stationary state in this study.

5.3 Results and discussion

The internal flow pattern of a liquid immersion droplet is numerically obtained by a simplified zero flux model. In this section, we evaluate the numerical model by comparing with the flow measurement result.

Figure 5.4 and 5.5 show streamlines results obtained by the Tomo-PIV and the simplified numerical model. For the numerical model, we assume that the liquid-gas interface (at $r = R$) is not deformable, so that a flow field near the interface could not be exactly resolved. However, except for the tail region (the green-zone of figure 5.4 and 5.5), the qualitative flow patterns are in a good agreement between two results. At the advancing part, we observe a stagnation point in both cases, as shown in figure 5.4. In the measurement results (see figure 2.12(a) and figure 5.4(a)), there are only few velocity vectors at the top of the advancing part of a liquid droplet due to the experimental limitation, i.e. non-uniform refractive indexes (see chapter 2.4.2). Hence, at the advancing part, the flow pattern obtained by Tomo-PIV is not very reliable but we can approximately identify a stagnation point from figure 5.4(a).

By using this simplified model, we investigate several internal flow patterns by varying the substrate velocity. We plot u- and w-velocity profiles at the advancing ($\phi = \pi$) and the receding ($\phi = 0$) part of the cross-sectional plane, as shown in figure 5.6. Figure 5.6(b) shows that a stagnation point at the advancing part is moving downward (close to the substrate) by increasing the substrate velocity while keeping a constant boundary condition at the inlet and outlet. At the receding part, for increasing substrate velocities, the gradient of the wall-normal velocity varies as shown in figure 5.6 (d).

The liquid immersion droplet should be kept as uniform as possible during operation. During semiconductor production, the main immersion droplet may lose mass (i.e. droplet breakup) when the dewetting part of the flow becomes unstable or the velocity of the dewetting contact line reaches a critical condition. The droplets that remain on the silicon

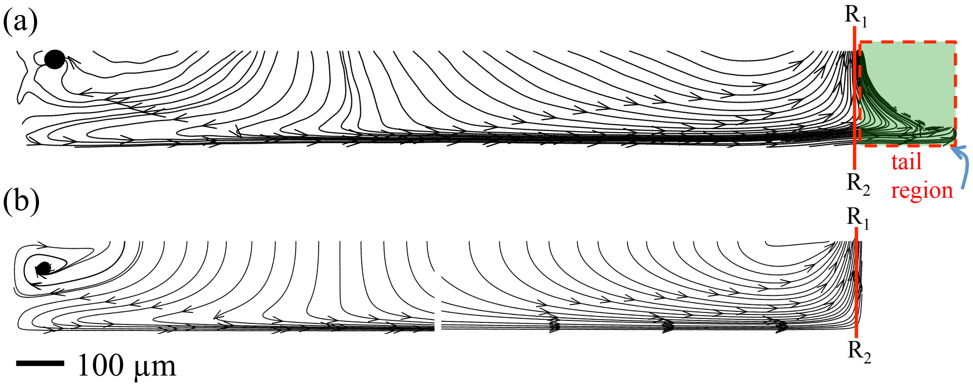

Figure 5.4: Side view comparison of streamlines at the cross-sectional plane from (a) Tomo-PIV ($y = 0$) and (b) the zero flux model (A–A') where the substrate velocity is $U = 1$ m/s. The green zone indicates the tail region.

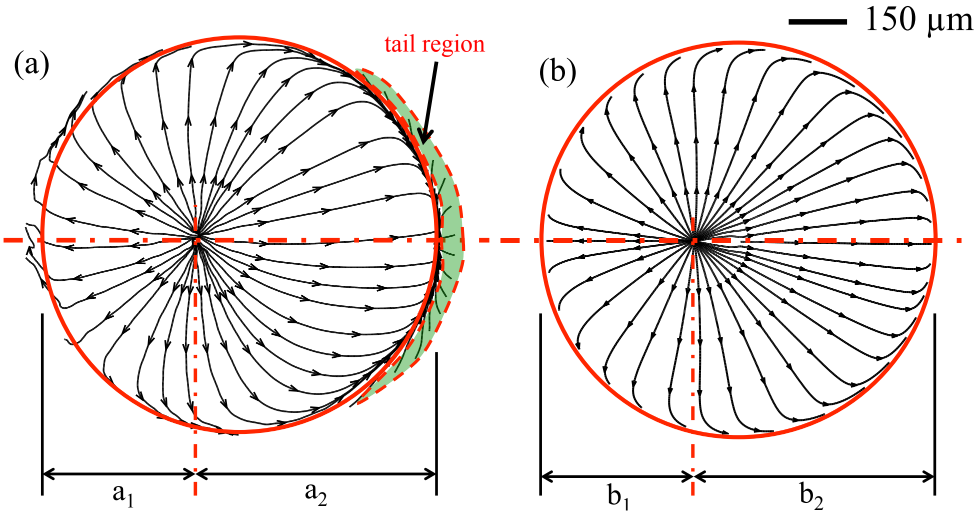

Figure 5.5: Top view comparison of streamlines at the cross-sectional plane at $z = 100$ µm from (a) Tomo-PIV and (b) the zero flux model where the substrate velocity is $U = 1$ m/s. The green zone of Tomo-PIV indicates the tail region. Except for the green zone, flow patterns are similar and the source point of the flow at the cross-sectional plane is located at the same relative position, $a_1/a_2 = b_1/b_2$.

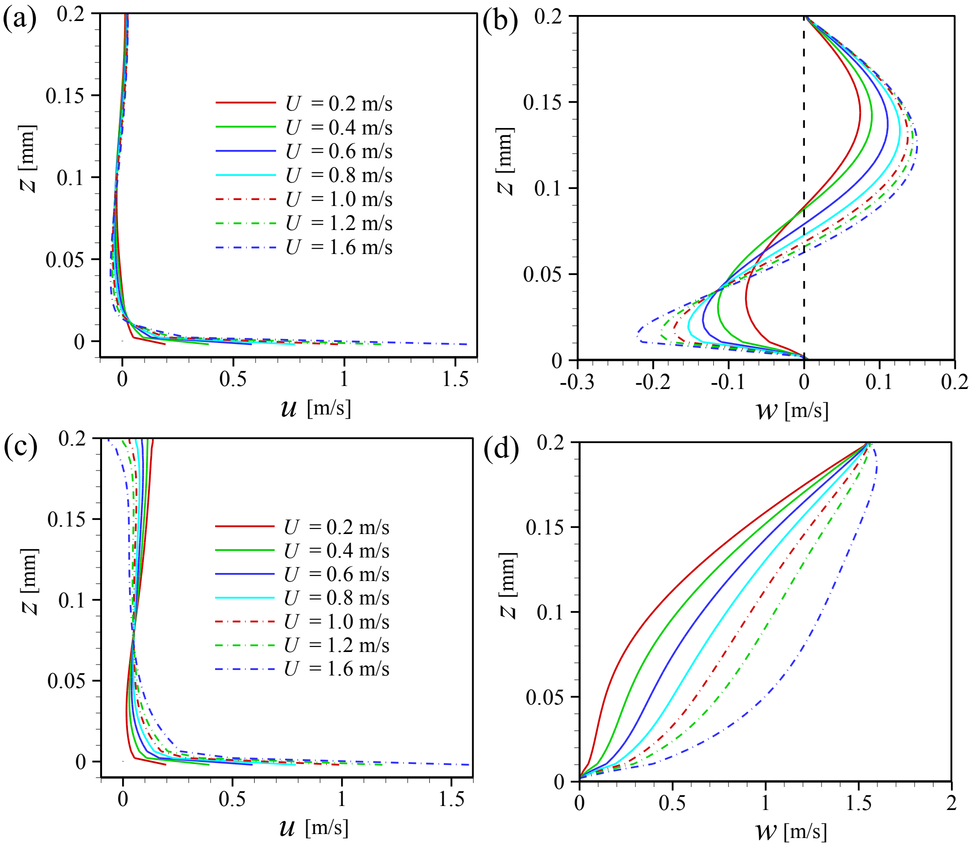

Figure 5.6: Comparison of u- and w-velocity profiles for various substrate velocities U. (a) and (b) are at the advancing part (at $\phi = \pi$). (c) and (d) are at the receding part (at $\phi = 0$ or 2π).

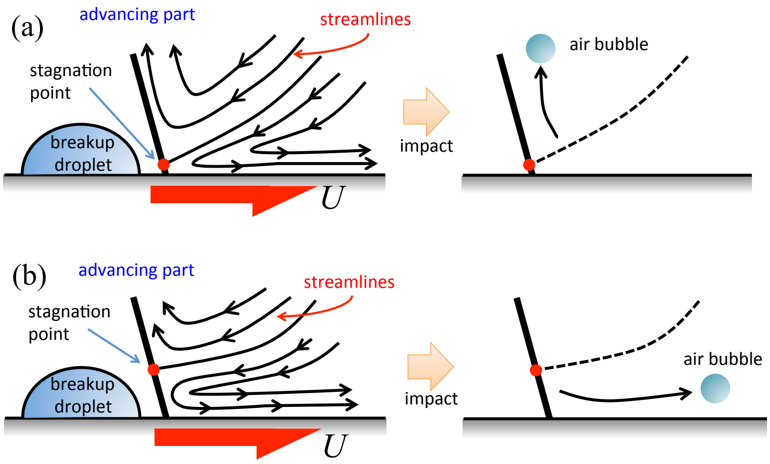

Figure 5.7: Cartoon for a bubble entrapment and travel when the liquid immersion droplet merges with a breakup droplet remained on the substrate. (a) a low stagnation point and (b) a high stagnation point.

wafer can merge with the main immersion droplet again while the hood moves randomly. Then, an air bubble can be entrapped when two liquid interfaces impact each other (Hasan and Prosperetti, 1990). The gas bubbles inside the immersion droplet may cause defects due to its different refractive index (see figure 1.6). The position of the stagnation point at the advancing part is significant to the trajectory of the entrapped-bubble inside the immersion droplet, as described in figure 5.7. If the stagnation point at the leading part of the immersion droplet is close to the substrate, the air bubble can move upward (see figure 5.7(a)). On the other hand, if the stagnation point is rather high, the bubble can travel along the substrate (see figure 5.7(b)). The stagnation point can be changed by changing the boundary conditions, e.g. the substrate velocity, the boundary conditions at inlet and outlet, and so on.

For the receding part, the numerical model could not obtain the flow pattern at the tail region of the liquid droplet due to the fixed geometry shape. Nevertheless, figure 5.4 and 5.5 show that the flow patterns are approximately similar between the PIV measurement and the numerical result. In particular, the flow fields of the bulk region (see the red-circle of figure 5.5) are in a good agreement. Figure 5.8 shows comparison of the streamwise and the wall-normal velocity profiles that are extracted from the R_1–R_2 line of figure 5.4. Both the experimental and numerical velocity profiles are similar but there is some disparity between two results. The difference can be due to the inflexible gas-liquid interface.

From this result, for the case of a simplified immersion hood device, we could postulate that the liquid immersion drop can be largely divided into a bulk region and a tail region,

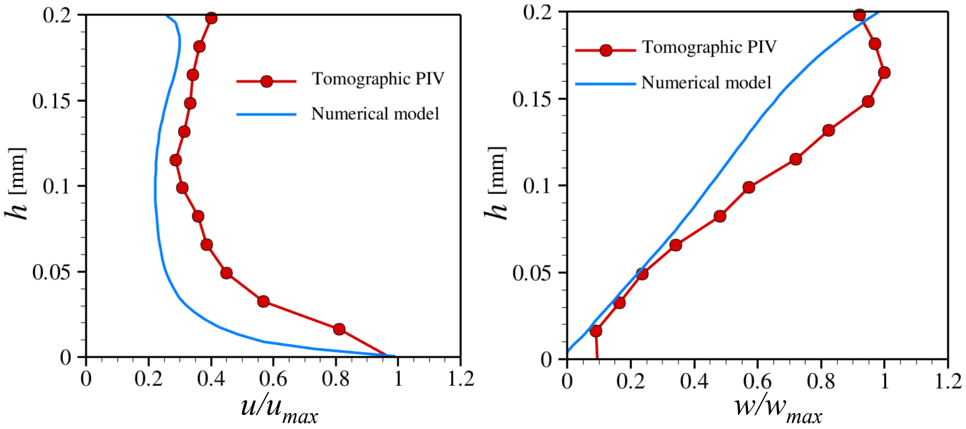

Figure 5.8: Comparison of velocity profiles at $R_1 - R_2$ of figure 5.4 by the Tomo-PIV and the numerical model.

as shown in figure 5.4 and 5.5. In this sense, we can study this liquid immersion droplet by separating a bulk and a tail region. For the tail region, we can use the modified lubrication model (see chapter 4). The simplified numerical model can be used for the bulk region.

5.4 Conclusion

The simplified numerical model for a liquid droplet over a moving substrate is introduced in this chapter. We use the zero flux boundary condition for the gas-liquid interface. We assume the liquid interface does not deform and hence the model can not provide the flow pattern for the tail region. However, the numerical result of the bulk region qualitatively is in a good agreement with the tomographic PIV result.

Furthermore, by using the simplified numerical model, we report that a stagnation point at the advancing part is moving downward when increases the substrate velocity. We address that the stagnation point is relevant for the travel route of an entrapped bubble inside the immersion droplet. Besides, a location of bubble generation can be important to determine the bubble travel route inside the immersion droplet. The impact position between two liquid interfaces (the breakup droplet left on the substrate and the main immersion droplet) is related to the size of the breakup droplet and the curvature of the leading edge of the main immersion drop. To validate this hypothesis, it is required to perform a further study, for instance an investigation into the bubble trajectory for various substrate velocities or the impact position of two liquid interfaces.

To control contact lines during wetting and dewetting, the most feasible tuning parameter can be an immersion hood design that is able to effectively change the internal flow pattern. The flow patterns are mainly governed by the inlet & outlet boundary conditions and the substrate velocity at the bottom. We believe that, to examine internal flow patterns, this simplified numerical model could be used in an effective way to test different designs of the immersion hood.

5.5 Acknowledgement

We would like to thank M.J.B.M. Pourquie who helped us to use the LES numerical code.

5.6 Bibliography

G. Brethouwer et al. Direct numerical simulation of turbulent mixing of a passive scalar in pipe flow. *EUR J MECH B-FLUID*, **18**, 739, 1999.

E. Canedo and C. D. Denson. Flow in driven cavities with a free surface. *AICHE J*, **35**, 129, 1989.

J. Eggels et al. Fully developed turbulent pipe flow: a comparison between direct numerical simulation and experiment. *J FLUID MECH*, **268**, 175, 1994.

R. French and H. Tran. Immersion lithography: photomask and wafer-level materials. *ANNU REV MATER RES*, **39**, 93, 2009.

P. H. Gaskell et al. Modelling and analysis of meniscus roll coating. *J FLUID MECH*, **298**, 113, 1995.

P. H. Gaskell et al. Stokes flow in a double-lid-driven cavity with free surface side walls. *P I MECH ENG C-J MEC*, **212**, 387, 1998.

P. M. Harder. *Physical and thermal behaviors of dynamic three-phase contact lines.* University of Wisconsin–Madison, 2007.

O. Hasan and A. Prosperetti. Bubble entrainment by the impact of drops on liquid surfaces. *J FLUID MECH*, **1219**, 143, 1990.

H. Kim et al. Full 3D-3C velocity measurement inside a liquid immersion droplet. *EXP FLUIDS*, **51**, 395, 2011.

H. Kim et al. Experimental and theoretical investigation of dewetting corner. *to be submitted to J FLUID MECH*, 2012.

M. Riepen, F. Evangelista and S. Donders. Contact line dynamics in immersion lithography-dynamic contact angle analysis. In *Proc. 1st Euro. Conf. Microfluidics*, 2008.

K. G. Winkels et al. Receding contact lines: From sliding drops to immersion lithography. *EUR PHYS J-SPEC TOP*, **192**, 195, 2011.

CHAPTER 6

DISCUSSION AND CONCLUSION

Contact line instabilities at intermediate Reynolds number are observed in industrial applications, e.g. an immersion lithography machine, where the velocity of wetting and dewetting contract lines increases up to $O(1\ \mathrm{m/s})$. In the last two decades, extensive research has been conducted on contact line instability. Despite these efforts, little is still known about the instability mechanism of wetting and dewetting contact lines in this industrial problem. Therefore, the present thesis reports an attempt to study partial dewetting flows at intermediate Reynolds number (in particular, for a liquid immersion droplet) by means of experimental, theoretical, and numerical analysis.

As part of the theoretical analysis, we have first performed a scaling analysis based on shadowgraphy measurement results. Then, we reported that nonlinear acceleration terms (i.e. inertia forces) are not negligible in comparison with viscous and pressure forces. Furthermore, an empirical model is obtained from experimental results, showing a relation between the dynamic receding contact angle and the corner opening angle of the immersion droplet.

Secondly, we have obtained a modified lubrication model at $Re{\cdot}\epsilon > 1$. To obtain the model, we assume that streamlines are nearly parallel and straight, which is validated experimentally. Then, a modified pressure is introduced that accounts for the capillary and the dynamic pressure. The inertial effects, i.e. the nonlinear acceleration terms, are expressed in terms of the dynamic pressure.

Thirdly, we have quantitatively assessed the similarity results between the gravity-driven droplets on an inclined plane at $Re \ll 1$ and the immersion droplet at $Re \sim O(100)$. Based on the modified lubrication model, we have obtained an interface equation, which describes the shape of dewetting corner at $Re{\cdot}\epsilon > 1$. From this model, we have shown that two angles (receding contact angles θ and corner opening angles Φ) are correlated to each other, which is also observed in the gravity-driven liquid droplets. However, the current model presents that the dynamic pressure (derived from the nonlinear acceleration terms) becomes dominant when the corner opening angle decreases (i.e. high speed of dewetting). When the corner opening angle is large, the capillary pressure is important. However, for the gravity-driven liquid droplet on an incline, the capillary pressure only plays a role in the Stokes flow problem. Furthermore, we have presented that the flow patterns obtained by analytical solutions near the corner are almost the same in both flow configurations, i.e. the gravity-driven droplet and the immersion droplet. In both cases, the analytical results for the flow pattern are governed by the interface equation, $H(y/x)$. The analytical model is validated and confirmed by experimental data. As a consequence, we could conclude that a primary parameter determining the droplet breakup is the shape of dewetting. Namely, to prevent the droplet breakup, it is important to avoid a sharp corner shape.

In this study, however, there is still a questionable aspect between the gravity-driven droplet at $Re \ll 1$ and the immersion droplet at $Re \sim O(100)$. From our results, we could presume that both examples have a similar flow pattern. The main difference is the magnitude of the internal velocity profile. In the case of the gravity-driven droplet, the nonlinear acceleration terms, i.e. inertial effects, are neglected by using the creeping flow approximation ($Re \ll 1$)and classical lubrication approximation ($Re{\cdot}\epsilon \ll 1$). Stone et al. (2002) and Limat and Stone (2004) first dealt with a three-dimensional lubrication model to describe the corner shape of the dewetting flow problem. In their results, the corner opening angles are underestimated by the theoretical model, when the contact line speed increases (high Ca and small θ). Our modified lubrication model better predicts the results. It might be that the nonlinear acceleration terms are also important in the gravity-driven droplet problem.

We can also recall the typical flow patterns near the corner structure of dewetting to raise an effect of nonlinear acceleration terms. The streamlines are straight and the flow field converges to the corner. While the fluid element is accelerated along streamlines, the fluid is stretched along streamlines and contracted along equipotential-lines at the same time. We hypothesize that if the dewetting structure shows a conical shape, the nonlinear acceleration terms might be considered. For this hypothesis, it needs to be substantiated by additional research.

Furthermore, here, we have one more open question. Cox (1986) and Voinov (1976) first proposed a hydrodynamic model to describe dynamic wetting and de-wetting, which provides an expression for the dynamic contact angle as a function of the capillary number, i.e. $\theta^3 = \theta_s^3 \pm 9Ca\ \ln(x/l)$. The model is limited to the Stokes flow regime. Interestingly, for the current problem, we have also observed a similar result that the dynamic receding contact angle θ^3 is proportional to the capillary number, similar to the Cox-Voinov law, $\theta^3 \propto Ca$. Figure 6.1 shows the relation between θ^3 and Ca for the experimental results (symbols) where the solid lines represent linear fits to the measurement results. For comparison, the original lubrication theory prediction for the Stokes regime is shown as the dashed line of figure 6.1. In the case of the de-wetting problem at $Re \sim O(100)$, the slope is approximately

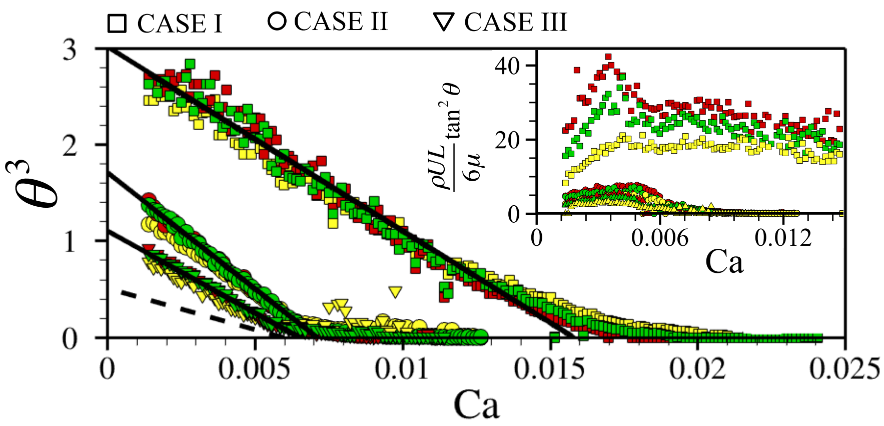

Figure 6.1: θ^3 versus Ca for different droplet volumes and solid surface conditions, where θ is the dynamic receding contact angle [rad]. The solid lines represent linear fits to the measurement results, and the dashed line is the conventional theory for a droplet sliding down an inclined substrate (Peters et al. (2009)). The red symbol notes for $H = 300$ µm; the green, $H = 250$ µm; the yellow, $H = 200$ µm above the different surface conditions, i.e., (a) $\theta_s = 89\pm8°$; (b) $\theta_s = 76\pm8°$; and (c) $\theta_s = 63\pm15°$.

two times larger than the Cox-Voinov model. However, so far there is no satisfactory explanation for this result.

Here, we try to explain it based on our new model taking into account inertia. In section 4.4.1, we have shown the modified lubrication model including dynamic pressure effects (see equation 4.18). It is recalled that the dynamic term is $(\rho h^2\tilde{\nabla}q^2)/(6\mu U)$. To directly measure this value is difficult but we can approximately calculate $(\rho Ux\cdot\tan^2\theta)/(6\mu)$ where $\tan\theta$ and q are assumed to be h/x and U, respectively. This approximated value is relatively constant for $Ca > 0.006$, as shown in the inset of figure 6.1. If this additional dynamic term is constant, the relationship (Cox 1986; Voinov 1976) between the contact angle and the substrate speed can be formulated as:

$$\theta^3 = \theta_s^3 \pm \Gamma\cdot Ca, \tag{6.1}$$

where θ is the dynamic receding contact angle and θ_s the static contact angle. Here, the pre-factor Γ is $9\cdot\ln(\alpha/l)$ for the Stokes flow problem (Cox 1986; Voinov 1976) where α is a macroscopic length and l is a microscopic length scale that is introduced to prevent a divergence of the dissipation. In the case of taking into into account inertia, from equation 4.18, Γ can be modified as $9(1+\beta)\cdot\ln(\alpha/l)$ where β describes inertial effects, $(\rho h^2\tilde{\nabla}q^2)/(6\mu U)$. The new Γ value accounting for inertia effects should be investigated in further detail.

For the experimental analysis, we have performed tomographic particle image velocimetry to obtain full three-dimensional three-velocity components at a small scale. There are several other three-dimensional velocimetry techniques, e.g. holographic particle image velocimetry, stereo particle image velocimetry, 3D particle tracking velocimetry, defocused particle image velocimetry, confocal scanning particle image velocimetry, and magnetic resonance velocimetry. Among those, we believe that tomographic particle image velocimetry is the best measurement technique for this research. There are three main reasons: Firstly, it provides a good spatial resolution of the 3D-3C velocity vector field. In this problem, the results provide a spatial resolution of 15 μm. Secondly, we successfully measure the flow field near the moving contact lines by this technique. (Actually, it is difficult to measure the flow field close to a gas-liquid interface due to a non-uniform refractive index.) Thirdly, although the volumetric gas-liquid interface is difficult to recognize, the tomographic reconstruction allows to obtain the droplet shape.

On the other hand, tomographic particle image velocimetry has some minor drawbacks. For instance, a long calculation time for the tomographic reconstruction and interrogation is required in comparison with other measurement techniques. In this respect, a further improvement of algorithms to reduce the computational load is desired. Furthermore, due to a multi-camera measurement technique, a proper calibration has to be performed as accurate as possible. Additionally, the volume self-calibration is essential to improve the accuracy which can be hardly improved by the initial calibration.

In fact, an initial plan was to perform 3D particle tracking velocimetry. However, this does not provide a reliable result compared with tomographic particle image velocimetry. Although we have investigated this problem step-by-step, we could not firmly explain the differences. In particular, we have reported that the main problem is a questionable particle reconstruction result. The 3D particle distributions in a volume obtained by 3D-PTV vary along the droplet height, while Tomo-PIV provides a constant 3D particle distributions in the volume. We presume that during triangulation the complex flow pattern can cause an erroneous particle detection. It is required to further investigate the particle identification by triangulation in the complex flow field.

In the numerical approach, we have introduced a simplified numerical model to investigate a flow pattern. The flow field is generated by a simplified immersion needle. The results are in good agreement with the experimental results. However, this numerical work still has a limitation. The gas-liquid interface is assumed to be an inflexible boundary. To improve this numerical model, further studies by using a flexible boundary condition are needed. Furthermore, it is required to investigate a real immersion hood having a complex geometry by comparing numerical and experimental studies. Nonetheless, we believe that this study has led to new insights into the flow pattern of the immersion droplet and this simplified numerical model can assist to improve the immersion hood design.

APPENDIX A

SUPPLEMENT: EXPERIMENTAL SETUP

This research is carried out as a part of the Industrial Partnership Programme (IPP), Contact line control during wetting and dewetting (CLC). The experimental setup used in the project is supplied by ASML.

A.1 Recirculation unit

The aim of this project is to visualize and investigate the internal flow pattern of a liquid immersion droplet. To perform Particle Image Velocimetry (referred to as PIV), the flow must be seeded with fluorescent particles. It is important to keep a constant seeding density of the particles during the PIV experiments. Therefore, we have a recirculation system as shown in figure A.1 (see also figure 2.3). The working fluid (seeded with fluorescent particles) and air are extracted from the droplet and reserved into the vacuum chamber. Then, the water and air are separated by pumps. The extracted water is moved into a stirring device to keep the seeding density of the particles uniform. Before supplying the working fluid again, we degas and filter out dust. In the recirculation system, every chamber has a level sensor. With these sensors, this setup automatically keeps circulating the working fluid during the measurement.

A.2 Glass wafer

In an early stage of the experiments, we observed that a commercial wafer does not provide accurate specifications, as shown in figure A.2. The wafer thickness is not constant over the

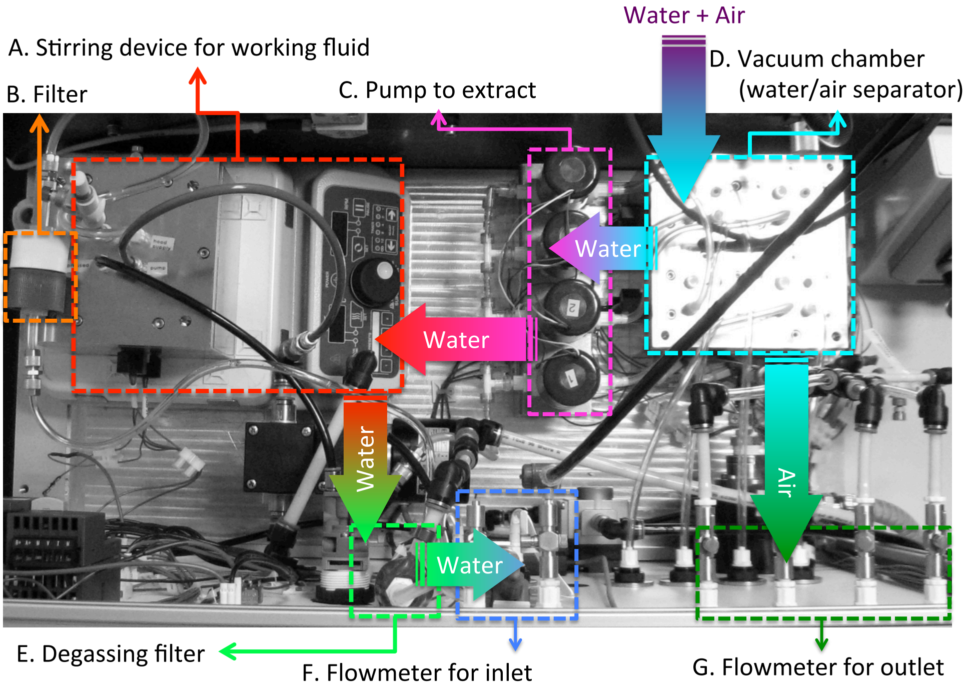
Water + Air
A. Stirring device for working fluid
B. Filter
C. Pump to extract
D. Vacuum chamber
(water/air separator)
Water
Water
Water
Air
Water
E. Degassing filter
F. Flowmeter for inlet
G. Flowmeter for outlet

Figure A.1: Illustration of the re-circulation system.

whole area. In this study, flatness of the wafer is very important to keep a constant height of the immersion droplet. In the current research, the droplet height is of the order of 100 μm. We searched many wafer suppliers and investigated the specification of wafers. However, it is not possible to have a very accurate wafer (see Table A.1). Therefore, we applied a mechanical device that maintains a fixed reference position of the substrate. By this device, a global flatness at the edge of the wafer is controlled within ±1 μm (see figure 2.6).

Acknowledgement
We would like to thank Martijn Verdonck (ASML) who manufactured the re-circulation unit for the project.

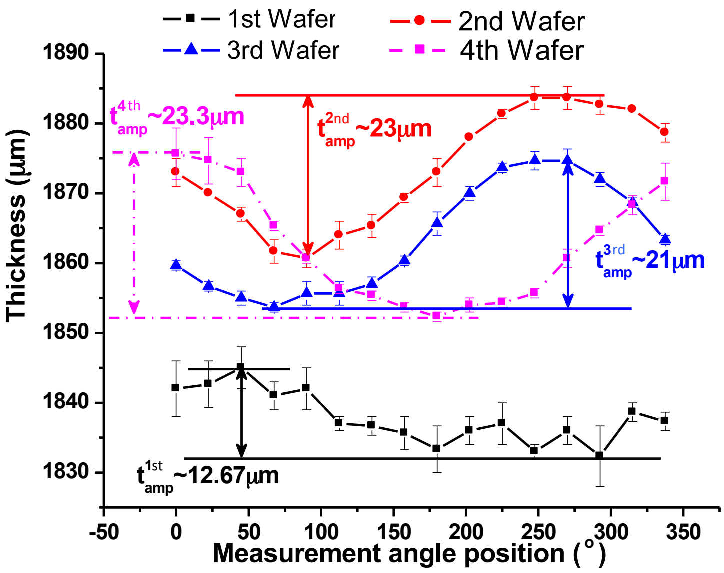

Figure A.2: Thickness variation of glass wafers. The edge thickness of four different wafers is measured by a micrometer and the wafer samples are provided by ASML for the research project.

Table A.1: Comparison of wafer specifications.

Company	Specification
Technical glass products, Inc.	D: 300 mm / T: 2 mm, Err. < 2 – 4 waves/inch
LSP Quartz, B.V.	D: 305 mm / T: 2 ± 0.05 mm
LSP Quartz, B.V.	D: 305 mm / T: 0.7 ± 0.05 mm
SVM	D: 300 ± 0.2 mm / T: 2.75 ± 0.2 mm
SVM	D: 300 ± 0.3 mm / T: 0.7 ± 0.05 mm
Mirtec	D: 300 mm / T: 6.3 mm , Local Err: O(10 nm)
Armstrong optical	D: 300 ± 0.1 mm / T: 2.7 mm, Local Err: O(600 nm)
Valley Design	D: 300 mm / T: 0.7 mm, Err. < 3 – 4 waves/inch

D: diameter / T: thickness

APPENDIX B

PARTICLE DEPOSITION

During the PIV measurement, some particles remain on the substrate as shown in figure B.1, which is taken by SEM (Scanning Electron Microscope, Quanta 3D Dualbeam FEI).

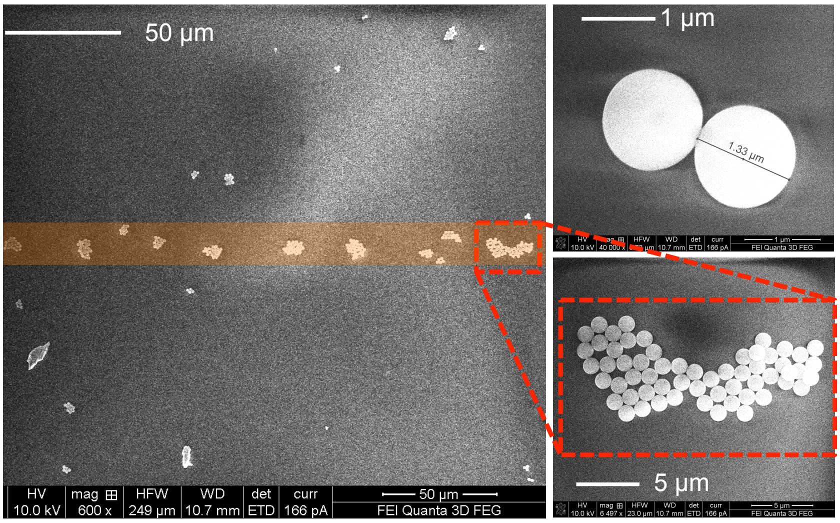
50 µm
1 µm
1.33 µm
5 µm
HV
10.0 kV
mag ⊞
600 x
HFW
249 µm
WD
10.7 mm
det
ETD
curr
166 pA
50 µm
FEI Quanta 3D FEG

Figure B.1: SEM photographs: remaining particles on a substrate. The accumulated particles are aligned in a horizontal line (the orange color zone), which is the location of the corner tip of dewetting.

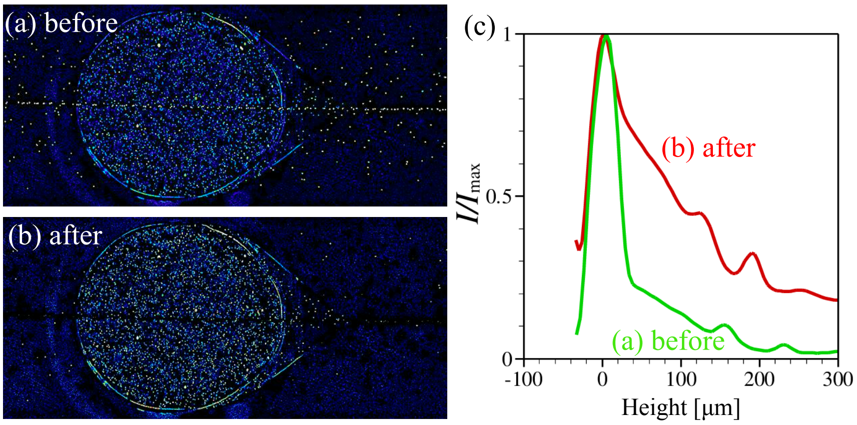

Figure B.2: Post-image processing: (a) before and (b) after reducing the sticky particles. (c) comparison of particle intensity distributions in the depth direction.

Nonetheless, the particles do not change the dewetting curvature of the moving droplet (see chapter 2). We can assume that other dynamic effects are much stronger than this. When we obtain velocity estimates, we perform cross-correlation of the recorded particle distribution at two exposures. The particles that remain on the substrate could bias the local velocity measurements. Therefore, we need additional image processing to get rid of the particles attached to the substrate. We recognize the particles by detecting the brightest intensity signal. The particles are then removed by using MATLAB image processing, as shown in figure B.2. These sticky particles affect the reconstructed intensity profile in tomographic particle image velocimetry (see figure B.2(c)). Therefore, it is essential to get rid of the sticky particle as much as possible.

To our best knowledge, the reason of the sticky particles is not known but we can provide some theories. First, particles are naturally charged negative in water. If a local region of a glass wafer is partly charged positive, then the particle can easily stick to the substrate. Second, according to the present experimental setup, the inflow impinges vertically downward to the wafer and therefore the particles stick to the substrate. Last, the number of sticky particles is related to the substrate coating condition. For instance, if the substrate is hydrophobic, then the sticky particles are less than the hydrophilic surface. In the case of the hydrophilic substrate, the dewetting flow structure is relatively thin compared to the hydrophobic substrate case. The particles are affected by the flow structure. To figure out this problem, it is essential to study this further.

Acknowledgement

We would like to thank David S. Jun (Imaging Science and Technology, Applied Sciences, TUDelft) who helped us to take SEM pictures.

Appendix C

Validation for shooting method

This appendix contains the shooting method code validation. Limat and Stone (2004) first presented the three dimensional lubrication model by considering the balance between viscous and capillary forces. They assumed the limit of small receding contact angle in the three-dimensional corner structure and highly viscous fluid flow. The similarity solution

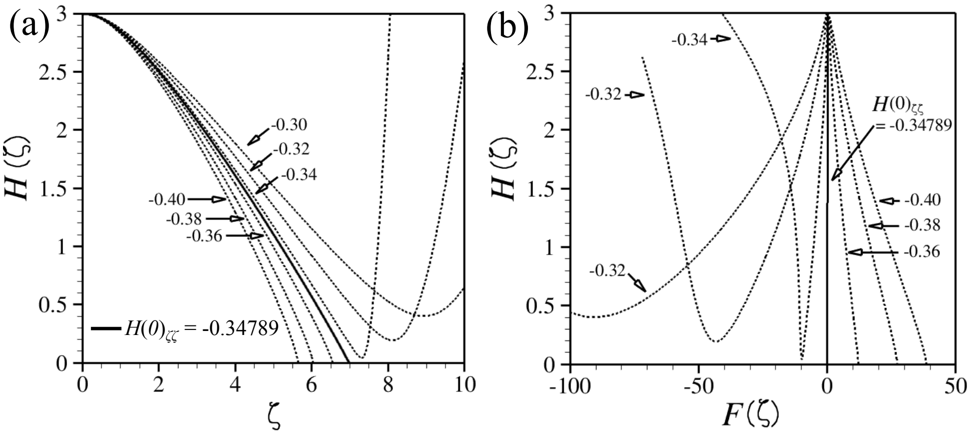

Figure C.1: Numerical code validation of the Runge-Kutta 4th order method. The different solutions of equation C.1, for $H(0)=H_0=3$ and several values of $H_{\zeta\zeta}(0)$.

$h(x,y) = Ca^{1/3}xH(y/x)$ is first suggested and then they give,

$$\begin{aligned}3(H-\zeta H_\zeta) =&(1+\zeta^2)^2(H^3H_{\zeta\zeta\zeta})_\zeta + 3\zeta(1+\zeta^2)(H^3H_{\zeta\zeta})_\zeta \\ &+2\zeta(1+\zeta^2)H^3H_{\zeta\zeta\zeta} + (1+3\zeta^2)H^3H_{\zeta\zeta}.\end{aligned} \tag{C.1}$$

This equation has a unique pair solutions of $H(0) = H_0$ and $H_{\zeta\zeta}(0) = H_0''$ as shown in figure C.1(a). To find out the solution pairs they consider the mass conservation in the corner structure. Therefore, they calculated the mass flux in x-direction between $y = -\zeta x$ and $y = \zeta x$,

$$F(\zeta) = \int_0^\zeta \left[H^3\left(\zeta[1+\zeta^2]H_{\zeta\zeta}\right)_\zeta + \frac{3}{H^2}\right] d\zeta. \tag{C.2}$$

The numerical code calculates equation C.1 by using the shooting method until $F(\zeta) = 0$. When $H(0) = 3.0$, $H(0)_{\zeta\zeta} = -0.34789$ is the matching solution to satisfy the mass conservation. As shown in figure C.1, the results show the same as the result of Limat and Stone (2004); Snoeijer et al. (2005).

C.1 Bibliography

L. Limat and H. A. Stone. Three-dimensional lubrication model of a contact line corner singularity. *EUROPHYS LETT*, **65**, 365, 2004.

J. H. Snoeijer et al. Self-similar flow and contact line geometry at the rear of cornered drops. *PHYS FLUIDS*, **17**, 072101, 2005.

Acknowledgements

This thesis is the fruit of four years of research at the Laboratory for Aero- and Hydrodynamics of the Delft University of Technology in the Netherlands. These years have been a nice time for me, broadening and deepening my knowledge of fluid dynamics. Furthermore, it was a good time to learn about a different culture. Living in Europe has not always been easy but I could manage due to all those people who helped and supported me in a different way. Here, I want to thank all the people.

Foremost, I am very grateful to Prof. Jerry Westerweel for his supervision and guidance during my PhD. During four years, his support and contribution have been priceless. It is impossible not to get affected by both his encouragement and expertise, which have helped me very much in completing this work. Many thanks go to Christian Poelma, whose feedbacks and comments contributed greatly to my work. Furthermore, I thank him for constantly correcting my English writing and for translating the Dutch summary. I especially appreciated the bi-weekly meetings with both of them, which were the source of many good ideas and fruitful discussions. I sincerely thank Gerrit Elsinga for his contribution to my work, in particular the measurement technique. It was a pleasure to work together to perform the 3D-3C velocimetry measurement techniques. I consider myself very lucky having had two daily-advisors, Christian and Gerrit, who were always willing to listen and give valuable advice. Besides, I thank Ralph Lindken and Sebasitan Große, who helped me a lot to experience the measurement world for the first time. They taught me the basics of μ-PIV. In early stages of the research, their contributions have been worthwhile. I also thank Mathieu Pourquie, who helped me to use the numerical code and contributed to chapter 7. Sometimes, his joke makes me learn the Dutch culture. I should thank Gijs Ooms, who discussed my work and wrote a recommendation for me.

I thank all the colleagues in the lab, who made the past four years successful and enjoyable. So, I would like to mention Gosse Oldenziel, Norbert Warncke, Ree Delfos, Ria van der Brugge-Peeters, Caroline Legierse, Edwin Overmars, Gea Parikesit, Ritau Yang, Massi Rossi, Nikolay Semin, Wim-Paul Breugem, Cor Gerritsen, Simon Toet, Joop Bodde, Carole Leguy, Marc Harleman, Mark Franken, Jeanette Hussong, Astrid Kloosterman, Valentina Koschatzky, Dirk Jan Kuik, Marcel Kwakkel, Oleksandr Zverkhovskyi (Sasha), Sedat Togoz, Arnoud Greidanus, Marike Schenker, and Ulrich (Ulri) Mießner. (I am sorry that I did not much join the 10 o'clock coffee break. That is so early to me.) Especially, I wanna thank again Norbert Warncke, who suggested to learn 'ROWING'. It was a very nobel and fun experience although I only took the rowing course for 4 months. I thank again Gosse, who is my office-mate and is the only guy who want to learn Korean expression in the lab.

Next, I first thank to Kyungchang Nam who is my best friend ever. Over 20 years, we have a friendship. He always supports and cheers me when I have a trouble. Here, I congratulate again for his marriage for 2012. Special thanks to Nam Seok Kim, who introduced and recommended excellent belgium beers. I am awakened to a belgium beer world due to him. Also, he made me get used to life in the Netherlands and he helped me a lot. I also

wish to thank Hansol Moon, Sungheon Oh, Chang Ho Yeo, Kyungho Choe (Gom), David Sangbeom Jeon, Jake Jung, Hyunjun Choi, Zooyoung Jung, Chajoog Kim, and Joongsoo Kim for their sharing funny and joyful time. I want to thank again Chang Ho Yeo, who taught me playing tennis. I should miss all the valuable times and memories. The advice and suggestions of Dr. Eun-Seong Cho of the Department of Process and Energy were also helpful and appreciated. Additionally, I pray for the repose of the soul of many chickens for Delft Fried Chicken (DFC). Very special thanks to SkyPe and FaceTime, which enabled to see my fiancee. Now, she is my wife. :)

I close this list the most important people in my life. I would like to thank my family for their unconditional support and trust during these four years. Finally, I absolutely thank my wife, Kyungeun Lee, for cheering and encouraging me during many difficult times. Despite a long and long distance you are with me in all I do. No words can depict how grateful I am and therefore I dedicate this work to you, my wife, Kyungeun Lee.

Delft, February 2013
Hyoungsoo Kim

List of Publications

Journal articles

Kim H; Kim T-H; Lee J; Kim H-Y; (2013) "Spontaneous induced mixing at 3-phases contact line," in preparation

Kim H; Poelma C; Ooms G; Westerweel J (2013) "Experimental and theoretical investigation for de-wetting flow corner," to be submitted to *J FLUID MECH*

Belmiloud N; Kim H; Mertens PW; (2013) "Hydrodynamics model of an evaporating colloidal droplet with receding contact lines," in preparation

Kim H; Westerweel J; Elsinga GE (2012) "Comparison of Tomo-PIV and 3D-PTV for microfluidic flows," *MEAS SCI TECHNOL* Vol. 24(2), pp. 024007

Kim H; Große S; Elsinga GE; Westerweel J (2011) "Full 3D-3C velocity measurement inside a liquid immersion droplet," *EXP FLUIDS* Vol. 51(2), pp. 395-405

Kim H; Kwak HS; Westerweel J (2011) "Assessment of mixing applications on the EOF with thermal effects," *COLLOID SURFACE A*, Vol. 376, pp. 53-58

Kwak HS; Kim H; Hyun JM; Song T-H (2009) "Thermal control of Electroosmotic Flow in a Microchannel through Temperature-Dependent Properties," *J COLLOID INTERF SCI*, Vol. 335, pp. 123-129

Conference proceedings

Kim T-H; Kim S; Kim H-Y; Kim H (2013) "Vortex-induced mixing at 3-phase contact line," 2nd Symposium on Fluid-Structure-Sound Interactions and Control (FSSIC2013), Hong Kong (Oral by Kim T-H)

Kim H; Elsinga GE; Westerweel J (2012) "Tomographic PIV towards a complex free surface," 8th KSME-JSME THERM FLUIDS ENGN , Incheon, South Korea (Oral)

Kim H; Poelma C; Westerweel J (2012) "A simplified analysis model for a liquid immersion drop," Physics@FOM Veldhoven (Oral)

Kim H; Poelma C; Westerweel J (2011) "Investigation of partially dewetting flow at Re $\sim O(100)$ and Ca $\sim O(0.01)$," 64th Annual Meeting of the APS Division of Fluid Dynamics, Baltimore, US (Oral)

Kim H; Poelma C; Westerweel J (2011) "Study on moving contact line at Re $\sim O(100)$," Gordon Research Conference 2011, USA (Oral)

Kim H; Große S; Westerweel J (2010) "Assessment of fundamental flow pattern inside a liquid immersion droplet," MicroNano Conference 2010, Enschede, the Netherlands (Poster)

Kim H; Franken M; Große S; Elsinga GE; Westerweel J (2010) "micro-PIV inside a moving immersion droplet," Invited lecture, International Symposium on Micro/Nano Flow Measurement Techniques, Tokyo, Japan (Oral by Westerweel J)

Kim H; Kwak HS; Westerweel J (2010) "A mass transfer in EOF with thermal effects," Proc. of the 9th International Electrokinetics Conference (ELKIN), Turku, Finland (Oral)

Kim H; Franken M; Westerweel J (2010) "Study on contact line dynamics and flow field of immersion lens droplet by 3D-PTV and TIRFM," Physics@FOM Veldhoven (Poster)

Kim H; Große S; Riepen M; Westerweel J (2010) "Experimental investigation of internal flow in an immersion droplet by 3D PTV," Proc. of the 14th International Symposium on Flow Visualization, Daegu, Korea (Oral)

Kim H (2010) "Experimental investigation of internal flow field of immersion lens droplet by 3D-PTV," Contact line instabilities, Lorentz center, the Netherlands (Oral)

Media

Kim H; Große S; Elsinga GE; Westerweel J (2010) "Challenge to the small-scale 3D flow field measurement nearby moving contact lines," JMBC newsletter

Curriculum Vitae

February 28, 1981	**Born** in Busan, Republic of Korea
1999 – 2006	*Summa Cum Laude*, **Bachelor** of Engineering degree in Department of Mechanical Engineering at Kumoh National Institute of Technology (**kit**), Gyeongbuk, Gumi, Republic of Korea
2006 – 2008	*2007 Outstanding dissertation award for BK21*, **Master** of Science in Engineering degree in School of Mechanical, Aerospace and Systems Engineering in Division of Mechanical Engineering at Korea Advanced Institute of Science and Technology (**KAIST**), Daejeon, Republic of Korea
2008 – 2012	**PhD** research at the Laboratory for Aero- and Hydrodynamics, which is part of the Process & Energy department, faculty of Mechanical, Marine, and Material science (3mE), Delft University of Technology(**TUDelft**), the Netherlands
2012	Visiting researcher at Micro Fluid Mechanics Laboratory in the School of Mechanical and Aerospace Engineering at Seoul National University(**SNU**), Seoul, Republic of Korea
2013 – 2015	**Postdoctoral** researcher at Complex Fluids Group in the Department of Mechanical and Aerospace Engineering at Princeton University (**PU**), NJ, USA